

NOVEL LIGHT-ACTIVATED TUMOR TARGETING DRUG CARRIERS USING SICKLE
RED BLOOD CELLS

By

SE-WOON CHOE

A DISSERTATION PRESENTED TO THE GRADUATE SCHOOL
OF THE UNIVERSITY OF FLORIDA IN PARTIAL FULFILLMENT
OF THE REQUIREMENTS FOR THE DEGREE OF
DOCTOR OF PHILOSOPHY

UNIVERSITY OF FLORIDA

2011

© 2011 Se-woon Choe

To parents, wife and lovely children:
Younghoon Choe and Younja Son,
Yoonsun Choi,
Jean Choe and Andrew Hanwool Choe

ACKNOWLEDGMENTS

I would like to sincerely thank to my advisor, Dr. Brian S. Sorg, for his excellent support and guidance to finish my Ph.D. study. Dr. Sorg always inspired me how to be an independent researcher with more creative and critical perspective. His voice was always calm but powerful. Without his advice this dissertation would not be possible.

I am indebted to my committee members, Dr. Dietmar W. Siemann, Dr. Johannes (Hans) van Oostrom and Dr. Rosalind J. Sadleir for their constructive criticism and assistance. I also would like to express my gratitude to Dr. Angela E Rivers and Dr. Richard Lottenberg for their collaboration.

I am grateful to Dr. Paul S. Oh for his interest and support, which helped improve the quality of this dissertation. I also thank his lab members, Chul Han, Yonghwan Kim and Dr. Chul Song, for giving me a warm welcome whenever I visit to ask their help.

I have been very fortunate to work with all past and current KeSorgle lab members. I would like to acknowledge Dr. Mamta Wankhede, Raymond Kozikowski, Jennifer Lee, Casey deDeugd, Nikita Agarwal, Phillip Barish, and Dr. Abhinav Acharya for their helpful discussion. I also thank my Korean friends, Dr. Soondo Yoon, Dr. Sungho Oh, Choongheon Lee, Kyungpyo Hong, Dr. Sahngmin Han, Hyochul Ahn, Myungsang Kim, Jintaek Ock and Jinseok Hong for their cheerful encouragement and friendship.

I greatly appreciate my parents and parents-in-law, Younghoon Choe, Younja Son, Sangkyun Choi and Soohee Yu, for their endless love and support. Especially, my parents always cheer and strengthen me throughout my life. I also appreciate my sisters and brothers, Koheun Choe, Soeun Choe, Arma Choe, Soomin Park, Soonhyoung Jung, and Yoongyu Choi for their love and concern. I am so happy to be a proud father

to my kids, Jean Choe and Andrew Hanwool Choe who are the most precious gifts in my life.

Last but not least, I am so grateful to my soul mate, lovely wife Yoonsun Choi.

TABLE OF CONTENTS

	<u>page</u>
ACKNOWLEDGMENTS.....	4
LIST OF TABLES.....	9
LIST OF FIGURES.....	10
ABSTRACT	12
CHAPTER	
1 INTRODUCTION	13
Current Drug Delivery Strategies to Tumors	13
Enhanced Permeability and Retention Effect Based Passive Targeting to Solid Tumors	15
Resealed Erythrocytes as a Drug Carrier	18
Sickle Red Blood Cells as a Potential Drug Carrier	21
Controlled Drug Release by Photoactivation using.....	23
Gompertz Function	26
Microdialysis Method for in-vivo Delayed Photohemolysis Measurement.....	27
Motivation and Goal of this Study	34
2 MATERIALS AND METHODS	35
Window Chamber Installed Mouse Model.....	35
Imaging System	36
Imaging Acquisition.....	37
Hyperspectral Imaging of Hemoglobin Saturation map.....	37
Delayed Photohemolysis Measurements.....	39
In-vitro Delayed Photohemolysis Measurement Systems	39
In-vivo Delayed Photohemolysis Measurement using Microdialysis Tubing.....	40
3 INTRAVITAL MICROSCOPY IMAGING OF MACROPHAGE LOCALIZATION TO IMMUNOGENIC PARTICLES AND CO-LOCALIZED TISSUE OXYGEN SATURATION.....	46
Materials and Methods.....	48
Microparticles	48
Macrophage Cell Line	50
Animal Model.....	50
Intravital Fluorescence and Spectral Imaging.....	52
Results.....	53
Hyperspectral and Fluorescence Imaging	53

Quantitative Analysis for Hemoglobin Saturation Map, Microparticles and Macrophages	54
Statistical Analysis for Accumulated Region of Interests Data	55
Discussion	64
4 PREFERENTIAL ACCUMULATION OF SICKLE RED BLOOD CELL IN TUMORIC ENVIRONMENT.....	69
Materials and Methods.....	71
Tumor Cells	71
Animal Model.....	72
Window Chamber Installation.....	72
Preparation of Blood Cells.....	73
Intravital Spectral and Fluorescence Imaging.....	74
Histology.....	76
Results.....	77
Monitoring Hb Saturation Map.....	77
In-vivo Numerical Analysis of Accumulated Sickle Red Blood Cells using a Single Fluorescent Microscopic Image.....	77
In-vivo Numerical Analysis of Accumulated Sickle Red Blood Cells using Fluorescence Video Recording	79
Histological Analysis of Accumulated Sickle Red Blood Cells in Liver, Spleen and Tumor Tissues	80
Discussion	88
5 IN-VIVO DELAYED PHOTOHEMOLYSIS MEASUREMENT FROM PHOTSENSITIZED SSRBCs LOADED WITH CALCEIN in 4T1 TUMOR BEARING MOUSE MODEL.....	91
Materials and Methods.....	93
Materials.....	93
Preparation of Blood Cells.....	93
Preparation of Loaded Blood Cells with Calcein.....	94
Preparation of Photosensitized Blood Cells by PpIX	95
In-Vitro Delayed Photohemolysis Measurement.....	95
Gompertz Function	96
Tumor Cells	97
Animal Models.....	97
In-vivo Delayed Photohemolysis using Microdialysis Tubing.....	98
Results.....	99
Efficacy of Calcein Loading Rate into Sickle Red Blood Cells.....	99
In-vitro Delayed Photohemolysis Measurement of Photosensitized SSRBCs by PpIX.....	100
Analysis of in-vitro Delayed Photohemolysis Measurement by Gompertz Function	101
In-vivo Controlled Calcein Release Form Sickle Red Blood Cells	101
Discussion	112

6	CONCLUSIONS AND FUTURE WORKS.....	115
	Summary and Conclusion.....	115
	Future Works	116
	LIST OF REFERENCES	118
	BIOGRAPHICAL SKETCH.....	137

LIST OF TABLES

<u>Table</u>	<u>page</u>
1-1 Drug delivery systems (DDS) in clinical trials and practice (adapted from [5]) ...	14
1-2 Factors responsible for the EPR effect of macromolecules in solid tumors (adopted from [29])	17
1-3 Comparison of carrier erythrocyte to other DDS in mouse model (adapted from [35])	18
1-4 Advantages and disadvantages of erythrocytes in drug delivery (adopted from [34])	20
1-5 Comparison of various hypo-osmotic lysis methods (adapted from [62, 63])	21
1-6 Summary of advantages and limitations of microdialysis sampling technique (adopted from [120])	29
4-1 Categorized groups for preferential accumulation of SSRBCs to tumoric microvasculature experiment.....	71
5-1 Categorized groups for in-vivo DPH measurement of SSRBCs to tumoric microvasculature experiment.....	98
5-2 SSRBCs with 25µM PpIX irradiated with 0.08W halogen lamp at various irradiation times at fixed irradiation and incubation temperature.....	108

LIST OF FIGURES

<u>Figure</u>	<u>page</u>
1-1 Pathophysiology of vaso-occlusion by SSRBCs.....	30
1-2 DPH measurement from photoactivated RBCs by PpIX with 10 μ M.....	31
1-3 Example plot of age-specific mortality rates with random parameters by Gompertz function.	32
1-4 Typical microdialysis probe configurations and sampling process.....	33
2-1 Window chamber installed mouse model.	41
2-2 Hyperspectral imaging system.....	42
2-3 Hyperspectral imaging to create HbSat map	43
2-4 Experimental setup for in-vitro DPH measurements. The sample cuvette in temperature controller at under physiological temperature is exposed by 0.08W halogen lamp.....	44
2-5 In-vivo DPH measurement setup with 4T1 tumor mass bearing mouse model. .	45
3-1. Hyperspectral and fluorescence images for a control mouse with saline (carrier) injection without microparticles.	57
3-2 Hyperspectral and fluorescence images for a LPS(-) mouse with microparticles lacking LPS	58
3-3 Hyperspectral and fluorescence images for a LPS(+) mouse with LPS encapsulated microparticles (400,000 in 20 μ L).	59
3-4 Hyperspectral and fluorescence images for LPS(++) mouse with LPS encapsulated microparticles (2,000,000 in 20 μ L).	60
3-5 Numerical HbSat data for each group of ROIs at various time points. The ROIs are selected on arterioles and venules separately.	61
3-6 Numerical macrophage signals for each group of ROIs at various time points. The ROIs are selected on arterioles and venules separately.	62
3-7 The accumulated ROI data overall time points are analyzed using ANOVA and Scheffe's post-hoc test.	63
4-1 Hyperspectral images of dorsal skinfold window chamber.	82

4-2	Microscopic images of postcapillary venules with transmitted light and fluorescence images were acquired.	83
4-3	Bar graphs show numerical fluorescence intensities on selected ROIs in each group (mean±SD).	84
4-4	In-vivo numerical analysis of accumulated RBCs and SSRBCs using video recording with 20x objective.	85
4-5	Fluorescently labeled cells in tissue specimens including liver, spleen and tumor were compared.....	87
5-1	Light microscope and fluorescence flow cytometry techniques were employed to analyze the efficiency of hypotonic preswelling method to SSRBCs.	103
5-2	Delayed photohemolysis in normal canine RBCs photosensitized with PpIX were measured at 415nm.....	104
5-3	Fractional photohemolysis rates of photosensitized SSRBCs by 25 µM of PpIX were measured.	107
5-4	Parameters for Gompertz function were calculated based on fractional DPH measurement of SSRBCs carrying calcein with various irradiation time (t_{irr}). ...	109
5-5	In-vivo fluorescence signal measurement through systemic administration of prepared blood sample groups.	111

Abstract of Dissertation Presented to the Graduate School
of the University of Florida in Partial Fulfillment of the
Requirements for the Degree of Doctor of Philosophy

NOVEL LIGHT-ACTIVATED TUMOR TARGETING DRUG CARRIERS USING SICKLE
RED BLOOD CELLS

By

Se-woon Choe

August 2011

Chair: Brian S. Sorg
Major: Biomedical Engineering

Conventional drug carriers such as liposomes, nanoparticles and red blood cells for cancer chemotherapy shield normal tissues from toxic drugs to treat cancer cells in tumors. However, inaccurate tumor targeting, uncontrolled drug release from the carriers and unwanted accumulation in healthy sites can limit treatment efficacy with current conventional drug carriers with insufficient concentrations of drugs in the tumors and unwanted side effects (i.e., systemic cytotoxicity) as a result.

In this research, we examined the use of sickle red blood cells as a new drug carrier with novel tumor targeting and controlled release properties. Sickle red blood cells show natural tumor preferential accumulation without any manipulation and controlled drug release is possible using a hemolysis method with photosensitizers. These properties were demonstrated in vitro and live animal models.

Through this research, we suggest that sickle red blood cells may have the potential to be a new drug carrier with better tumor targeting and controllable drug release for improved chemotherapy in advanced cancer patients.

CHAPTER 1 INTRODUCTION

Systemic chemotherapy by intravenous administration has been one commonly used and standard method in the treatment of solid tumors due to the ease of administration, rapid reaction, and avoidance of the gastrointestinal tract (GI tract) problems with oral drug administration [1]. Generally, multiple cycles of chemotherapeutic treatments are required because the efficacy of treatment is directly proportional to the given drug concentration in target sites [2]. Despite impressive progress in development of chemotherapeutic agents, most challenges remain such as inadequate therapeutic agent doses to the tumor sites by inaccurate delivery and adverse toxic effects on normal organs (systemic toxicity). For example, highly proliferative normal cells such as bone marrow and GI mucosa are susceptible to the fatal cytotoxicity of chemotherapeutic agents and reveal the adverse side effects such as a dose response effect by indiscriminate distribution of administered drug.

Therefore, new drug delivery strategies that can improve therapeutic index and adequate concentration of drug delivery to tumor sites are needed [1, 2].

Current Drug Delivery Strategies to Tumors

Numerous drugs have been developed for chemotherapeutics, but the effective drug delivery system (DDS) of therapeutic agents to tumors has been limited [3]. Among various approaches to specific DDS to tumor sites, two targeting methods seem to be most general in clinical trials and practice and summarized in Table 1-1.

Active targeting employs molecular interaction in pairs of specific antigen / monoclonal antibody, ligand / receptor and aptamer / counter part between on the surface of pharmaceutical carriers and in targeted cell sites [3, 4].

Table 1-1. Drug delivery systems (DDS) in clinical trials and practice (adapted from [5])

Name	Type of DDS	Type of targeting	Stage of approval for clinical practice	Therapeutic agent
Doxil	Liposome	Passive	Approved for clinical use	Doxorubicin
DaunoXone	Liposome	Passive	Approved for clinical use	Daunorubicin
Abraxane	Albumin-based polymer	Passive	Approved for clinical use	Paclitaxel
Bexxar	Immunoconjugate	Active	Approved for clinical use	Radioactive iodine
SMANCS	Nanopolymer	Passive	Approved for clinical use	Neocarzinostatin
NK105	Micelle	Passive	Phase 2	Paclitaxel
Xyota	Nanopolymer	Passive	Phase 3	Paclitaxel
MBP-426	Liposome	Active	Phase 1	Oxaliplatin

An example of active targeting is the binding of folate to pegylated particles for interaction with the folate receptor. The cells of many cancers overexpress folate receptors on their surface and have a higher binding affinity for the nanoparticle folate bound protein than for free folate [6]. However, the rapid clearance of ligand directed immunoliposomes owing to non-specific uptake by the cells of reticulo-endothelial system (RES) reduced the therapeutic efficacy [7, 8]. Antibodies conjugated with liposomes limit targeting to intravascular targets due to the increased size of the liposomes and reduced release rate of entrapped drugs [9].

On the other hand, passive targeting employs the prolonged circulating time of the drug carriers in the blood stream with reduced accumulation in the normal organs and sufficient levels of accumulation in tumor sites through the enhanced permeability and retention (EPR) effect [3, 4]. Longevity of drug carriers in the circulation increases the probability for drug-loaded carriers to find large fenestrations on the blood vessels with modest loss of drug concentration during circulation in the blood stream.

Enhanced Permeability and Retention Effect Based Passive Targeting to Solid Tumors

The EPR effect is the mechanism by accumulation of macromolecular prodrugs in sites of inflammation or cancer by increased vascular permeability. In 1986, EPR effect was described by Matsumura et al. and was attributed as the basis for the selective targeting of macromolecular drugs to the site of solid tumors [10]. In their experiment, Evans blue (which forms a noncovalent, macromolecular complex with albumin) showed decreased clearance rate from tumor tissue for 3-4 weeks compared with healthy tissue less than 1 week [10]. In addition, one study reported that EPR is affected by the tumor size, with a greater EPR in smaller tumors, probably because the greater vessel density as compared to larger tumors containing an avascular region [11].

Tumor cells tend to aggregate when they proliferate. When the mass of tumor cells reach 2-3mm in diameter, angiogenesis is induced because of the excessive nutrition and oxygen demands of the growing tumors [12]. As opposed to normal neovasculature, tumor neovasculature differs greatly in anatomical structure [13]. For instance, the tumor vasculatures are characterized by higher vascular density, unorganized vascular distribution, uneven diameter of blood vessels, and higher permeability with large fenestration [14].

The pores caused by this discontinuity of endothelium are involved in the enhanced permeability or leakiness in tumor microvasculature. Hobbs et al. and Yuan et al. determined the pore size of tumor vasculatures using transplanted murine tumors [15-17]. It varied from 100 to 780 nm in diameter depending on the anatomic location of the tumor and tumor growth. On the other hand, the fenestration in normal microvasculature with the tight junctions was usually less than 2nm [18] and larger at up

to 6nm in postcapillary venules [19]. Additionally, discontinuous endothelium existing in the kidney glomerulus and the sinusoidal endothelium of the liver and spleen are ranging from 40 to 60nm in width and up to 150nm in width, respectively [20]. Therefore, the major pathway of drug transport across tumor microvascular wall is by extravasation via diffusion and/or convection through the discontinuous endothelial junctions in solid tumors. Also, poor lymphatic drainage in solid tumor decreases the clearance of macromolecular compounds from tumor interstitium [21-23]. Consequently, the anatomical and functional defectiveness in solid tumors result in extensive leakage of blood plasma components and enhanced retention in tumor tissues. This phenomenon was recognized as the EPR effect and EPR effect could be observed in almost all human cancers with except for prostate cancer or pancreatic cancer [24]. Accordingly, EPR effect became most commonly used term and predominant factor to increase specific tumor targeting therapy. The active targeting process cannot be separated from the passive because it occurs only after passive accumulation in tumors.

Additionally, elevated levels of growth factors such as vascular endothelial growth factor (VEGF) [25, 26], basic fibroblast growth factor (bFGF) [27], and other vasoactive factors (bradykinin and nitric oxide) were determined as compared to normal tissues. In Table 1-2, the factors responsible for the EPR effect of macromolecules in solid tumors are summarized. For instance, the overexpressed bradykinin cause vasodilatation and EPR effect in tumors [28].

The principle of the EPR effect has prevailed in numerous strategies including active targeting to overcome systemic delivery limitations [8].

Table 1-2. Factors responsible for the EPR effect of macromolecules in solid tumors (adopted from [29])

Anatomical factors
Extensive angiogenesis and high vascular density
Lack of smooth-muscle layer, pericytes, sporadic blood flow → passive dilation of vessels in the angiotensin-II (AT-II)-induced hypertensive state → more leakage
Defective vascular architecture → extensive leakage
Meager lymphatic clearance → enhanced retention of macromolecular drugs and lipid particles in the interstitium of tumors
Slow venous return → accumulation of macromolecules in the interstitium
Generation of permeability-enhancing factors
Vascular endothelial growth factor (VEGF)
Bradykinin (BK) and/or hydroxypropyl BK
Nitric oxide (NO)
Peroxynitrite (ONOO ⁻), a reaction product of superoxide radical and NO
Prostaglandins (PGs)
Matrix metalloproteinases (MMPs) → proMMP is activated by ONOO ⁻
Other proteinases (e.g. kallikrein system) → involved in various protease cascades
Other cytokines (e.g. tumor necrosis factor, interleukin-2) → facilitate EPR effect

For example, many drug carriers including nanoparticles [6], polymer micelles [30], polymeric conjugate [31], lipid microemulsion [32], liposomes [33], and resealed erythrocytes [34] have been developed based on EPR effect of solid tumors.

In Table 1-3, commonly used DDSs are summarized and compared to other carriers and RBCs. Among current drug delivery system (DDS), red blood cell (RBCs) carriers have longer half life in blood stream than others. RBCs could be potential drug carriers if carrier longevity in the circulation is considered a crucial value in passive targeting because the accumulation of drug carriers is slow, occurring and stabilizing over 1-2 days by passive targeting methods [29, 35].

However, studies of cytotoxic chemotherapy have revealed that the adverse side effects into normal cells, low concentration level of packaging of the drug into drug carriers, slow non-specific degradation of carriers, and uncontrolled and passive drug release in tumor sites are the key obstacles in conventional chemotherapeutics [2].

Table 1-3. Comparison of carrier erythrocyte to other DDS in mouse model (adapted from [35])

Carriers	Size [nm]	Shape	Half-life in blood	Diffusion in tissues
Murine RBCs	5,000~7,000	Biconcave disc	10~15 days	RES openings
PEG-Liposomes	50~500	Spheres	3~6 hours	Tumors (EPR), endocytosis
Polymersomes	50~500	Spheres	10~20 hours	Tumors (EPR), endocytosis
Filomicelles	40x20,000	Filaments	1~3 days	Unknown, possibly EPR
Polymer micelles	20~300	Spheres	0.1~6 hours	Tumors (EPR), endocytosis
Proteins and conjugates	5~5,000	Irregular sphere	10 min~6 hours	Diffusion and endocytosis

Reddy [2, 8, 36] described that solvents or stabilizers for nanoparticles possibly caused toxicity during nanoparticle production so that consistent and stable substances are needed. Andreson *et al.*[8], Chen *et al.*[37], and Pakunlu *et al.* [38] demonstrated that liposome-based formulations could decrease the systemic cytotoxicity in normal sites, but its rapid clearance owing to non-specific uptake by the cells of RES reduced the therapeutic efficacy. Also, several limitations including insufficient accumulation level of drug carrier and drug release into the tumor sites were observed by synthetic drug carriers [8].

Resealed Erythrocytes as a Drug Carrier

Among drug carriers, erythrocytes (non-nuclear biconcave discs with a thickness ~2 μm , a diameter ~7 μm and plasma membrane surface area ~160 μm^2) loaded by therapeutic agents have been exploited extensively for both temporally and spatially controlled chemotherapeutic carriers. The erythrocytes have been given the furthestmost interests for their potential applications because of various advantages. The advantages and limitations for erythrocytes as intravenous drug carriers are summarized in table 1-4.

Briefly, its relatively long lifespan [39, 40] compared to other drug delivery systems (i.e., <10 hrs for PEG-modified liposomes) was considered as a crucial feature for the passive targeting because the accumulation of drug carriers is slowly occurring and stabilized over 1-2 days by passive targeting method [29, 35]. In addition, restriction of unwanted extravasation except hepatic sinuses and interstitium in the splenic follicles [35, 39, 40], high biocompatibility without any undesired immune responses and biodegradability by macrophages [41, 42]. These promising features of analogous RBCs have been attracting more interest as intravenous slow release carriers in numerous animals [43-45] and human studies [45].

Gardos tried to encapsulate ATP into human erythrocytes for the first time in 1954 [46]. Nineteen years later, Ihler et al. first used the human erythrocyte as the carrier to deliver enzymes in the human body to heal certain diseases successfully [47]. Consequently, various types of erythrocytes from human beings [48] and different animal species, such as rats [49], mice [50], rabbits [51] and dogs [52], were applied to deliver antineoplasms [53], antiparasitics [54], antiretroviral agents [45], vitamins [55], steroids [56], antibiotics [57] and cardiovascular drugs [58].

According to previously documented examples regarding drug loaded normal RBCs, osmosis-based techniques including hypotonic hemolysis, hypotonic dilution, hypotonic dialysis, hypotonic preswelling, and osmotic pulse have been developed and popularly applied with high entrapment efficacy so far [41, 59-61]. Various hypo-osmotic lysis methods are reviewed in table 1-5.

Table 1-4. Advantages and disadvantages of erythrocytes in drug delivery (adopted from [34])

Advantages
A remarkable degree of biocompatibility
Complete biodegradability and the lack of toxicity resulting from the carrier degradation
Avoidance of any undesired immune responses against the encapsulated drug
Considerable protection of the organism against the toxic effects of the encapsulated drug, e.g., antineoplasms
Longer life-span of the carrier erythrocytes in circulation
An easily controllable life-span within a wide range from minutes to months
Considerably uniform size and shape
Protection of the loaded compound from inactivation by the endogenous factors
Possibility of targeted drug delivery to the RES organs
Relatively inert intracellular environment
Wide variety of compounds with the capability of being entrapped within the erythrocytes
Possibility of loading a relatively high amount of drug in a small volume of erythrocytes
Disadvantages
Clearance by RES
The rapid leakage of certain encapsulated substances from the loaded erythrocytes
Several molecules may alter the physiology of the erythrocyte
Some inherent variations in their loading and characteristics
Possible contaminations

Since preswelling method shows relatively higher entrapment efficacy [62, 63], better survival rate in systemic circulation [62, 63], simpler preparation steps among osmosis-based loading methods [64] and minimal damage to cells during drug loading procedures [65], the preswelling method was selected in this experiment. Hypotonic preswelling method is derived from the fact that exposing RBCs in a hypotonic solution cause an enlargement of pores with diameters of 200 to 500Å (20~50 nm) in the membrane when it reaches lysis point [66]. At this point, instantly added aqueous solution of the drug can come across through these pores into the interior of the cells. A calculated hypertonic buffer is added to restore the tonicity and reseal the openings in membrane. Then, the cell suspension is incubated in 37°C for about 30min to reanneal the membrane and washed out twice to remove uncaptured drugs into RBCs [67]. Loss

of hemoglobin (Hb) and intracellular components during this loading procedures can be compensated by added aliquot of a hemolysate. The resealed erythrocytes that retain most of Hb and other cellular contents of normal erythrocytes are referred to as “engineered erythrocytes” or “resealed erythrocytes” [68] and such resealed cells have a circulation half life span comparable to that of normal cells [69].

Table 1-5. Comparison of various hypo-osmotic lysis methods (adapted from [62, 63])

Method	Entrapment efficiency [%]	Advantages	Disadvantages
Dilution method	1-8	Fastest and simplest especially for low molecular weight drugs	Entrapment efficiency is less
Dialysis method	30-50	Better in vivo survival of erythrocytes better structural integrity of membrane	Time consuming heterogeneous size distribution of resealed erythrocytes
Preswelling method	30-90	Good retention of cytoplasm constituents and good survival in vivo	
Isotonic osmotic lysis method		Better in vivo surveillance	Impermeable only to large molecules, process is time consuming

Sickle Red Blood Cells as a Potential Drug Carrier

Sickle cell disease (SCD) is one of the most prevalently inherited hemolytic anemia in the United States [70]. It affects approximately 70,000 - 100,000 people of predominantly African descent in the United States. However, Caribbean, East Indian, Arabian, Mediterranean, and South and Central American decent also have high risk genotypes as well [71]. It also affects millions of individuals worldwide in regions with endemic malaria, such as Africa, the Middle East, and India [70, 71].

A single amino acid substitution (Glu→Val) on the β -globin chain of HbS results in mutated sickle hemoglobin (HbS). This mutation causes polymerization of HbS, damage to the membrane and cytoskeleton of RBCs, massive cation loss, and increased erythrocyte surface expression of adhesion molecule receptors in the presence of decreased pH and hypoxic conditions. These abnormalities result in decreased deformability, increased rigidity and viscosity, and dehydration of sickle RBCs (SSRBCs) [72-76]. The mechanical events lead to hemolysis, reticulocytosis, anemia, vaso-occlusive events, reperfusion injury, accumulation of sickle red cells to endothelium, and red cell oxidative stress which play a role to increase oxidative stress and reduce nitric oxide (NO) bioavailability [77, 78]. These pathophysiologies in SCD cause avascular necrosis, abnormal blood cell-endothelium interactions, inflammation, infarction and end organ failures [78-81]. Pathophysiology of vaso-occlusion by SSRBCs is shown in Fig. 1-1.

It is well known that most tumors are hypoxic and have a lower (more acidic) extracellular pH due to low vascular density, poor vascular organization, irregular vascular geometry, build up of products of metabolism (i.e., lactic and carbonic acid) and unbalanced oxygen consumption [82-84]. Accordingly, the hypoxic environment in tumor microvasculature could increase HbS polymerization and lead to form long polymers that distort shape and change flexibility of SSRBCs.

In addition, matured SSRBCs express a number of adhesion receptors interacting to endothelial cells such as B-CAM/Lu, LW (ICAM-4), and CD47 [85]. Zennadi et al. and Kaul et al. showed that overexpressed LW on SSRBCs was a major receptor for endothelial $\alpha_v\beta_3$ integrins contributing to the adhesion in animal models [86-88].

Interestingly, $\alpha_v\beta_3$ integrin was recognized as one of the overexpressed counter-receptors in tumor microvascular endothelial cells through in-vivo screening by Arap et al. [89]. Accordingly, SSRBCs may have a promising combination of molecularly and mechanically accumulative factors as a new tumor-targeting carrier with preferential accumulation in tumor sites.

Tumor-preferential accumulations by SSRBCs under the hypoxic tumor environment were reported previously. For example, Brown et al. demonstrated that exogenously administered SSRBCs from human SCD patients loaded with Gd-DTPA using hypo-osmotic lysis method preferentially aggregated in orthotopic 9L glioma brain tumors in a rat model [90]. On the other hand, SSRBCs less than 30% of total circulating RBCs rarely accumulated in normal physiological condition. In addition, Milosevic et al. reported case study regarding a 63 year-old African-American female patient with an advanced squamous cell carcinoma cervical cancer [91]. Normally, patients with sickle cell trait do not have anemia and need neither treatment nor occupational restrictions because the cellular concentration of HbS is too low (less than 50%) for polymerization to occur [92]. However, the polymerization under hypoxic and acidic conditions was confirmed by tumor punch biopsies [91].

Controlled Drug Release by Photoactivation using

It is well-known fact that it is almost impossible to achieve sufficient therapeutic concentration of drug at the tumor site by passive diffusion release without damaging healthy tissues when traditional systemic chemotherapy is performed. A possible solution is to encapsulate anticancer drug into specific drug carrier with preferential accumulation in tumor sites and release drug from carrier when it reaches at target sites. Preferential accumulations of SSRBCs in tumor microvasculature were shown above

due to the adhesive interaction between molecular receptors on the membrane surface and counter-receptor on endothelial cells. In addition, physical changes of microvascular structure in tumor sites enhanced polymerization of SSRBCs resulting in the accumulation by hypoxic condition.

Various methods have been studied for slow efflux of encapsulated drug from RBCs. The most important parameter for evaluation of such resealed erythrocytes is the drug release pattern [42, 65], but release rates vary according to the nature of the encapsulated drug (i.e., polarity and molecular weight) [41, 66]. In addition, uncontrolled slow release of drug from carriers with prolonged lifespan does not always show the greatly increased therapeutic efficacy [93]. Therefore, several approaches to trigger drug release in a controlled manner were proposed by specific stimuli such as magnetic field guided ultrasound [94] , light [95-97], and temperature [98] over the targeted sites. However, these methods may be restricted to only clinically identified tumor sites, not for randomly disseminated advanced solid tumors [8]. In addition, only targets within an appropriate penetration depth of the stimulus source may be affected.

In response to this challenge, light-activated controlled release method by photosensitizers is employed to control release from resealed SSRBCs. Flynn et al. demonstrated the directly photo-dependent release of entrapped thrombolytic agent brinase from photosensitized RBCs by exposure of radiation from a 10mW HeNe laser placed 17cm above the sample [97]. Moreover, they developed the loading erythrocytes with chemotherapeutic agent (methotrexate) for chemotherapy and subsequently performed photoactivation by hematoporphyrin [95]. Continuous laser stimulus enhanced rapid drug release and then caused decreased Hela cells viability.

Photohemolysis reaction of photoactivated RBCs was more precisely analyzed by Al-Akhras et al. in 1996 [99]. A basic photohemolysis from photosensitized RBCs requires two distinct steps; photochemical and thermal reactions. Continuous photohemolysis (CPH) measurement is assumed that photohemolysis is attributed to cooperative photochemical and thermal reactions simultaneously. On the other hand, in delayed photohemolysis measurement (DPH), the photochemical reaction is followed by thermal reaction in dark sequentially. The lysis time, which is the time measured from the start of rupturing the RBCs, was measured from the beginning of irradiation for CPH method and incubation in dark for DPH method [100]. During the incubation step in DPH, the lysis that occurred during the increase in incubation temperature up to physiological temperature in the dark was considered as insignificant offset and ignored. Photohemolysis rate was measured by the absorbance of released Hb in supernatant separated by immediate centrifugation using spectrophotometer and a typical photohemolysis curve has a sigmoidal shape as in Fig. 1-2.

Fig. 1-2 showed an example of DPH measurement of bovine RBCs in vitro by Al-Akhras et al. [101]. Based on DPH method, photochemical reaction occurred by irradiation for a defined time interval at lower temperatures to avoid thermal activation, and then thermal reactions were initiated after the solution temperature reached physiological body temperature in the dark. The lysis that occurred up to when the temperature reached 37°C was considered as negligible offset. As shown in Fig. 1-2, DPH was adjustable by only changing radiation time and it demonstrated the controlled Hb release from photoactivated bovine RBCs [101]. Similarly, DPH method may be applicable to perform in-vivo experiment using SSRBCs.

For in-vivo experiment, photochemically activated SSRBCs loaded with therapeutic drug by hypo-osmosis method may be injected in human or animal model. Preferentially accumulated SSRBCs at tumor sites may be observed according to the reasons described in previous sections. Drug release is initiated by thermal reaction due to the body temperature and temporally controllable drug release rate by the adjustment of irradiation time may occur at local tumor sites resulting in a higher peak drug concentration.

To characterize the released drug concentration rate in a live model, Gompertz function is adapted to examine the characterization in-vitro DPH effect by photoactivated SSRBCs in this experiment. The Gompertz function shows a similar fitting curve as multi target theory described previously [99]. Using this function, estimated DPH measurements at presumed time points were successfully matched with empirical results [101].

Gompertz Function

Gompertz function is also known as Gompertz's law of mortality especially for the elderly mortality rates in 1825 [102] and is determined as follows:

$$M(t) = \alpha e^{\beta t} \quad (1)$$

where $M(t)$ is the mortality rate at a given age t with parameters α and β . The parameter α determines the intercept of the curve, also referred to as the basal mortality rate, and is usually set at adolescence. The parameter β determines the rate of increase of the mortality rate over age. This simple model yields a sigmoidal mortality rate curve which shows accelerating growth for younger age and decelerating growth for older age as shown in Fig. 1-3.

Hemolysis rate of photosensitized RBCs by hypericin and Photofrin showed similar sigmoidal shape as previously described [99] and Gompertz function was selected as the most applicable function describing photohemolysis process with only two parameters by Al-Akhras *et al.*[101]. A slightly modified Gompertz function was defined as follows:

$$H = H_0 e^{-ae^{-bt}} \quad (2)$$

where H is the percentage of hemolysis during the incubation time t (the time measured from start of rupturing the RBCs at dark incubation), H_0 the initial maximum number of cells, normalized to one, a is a fractional hemolysis ratio and b is the rate of fractional hemolysis change. The theoretical time required for 50% fractional photohemolysis (t_{50}) could be calculated by equation (3).

$$t_{50} = \frac{\ln\left(\frac{0.693}{a}\right)}{-b} \quad (3)$$

The theoretical values of t_{50} from the equation was compared with the empirical t_{50} . This functional parameters a, b , and t_{50} were important parameters to estimate the average of empirical DPH rate and this model has been assessed to investigate the hemolysis rate of photosensitized RBC by PpIX.

Microdialysis Method for in-vivo Delayed Photohemolysis Measurement

Microdialysis methodology, based on the dialysis principle, has been a powerful sampling technique capable of continuous monitoring during several hours and days the concentration of unbound drugs or biological molecules both for in-vitro and in-vivo investigation of both endogenous and exogenous substances [103, 104]. Although it was originally developed to monitor for neurotransmitter concentrations in animal brain in 1972 [105], it has been applied and broadened for various pharmaceutical researches

including the transdermal delivery of drugs [106], tissue pharmacokinetics [107], and tissue pharmacodynamics [108, 109]. In addition, microdialysis monitoring has been employed in various tissue and organs of human or murine models such as liver [110], heart [111], skin [109], blood vessels [112], placenta [113], stomach [114], ear [115], and tumor tissue [116-118].

Fig. 1-2 shows the microdialysis sampling process. Briefly, the probe consists of a semipermeable hollow fiber membrane with a specific molecular weight cutoff connected to an inlet and outlet tubing. The probe is implanted in the region of interest and then is continuously perfused with an equivalent fluid (i.e., Ringer's solution), termed the perfusate, to the extracellular fluid (ECF) surrounding the probe. Lower molecular weight compounds than the membrane cutoff are able to diffuse into or out of the probe lumen in both directions in response to concentration gradients. The collected solution that exits the probe, the dialysate, can be analyzed using quantitative techniques like high performance liquid chromatography (HPLC) [119].

Using microdialysis methodology, fluorescence intensities of the collected dialysates from tumors were compared to healthy muscle tissues by microplate reader at two different time points. The ratio of the released calcein concentration from resealed SSRBCs in tumors to healthy tissues was determined and compared. The controllability of release time for calcein from photoactivated SSRBCs and possible systemic toxicity caused by SSRBCs were evaluated from the numerical comparison.

Table 1-6. Summary of advantages and limitations of microdialysis sampling technique
(adopted from [120])

Advantages
Determination of the bioactive concentration of the drug in the target tissue
Excellent time and spatial resolution
Protein free samples
No further enzymatic degradation of the drug
On-line coupling of analytical determination
No fluid loss
Simultaneous collection of endogenous compounds
Monitoring of drug time course in different tissues by multiple microdialysis probes

Disadvantages
Tissue damage by probe implantation
Diluting effect of the microdialysis procedure
Need of high sensitive analytical methods, specially for drugs with high protein binding
Necessity of determination of the in vivo recovery during the experiment
Sticking of lipophilic drugs to tubing and probe components
Low recovery of large molecules

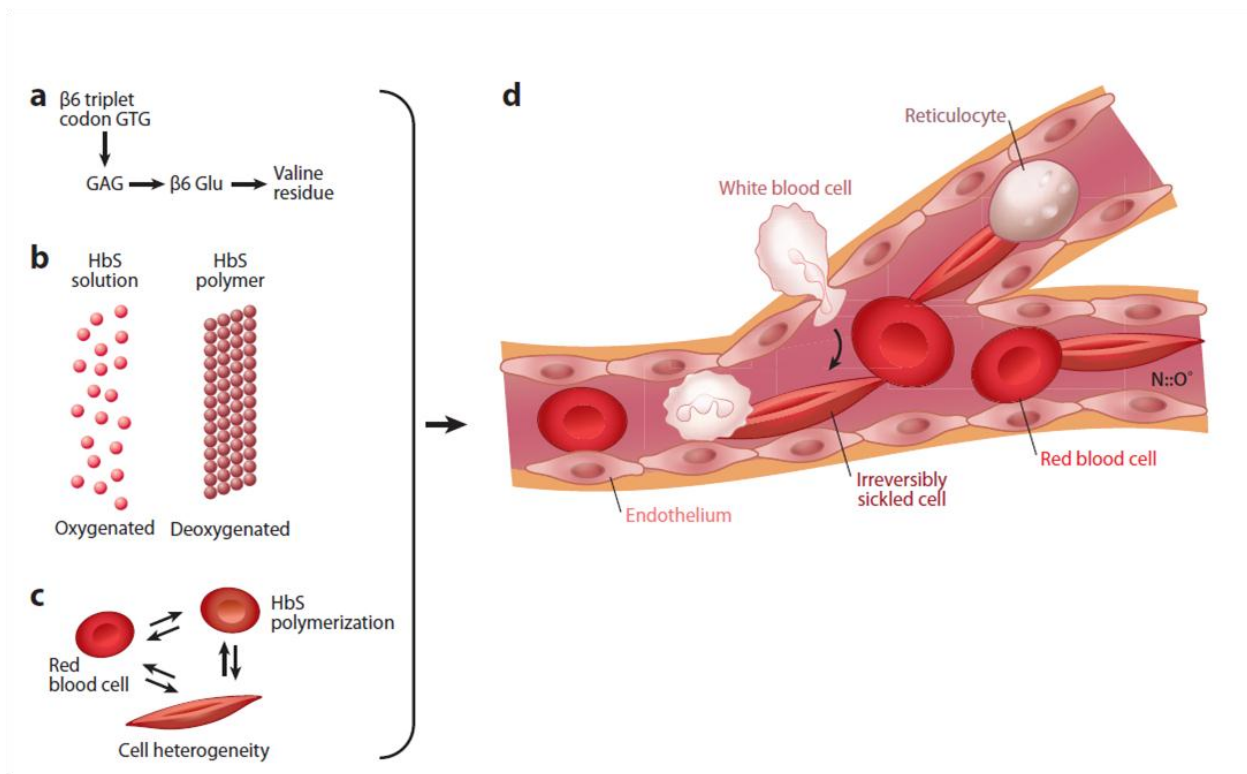


Figure 1-1. Pathophysiology of vaso-occlusion by SSRBCs. (a) Point mutation in sickle cell disease. (b) Polymerization of HbS under deoxygenation. (c) Red blood cell shape change in response to HbS polymerization. (d) Cells in microvasculature. Abbreviation: N::O*, nitric oxide bioavailability. Reticulocyte accumulated to endothelium initiates vaso-occlusion by trapping irreversibly sickled cells and forming aggregates with white blood cells (adapted from [121]).

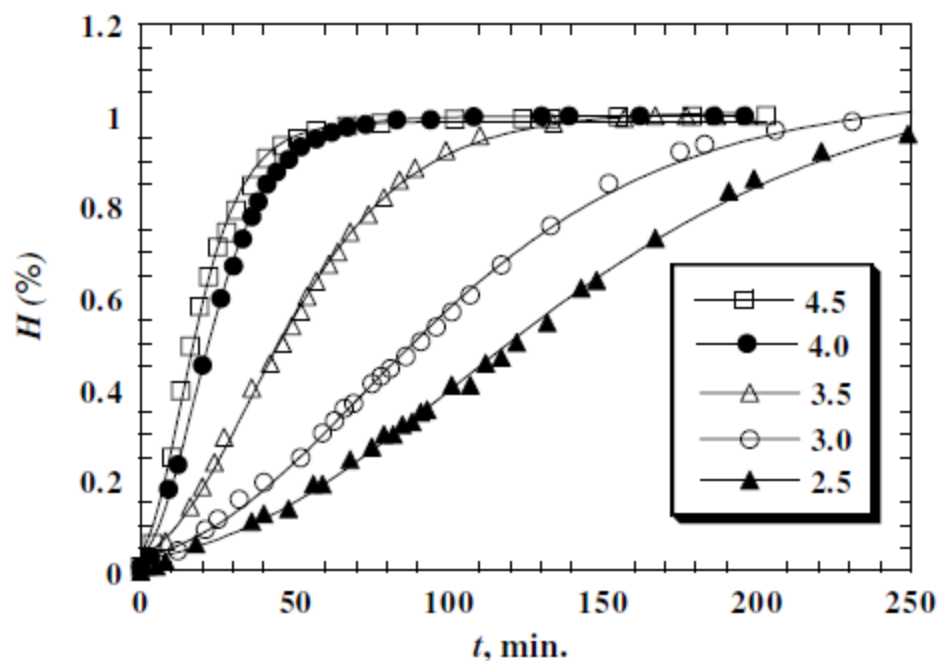


Figure 1-2. DPH measurement from photoactivated RBCs by PpIX with 10 μ M. Different irradiation time was applied with Hg-Xe arc lamp at 24°C and incubated at 24°C. The cell were irradiated for open circle 4.5, open square 4.0, open diamond 3.5, open triangle 3, and inverted triangle 2.5 min. (adapted from [101])

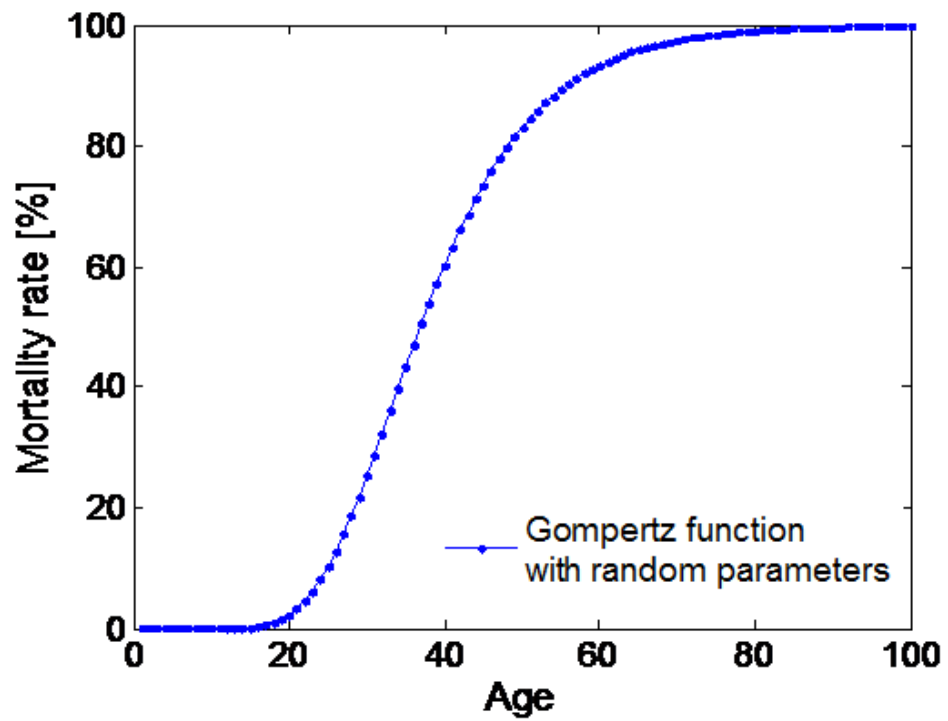


Figure 1-3. Example plot of age-specific mortality rates with random parameters by Gompertz function.

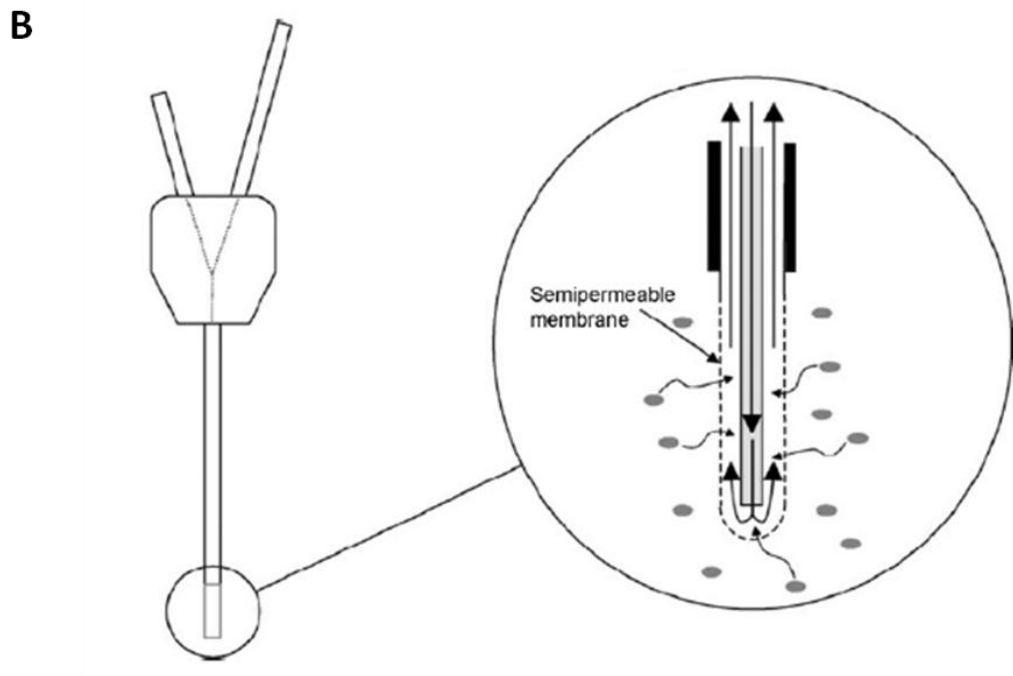
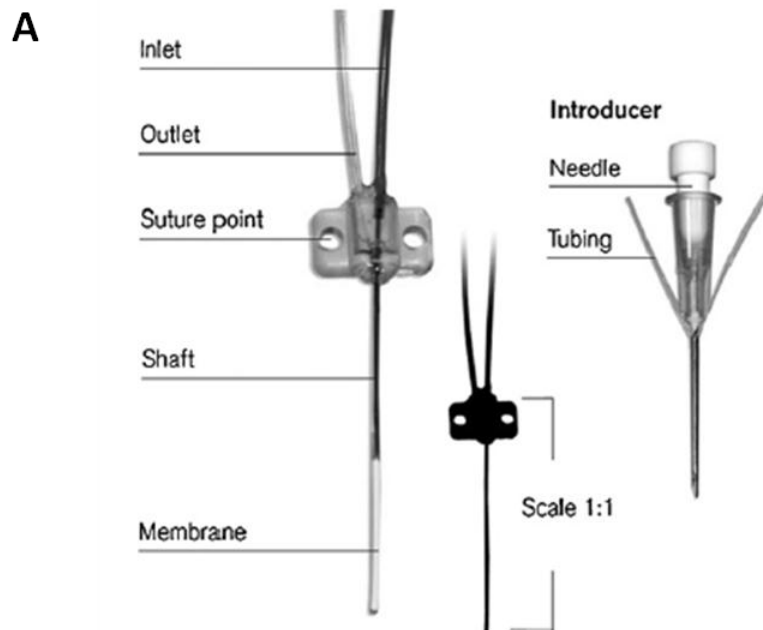


Figure 1-4. Typical microdialysis probe configurations and sampling process. (A) flexible CMA probe from CMA product catalogue. (B) Sampling process across microdialysis probe membrane from [104]. A perfusion fluid that closely matches the ionic strength and composition of the fluid external to the microdialysis membrane is passed through.

Motivation and Goal of this Study

Numerous drug carriers such as liposomes, nanoparticles, and polymers for cancer chemotherapy have been investigated to protect normal tissues from toxic drugs to treat advanced stage malignant cancer. However, currently conventional drug carriers are not free from systemic cytotoxicity, thus therapeutic efficacy is limited by insufficient tumor accumulation of the drug carrier and insufficient drug release into the tumor sites [2, 8]. Therefore, alternative drug carrier system is required with effective tumor targeting and controlled drug release rate.

SSRBCs may have the potential to be used as a novel drug carrier. According to previous researches, SSRBCs from human SCD patients and animal models caused vaso-occlusive events in the deoxygenated microvasculatures [72-76]. For example, exogenously administered SSRBCs from human SCD patients demonstrated preferentially aggregated in orthotopic 9L glioma brain tumors in a rat model [90]. In addition, RBCs in a female patient with sickle cell trait were accumulated in the blood vessels near an advanced squamous cell carcinoma cervical cancer [91]. Therefore, SSRBCs may have natural tumor preferential accumulation characteristics due to hypoxic circumstances caused by unbalanced oxygen consumption in tumor sites [82-84]. Moreover, temporally controlled drug release mechanisms from resealed RBCs were described and performed ex-vivo [99-101]. To characterize Hb release model, Gompertz function was applied for its numerical analysis to estimate DPH measurement [101].

According to these evidences, in this research, it is hypothesized that SSRBCs may have the potential to be a new drug carrier with better tumor targeting and controllable drug release for improved chemotherapy in advanced cancer patients.

CHAPTER 2 MATERIALS AND METHODS

Window Chamber Installed Mouse Model

Intravital microscopy in window chamber installed animal model allows non-invasive, high-resolution studies of tumor pathophysiology and interaction with therapeutic and diagnostic nanoparticles in solid tumors. For these reasons, it is an attractive complementary imaging technique to clinical and preclinical in-vivo imaging modalities such as magnetic resonance imaging (MRI), computed tomography (CT), positron emission tomography (PET), and whole body fluorescence imaging [122].

Historically, the window chamber was installed in rabbit ears in 1924 [123] and then this technique was employed for study of the tumor vasculature in a hamster cheek pouch window chamber in 1965 [124]. From that time onward, various chambers such as the mammary imaging window, cranial window chambers, and dorsal skinfold window chambers have been developed for tumor research on hamsters, rats and immunodeficient mice [125-131]. Especially, intravital microscopic studies in dorsal skinfold window chamber installed animal models with growing solid tumors provide unique functional and morphological information. For example, microvascular morphology and function [132, 133], vascular and physiological response to conventional therapies [134, 135], the extracellular matrix components [136, 137], pH and pO_2 [138], growth factor signaling and tumor host interaction [139, 140], and molecular and nanoparticle dynamics [141, 142] were able to be studied.

In this experiment, the tumor bearing immunodeficient mice were surgically implanted with titanium dorsal skinfold window chambers. Transillumination and fluorescence intravital microscopy were employed to monitor the growth rate of tumors,

morphological changes of normal and tumor microvasculature, Hb saturation, blood flow, and localization / accumulation of fluorescently labeled target cells. The dorsal skinfold window chamber installed on an immunodeficient mouse model with growing tumors is shown in Figure 2-1.

Imaging System

A Zeiss microscope (Carl Zeiss, Incorporated, Thornwood, NY) is used as the imaging platform (Fig. 2-2). A 100W tungsten halogen lamp is used for transillumination of the window chamber, while for fluorescence images, a 100W mercury lamp is used for epiillumination. Spectral image datasets are acquired with a monochrome scientific grade CCD camera thermoelectrically cooled to -20°C (DVC Company, Austin Texas) and fluorescence images are acquired with an ANDOR iXon electron multiplying CCD (EMCCD) camera thermoelectrically cooled to -50°C (ANDOR Technology, South Windsor, CT). The long working distance objectives used are 2.5x and 5x Fluars, 10x EC Plan-NeoFluar, and a 20x LD-Plan-NeoFluar (Carl Zeiss, Inc., Thornwood, NY).

Hyperspectral image data are obtained using a liquid crystal tunable filter (LCTF, CRI, Cambridge, MA) with a 400–720 nm pass band and 10 nm nominal bandwidth. Fluorescently labeled macrophages and PLGA MPs are imaged using the EMCCD camera with a FITC filter set (Chroma Technology Corp., Rockingham, VT; excitation: 480 nm, with 20 nm bandwidth; emission: 550 nm, with 30 nm bandwidth) and a Cy5 filter set (Chroma Technology Corp., Rockingham, VT; excitation: 640 nm, with 20 nm bandwidth; emission: 680 nm, with 30 nm bandwidth), respectively. Additionally, fluorescently labeled RBCs with DiD (Carbocyanine dye 1,1'-dioctadecyl-3,3',3'-tetramethylindodicarbocyanine, 4-chlorobenzenesulfonate salt) are numerically analyzed using a Cy5 filter set (Chroma Technology Corp., Rockingham, Vermont,

excitation 640nm with 20nm bandwidth, emission 680nm with 30nm bandwidth). Further image processing is performed using Matlab (The Mathworks, Incorporated, Natick, Massachusetts).

Imaging Acquisition

LabVIEW (National Instruments Corp., Austin, TX) is used to prepare a custom designed virtual instrument for controlling the tuning of the LCTF and operation of the CCD camera. The software enables automated image acquisition using the specifications for camera exposure time and gain for each filter wavelength. Since the LCTF filter transmits less at lower wavelengths and more at higher wavelengths the exposure time for the camera has to be controlled such that the full dynamic range of the camera is utilized. The minimum exposure time used is 400ms whereas the maximum exposure time used is 1400ms, resulting in a typical acquisition time of approximately 16ms for image acquisition, filter tuning, image transfer, and saving images on external hard drive. One hemoglobin saturation (HbSat) image set comprised of 16 images are acquired in the wavelength range of 500-575nm with an interval of 5nm.

Hyperspectral Imaging of Hemoglobin Saturation map

Hypoxia caused by the unique characteristics of solid tumor sites such as lowered vascular density, irregular vasculature, longitudinal oxygen gradient, and unbalanced oxygen consumption has decreased therapeutic efficacy in several clinical trials (radiation, chemotherapy and surgery) [143, 144]. Hence, tumor oxygenation studies at microvascular levels are important to provide better understanding of the complexity of microvasculature oxygen transport and exchange with tissue. A known technique, polarographic microelectrodes, was employed to measure pO_2 at the microvasculature

level, but it is difficult to perform and does not provide significant spatial information of oxygen delivery [82]. On the other hand, hyperspectral imaging is able to provide spatial maps with hemoglobin saturation (HbSat) information for better understanding of the relationship between blood oxygen delivery and hypoxia at microvascular levels during tumor growth [145].

In our experiment, hyperspectral imaging is acquired by stack of spatial images with each image being acquired at a different wavelength (λ) as in Fig. 2-3 (A). Hyperspectral image data were collected using a LCTF with a 400–720 nm pass band and 10 nm nominal bandwidth. Band-limited images were acquired from 500 to 575 nm at 5 nm intervals to create HbSat pseudocolor maps from pure oxy- and deoxyHb reference spectra as described previously [145]

Image processing is performed using Matlab software (The Mathworks, Inc., Natick, MA) to create pseudocolor HbSat maps according to the flow diagram in Fig.2-3 (B). The HbSat values can be calculated from stack of spatial images at a different wavelength based on the following model equation using linear least squares regression [146].

$$A_\lambda = \log\left(\frac{I_0}{I}\right) = \varepsilon_\lambda^{\text{HbO}_2} \cdot [\text{HbO}_2] \cdot L + \varepsilon_\lambda^{\text{HbR}} \cdot [\text{HbR}] \cdot L + SL \quad (4)$$

where A_λ is the absorbance at wavelength λ , I is the pixel value, I_0 is the pixel value of reference light, $\varepsilon_\lambda^{\text{HbO}_2}$ and $\varepsilon_\lambda^{\text{HbR}}$ are the extinction coefficient for HbO₂ and HbR at wavelength λ , $[\text{HbO}_2]$ and $[\text{HbR}]$ are the concentrations of oxy- and deoxy-Hb, L is the pathlength, and S is a pathlength-dependent scattering term. Using this formulation, stack of hyperspectral images can be converted to a single HbSat map.

Delayed Photohemolysis Measurements

In-vitro Delayed Photohemolysis Measurement Systems

In-vitro SSRBCs DPH measurement system and techniques are similar to the experimental setup by Al-Akhras and Grossweiner and depicted in Fig. 2-3 [99, 100].

Photosensitized SSRBCs in 3ml of buffer are transferred in glass cuvette (Starna Cells, Atascadero, CA) and positioned in a temperature controlled cuvette holder (Ocean Optics, Dunedin, FL). The temperature-controlled holder for the cuvette can control temporal conditions from 4°C to body temperature. The cell suspension in the cuvette was irradiated by a 0.08W halogen lamp (Fiber lite DC-950, Dolan-Jenner, Boxborough, MA) through one face on an orthogonal face of the cuvette for various irradiation times to trigger protoporphyrin IX (PpIX) activation at room temperature. The SSRBCs solution is gently stirred with a magnetic stir bar to have uniform irradiation and to increase exposing cells to ambient air due to oxygen supply.

After the irradiation step, the temporal reaction by is initiated by increasing the temperature of cuvette holder up to body temperature (37°C) in dark. In the DPH method, photohemolysis rates are measured from the beginning of incubation in dark after irradiation period as discussed in previous chapter. When the temperature reached at 37°C, 30µl blood samples were collected at various time points from 0 min to 48 hrs. The collected blood sample was split into packed SSRBCs and supernatant by immediate centrifugation and then 20µl of supernatant was stored in conical tubes to measure the absorbance for fractional photohemolysis (absorbance) using a spectrophotometer (NanoDrop™ 1000, Nanodrop, Wilmington, DE). The fractional hemolysis was determined from the amount of Hb released into the solution normalized to an equivalent solution of fully lysed red blood cells.

The empirical results were analyzed by Gompertz function. Unknown parameters such as a and b from equation (2) were calculated to estimate the theoretical time required for 50% fractional photohemolysis (t_{50}) by equation (3). R^2 values were computed for the fit of the empirical t_{50} to the theoretical values of t_{50} by the Gompertz function.

In-vivo Delayed Photohemolysis Measurement using Microdialysis Tubing

To investigate the controlled release rates of calcein from photoactivated SSRBCs in tissues, microdialysis probes were inserted at the sites for collection of dialysate. Microdialysis probes and tubing connectors were soaked in Ringers's solution and ethanol for 5min before use. After that, the probes were perfused with Ringers's solution to purge air bubbles in tubing for 30min at a flow rate of $2 \mu\text{l min}^{-1}$ by syringe pump (BASi Syringe Pump, MD-1002, West Lafayette, IN). The probes were then placed 5mm below the surface for tumor tissue through a plastic guide cannula. A probe was placed into the quadriceps muscle as a control site through a small incision made on the skin of implantation site with a small scalpel blade. The probes were inserted in a similar way in tumor tissue and sutured to skin (Fig. 2-4). Dialysate samples were collected by perfusing with Ringers's solution at the rate of $1 \mu\text{l min}^{-1}$ during 4hrs intervals from the tumor tissue and the quadriceps muscle. Each sample was collected at a variety of time points after the photosensitized SSRBCs cells or free calcein injection via tail vein. Fluorescence signal of calcein collected from tumor tissue and quadriceps muscle was analyzed using a fluorescence plate reader (Synergy HT Multi-Mode Microplate Reader, Biotek, Winooski, VT) and compared with each group.

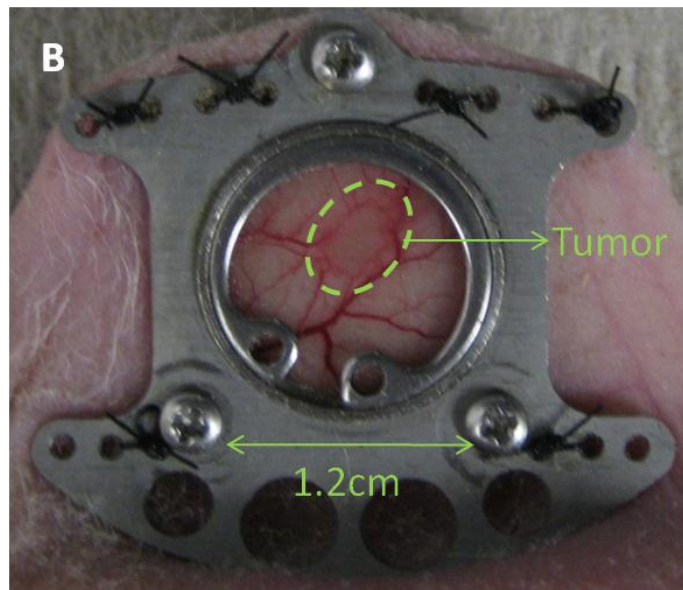


Figure 2-1. Window chamber installed mouse model. (A) Dorsal skinfold window chamber installed athymic (nu/nu) mouse. (B) A photograph of the 4T1 tumors growing at the implantation site in the window chamber indicated by the dashed circle, 5 days after implantation.

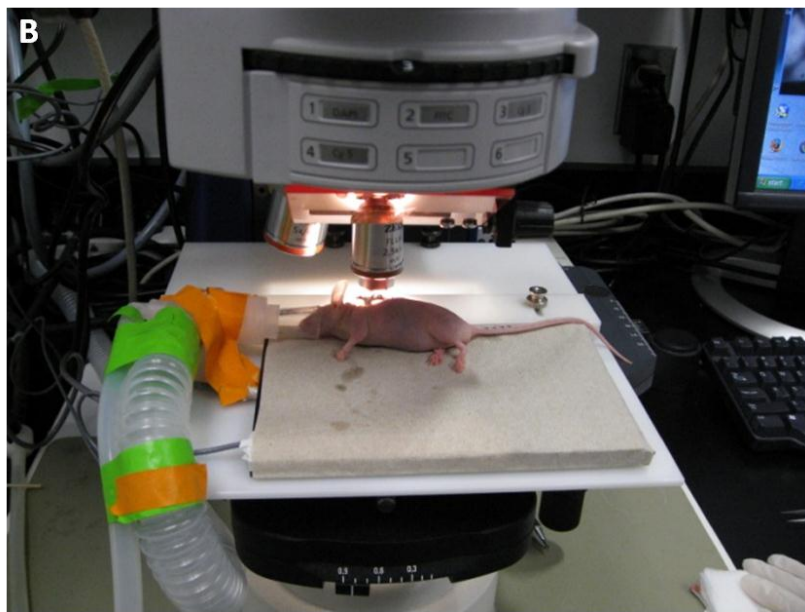


Figure 2-2. Hyperspectral imaging system. (A) The Sorg lab imaging system. (B) Window chamber installed mouse placed on the heating pad and anesthetized through the nose cone.

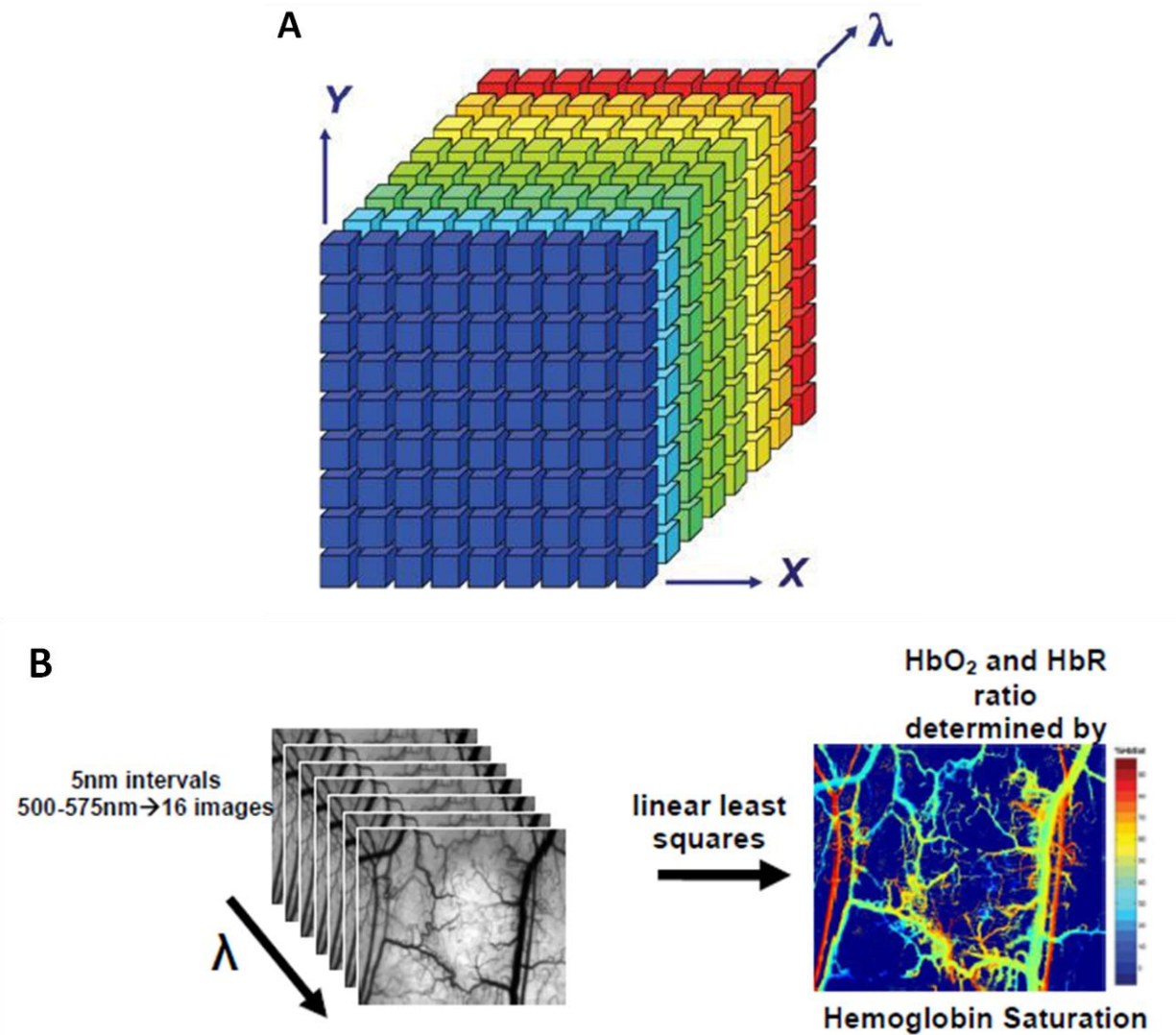


Figure 2-3. Hyperspectral imaging to create HbSat map (A) 3-D hyperspectral image cube represents a single image (x,y) at wavelength λ . (adopted from [147]), (B) Image processing method to obtain HbSat map from the stack of images that each image is acquired at different wavelength through hyperspectral imaging method.

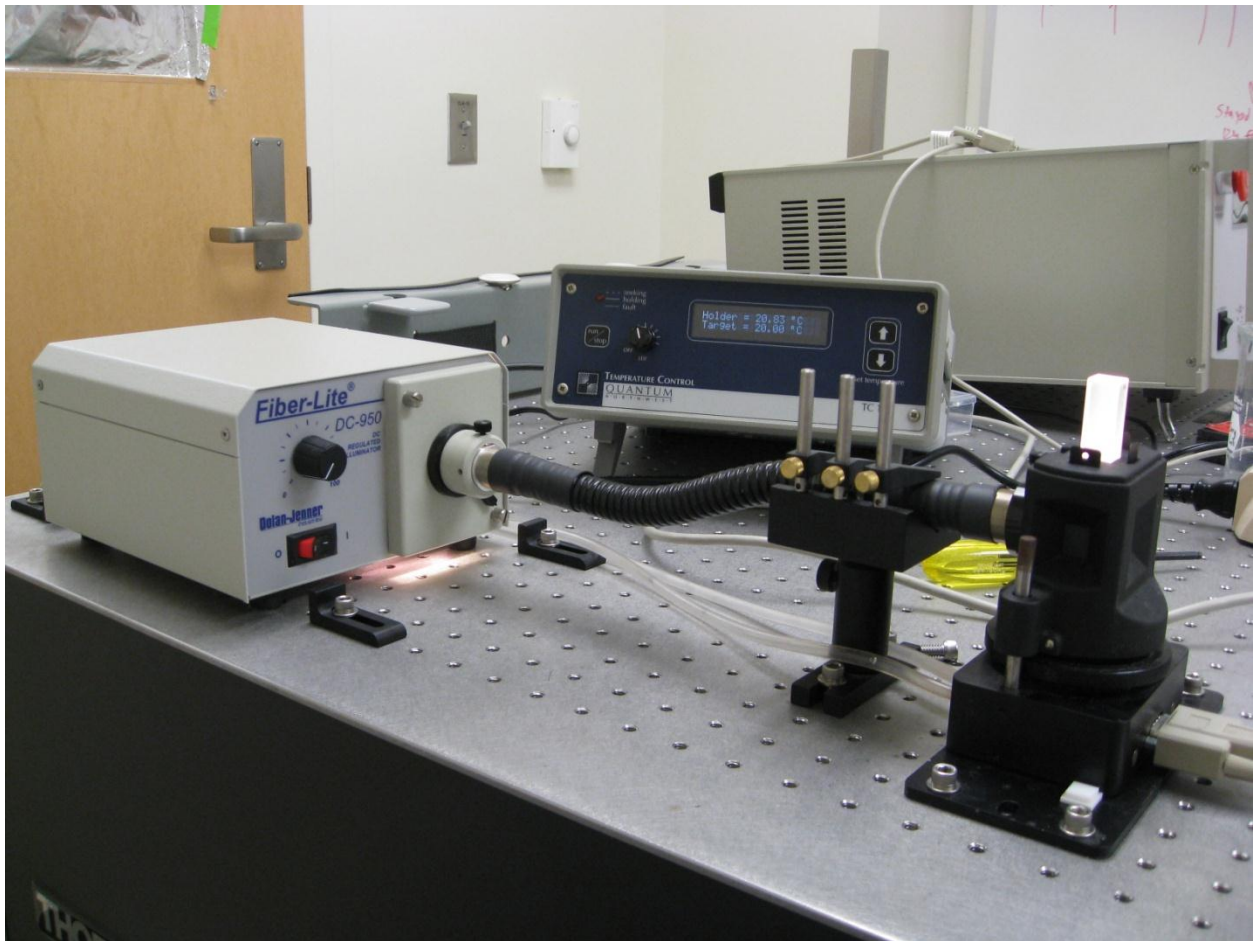


Figure 2-4. Experimental setup for in-vitro DPH measurements. The sample cuvette in temperature controller at under physiological temperature is exposed by 0.08W halogen lamp.

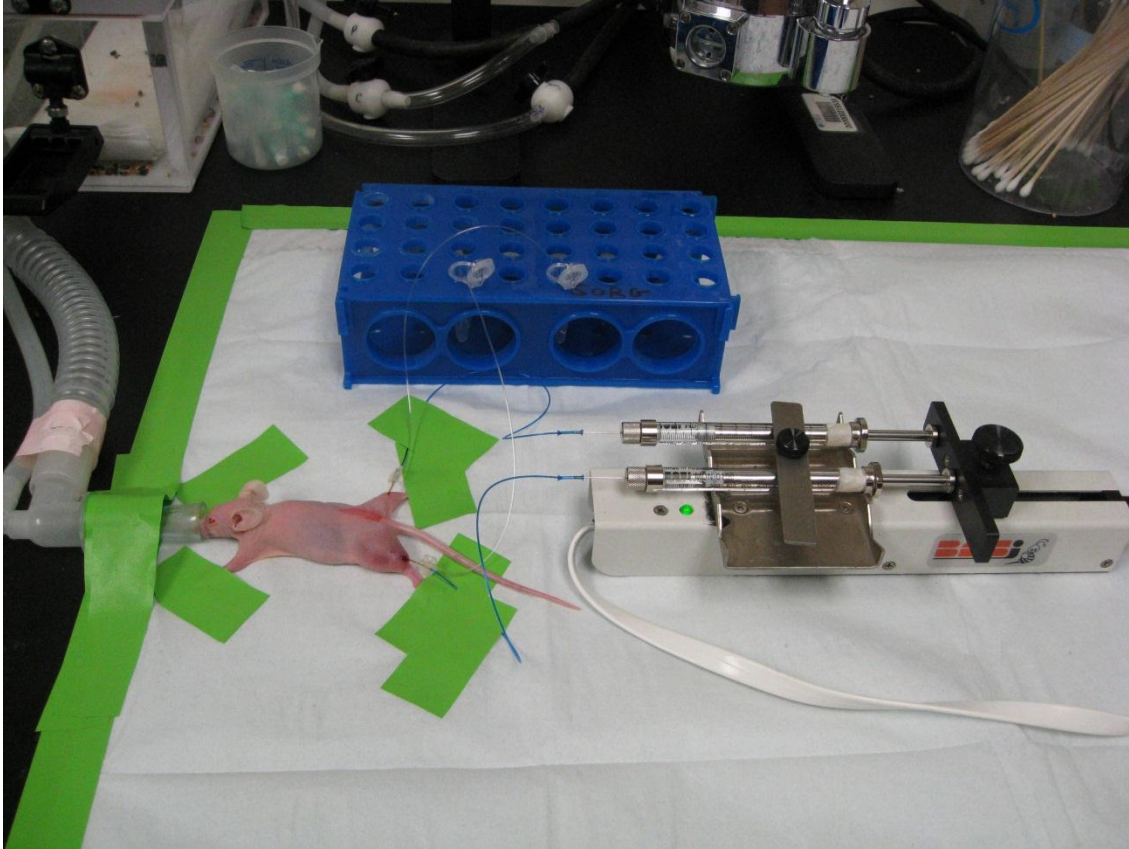


Figure 2-5. In-vivo DPH measurement setup with 4T1 tumor mass bearing mouse model. Each dialysate sample is collected at 0, 6, 12, and 24 hrs after the photoactivated SSRBCs or free calcein injection via tail vein.

CHAPTER 3 INTRAVITAL MICROSCOPY IMAGING OF MACROPHAGE LOCALIZATION TO IMMUNOGENIC PARTICLES AND CO-LOCALIZED TISSUE OXYGEN SATURATION

Polymer biomaterial particles have the potential to be used as drug delivery vehicles. Both hydrophilic and hydrophobic drugs can be loaded into polymer particles and administered by either the parenteral or oral route [148-156]. Several therapeutics, such as plasmid DNA, peptides, proteins and low-molecular-weight compounds, have been particle-loaded [148, 150, 154]. We are interested in particle-based methods of vaccination for optimizing the response of antigen-presenting cells, such as macrophages and dendritic cells, and minimizing adverse tissue responses to biomaterial polymer particles and encapsulated drugs or adjuvants [157-160]. One advantage of biodegradable vaccine carriers is that they can be designed to target antigen-presenting cells with differential timed release profiles with the potential to preclude the need for booster doses [148, 150, 151].

In the design of biomaterial particle-based vaccines it is important to consider the adaptive and innate immune responses to the vaccine and any potential adverse effects of immune response on local tissue at the vaccination site. For example, macrophages are antigen-presenting cells that can modulate both adaptive and innate immune responses to biomaterials, and activation of macrophages after phagocytosis of biomaterial microparticles (MPs) can result in an inflammatory response leading to reorganization of the tissue matrix [161]. Phagocytosis by macrophages can also induce a burst of reactive oxygen species (ROS), and excessive ROS production can lead to apoptosis [162]. In terms of macrophage function, it would be desirable for a biomaterial particle-based vaccine to stimulate the antigen-presenting behavior of macrophages

while inhibiting excessive ROS production and other inflammatory functions that are potentially damaging to local tissue.

We are interested in using intravital microscopy for investigation of immune cell localization and function and co-localized tissue effects in response to various biopolymer particle-based vaccine formulations, including encapsulated drugs, cytokines and adjuvants. Intravital microscopy has enabled investigations of various aspects of cell function in vivo for cells such as tumor cells and immune cells [127, 163]. Intravital microscopy with rodent dorsal skin window chamber preparations enables in vivo serial observations in the same animal over time [127, 163, 164], and these models have been used to study angiogenesis and macrophage response to implanted biomaterial scaffolds [156]. To our knowledge, however, there have been no reports in which intravital microscopy has been used to document real-time immune cell localization and co-localized tissue effects that give insight into potentially harmful immune cell function, especially in terms of endogenous biomarkers of inflammation with potential for clinical application.

Previously we have used spectral imaging of mouse window chambers to investigate tissue microvessel oxygenation changes from endogenous HbSat signals in response to tumor growth and development [145, 165, 166]. In the present proof-of-principle study, we used fluorescence and spectral imaging intravital microscopy of mouse window chambers to investigate macrophage accumulation and co-localized tissue microvessel HbSat changes in response to an inflammatory stimulus from MPs. Lipopolysaccharide (LPS), a coating found on the exterior of Gram-negative bacteria, was encapsulated in poly (D,L-lactide-co-glycolide) (PLGA) MPs to stimulate an innate

immune response [167]. Intravital fluorescence imaging was used to monitor localization of systemically administered fluorescent macrophages to fluorescent PLGA MPs and spectral imaging was used to measure the co-localized microvessel HbSat. This technique may enable investigations of specific immune cell responses to MP vaccine formulations while simultaneously monitoring potentially harmful tissue effects in order to optimize MP vaccine formulations.

Materials and Methods

Microparticles

PLGA (Lactel, AL) with 50:50 composition in hexafluoroisopropanol and inherent viscosity of 0.55–0.75 dl g⁻¹ was used to generate MPs of 1 µm diameter using a standard water–oil–water solvent evaporation technique [157]. The PLGA polymer was dissolved in methylene chloride at 20% (w/v) concentration. A primary emulsion was generated by mixing a fluorescent dye solution with the PLGA solution with or without LPS. A 100 µl aliquot of 5 mg ml⁻¹ fluorescein isothiocyanate (FITC) solution (Invitrogen) in phosphate-buffered saline (PBS) was mixed with 1000 µl of 20% PLGA solution using a tissue-miser homogenizer (Fisher Scientific) at a speed of 26,500 rpm for 60 s. To create MPs containing LPS, 100 µl of 1 mg ml⁻¹ LPS from *Escherichia coli* 026:B6 (Sigma–Aldrich) in PBS was added to the primary emulsion prior to homogenization. After the first homogenization, the primary emulsion was added to 10 ml of 5% polyvinyl alcohol (PVA, molecular weight ~100,000 g mol⁻¹) (Fisher Scientific) solution in PBS and the homogenizing was continued at 19,500 rpm for 60 s to form the secondary emulsion. The secondary emulsion was then added dropwise to 50 ml of 0.5% PVA solution to produce precipitate of particles. The precipitated particles were agitated using a magnetic stirrer (Fisher Scientific) for 3 h to evaporate residual methylene chloride. The

remaining solution was then centrifuged at 10,000g for 10 min to collect MPs. The supernatant was discarded and an equivalent amount of PBS was added. The MPs were resuspended in PBS by vortexing. This process of centrifugation and resuspension of particles was performed three times. The PBS was aspirated from the centrifuged MPs, which were then flash-frozen in liquid nitrogen and kept under vacuum in dry ice overnight to evaporate any water trapped in the MPs. The dried MPs were stored at -20°C until use.

The MPs were manufactured using methylene chloride which is toxic to living organisms and thus helps insure sterility of the particles during manufacturing of MPs. Sterility was preserved by using sterile solutions, glassware, etc. during the manufacturing process. In order to assess the amount of endotoxin present on the non-degraded blank MPs the chromo-Limulus amoebocyte lysate (chromo-LAL) assay was performed per the manufacturer's instructions (ACC Inc., East Falmouth, MA) on a solution of 4×10^7 particles ml^{-1} . Quantification of endotoxin levels by chromo-LAL revealed that the particle endotoxin levels were below the detection limit of 0.050 endotoxin units ml^{-1} . The MPs were characterized by scanning electron microscopy and were determined to be spherical with an 890 nm diameter and smooth morphology. LPS loading did not affect the fluorescence signal from the MPs as determined by fluorescence microscopy imaging of solutions of known amounts of particles in square profile microcapillary tubes (VitroCom, Mountain Lakes, NJ). The fluorescence signals measured in-vitro and normalized to particle number for LPS-containing and non-LPS MPs were 0.543 ± 0.092 vs. 0.547 ± 0.101 , respectively (relative fluorescence intensity,

mean \pm standard deviation). No statistically significant difference (t-test, $p > 0.655$) was found between MPs with and without LPS in terms of the fluorescence signal.

Macrophage Cell Line

Macrophage murine RAW 264.7 cells were cultured in 35 mm tissue culture-treated polystyrene dishes (Corning). The macrophage medium consisted of 10% fetal bovine serum (Bio-Whittaker) and 1% penicillin–streptomycin (Hyclone) in DMEM/F12 (1:1) with L-glutamine (Cellgro, Herndon, VA). The cells were incubated at 37°C in a 5% CO₂ atmosphere and passaged every 3 days with a 1:3 split during passage.

Macrophages were fluorescently labeled by incubation with the fluorescent carbocyanine dye 1,1'-dioctadecyl-3,3,3',3'-tetramethylindodicarbocyanine, 4-chlorobenzenesulfonate salt (DiD) (Invitrogen) at a concentration of 5 $\mu\text{g ml}^{-1}$ in a serum-free solution of 2 mM dextrose in PBS for 30 min at 37°C. The cells were centrifuged for 5 min at 330g, washed with PBS, and then suspended in 200 μl of PBS. The cells were delivered systemically at a concentration of 8000 μl^{-1} and a total volume of 100 μl via the tail vein 2 h after surgery. Research suggests that a brief inflammatory response over a 2 h period could be expected after window chamber surgery due to exposure to the titanium window chamber structures [168], thus macrophages were injected 2 h after implantation of the windows. For the purposes of this study, the brief recovery time was expected to be enough to observe localization of the administered labeled macrophages to the MPs sufficiently above a response to factors associated with surgery given the strong induction of an innate immune response provoked by LPS.

Animal Model

All in vivo procedures were conducted under a protocol approved by the University of Florida Institutional Animal Care and Use Committee and conformed to the NIH

Guide for Care and Use of Laboratory Animals. Ten female athymic (nu/nu) nude mice, weighing 20-26 g (Charles River Laboratories, Raleigh, NC), were surgically implanted with titanium dorsal skinfold window chambers while under anesthesia consisting of ketamine (100 mg kg^{-1}) and xylazine (10 mg kg^{-1}) injected intraperitoneally. Nude mice were used in this study for the following reasons: we have extensive experience with window chambers in this model from research with xenograft tumors; in this proof-of-principle study the nude mouse was an acceptable stand-in for the genetically modified mice we may use in future experiments with adoptive transfer of various immune cells; and nude mice have previously been used in immune cell research for certain purposes when a T-cell-deficient host was desired, such as for the adoptive transfer of leukocytes [169]. In our study, the lack of T-cells in the nude mice was not critical since we were primarily interested in tracking the administered RAW 264.7 macrophages. During surgery one layer of dorsal skin was carefully and completely removed in a circular area of about 12 mm diameter and covered with a glass coverslip. Spectral and fluorescence imaging were performed for up to 6 days after administration of fluorescently labeled macrophages. After surgery animals were housed in an environmental chamber maintained at 33°C and 50% humidity with free access to food and water and standard 12 h light/dark cycles.

A total of 10 mice were placed in one of four different groups: control mice ($n = 3$), which received saline injections instead of MPs; LPS(-) mice ($n = 3$), which received MPs without LPS, LPS(+) mice ($n = 3$), which were administered MPs with LPS at a concentration of 400,000 particles in $20\mu\text{l}$; and LPS(++) mice ($n = 1$), which were administered MPs with LPS at a concentration of 2,000,000 particles in $20\mu\text{l}$. The $20\mu\text{l}$

total dose of MPs was injected in two 10 μ l volumes in two different locations in the window chamber.

Intravital Fluorescence and Spectral Imaging

A Zeiss microscope (Carl Zeiss, Incorporated, Thornwood, NY) was used as the imaging platform. A 100W tungsten halogen lamp was used for transillumination of the window chamber. Spectral image datasets were acquired with a monochrome scientific grade CCD camera thermoelectrically cooled to -20°C (DVC Company, Austin Texas) and fluorescence images were acquired with an ANDOR iXon electron multiplying CCD (EMCCD) camera thermoelectrically cooled to -50°C (ANDOR Technology, South Windsor, CT). A 2.5 \times objective (Carl Zeiss, Inc., Thornwood, NY) was utilized for imaging.

Spectral imaging of microvessel HbSat was performed as done previously [145, 165]. Briefly, customized LabView software (National Instruments, Austin, Texas) was used to automatically acquire spectral images. Spectral image data were collected using a liquid crystal tunable filter (CRI, Cambridge, MA) with a 400–720 nm pass band and 10 nm nominal bandwidth. Band-limited images were acquired from 500 to 575 nm at 5 nm intervals to create HbSat pseudocolor maps from pure oxy- and deoxyHb reference spectra as described previously [145]. Fluorescently labeled macrophages and PLGA MPs were imaged using the EMCCD camera with a FITC filter set (Chroma Technology Corp., Rockingham, VT; excitation: 480 nm, with 20 nm bandwidth; emission: 550 nm, with 30 nm bandwidth) and a Cy5 filter set (Chroma Technology Corp., Rockingham, VT; excitation: 640 nm, with 20 nm bandwidth; emission: 680 nm, with 30 nm bandwidth), respectively. Image processing and statistical analysis were performed using Matlab (The Mathworks, Incorporated, Natick, Massachusetts) and

SPSS software (SPSS for Windows; SPSS Inc., Chicago, Illinois, USA), respectively. Spectral and fluorescence imaging were performed up to 6 days after surgery.

Results

After administration of macrophages via tail vein injection, two different large regions of interest (ROIs) corresponding to the two regions where MPs were injected were chosen to investigate the interaction between MPs and localized macrophages, and adjacent microvessel HbSat during a posterior analysis phase. Macrophage localization to MPs was presumably due to a combination of macrophage accumulation and extravasation.

Hyperspectral and Fluorescence Imaging

Macrophage accumulation and HbSat changes over time for the different groups (control saline injected, LPS(-), LPS(+), and LPS(++)) are shown in Figs. 3.1–3.4. Images in the rows are transmitted light, microvessel HbSat, distribution of MPs and macrophage accumulation. Images were acquired at 0, 6, 12, 24, 48, 72 and 144 h after the injection of labeled macrophages for control, LPS(-), and LPS(+) mice, and at 0, 1, 2, 4, 6, 8, 12, and 24 h for LPS(++) mice. There were perturbations in tissue microvessel HbSat over time in all of the different groups. As shown in Figs. 3–1 and 3–2, the macrophage accumulation appears similar for both the control group, administered the saline carrier alone, and the LPS(-) group, with unloaded MPs, demonstrating a lack of appreciable inflammation response to the unloaded MPs. There is greater macrophage accumulation in the LPS(+) group as compared to the control group, demonstrating appreciable inflammation due to LPS release (Fig. 3–3). Note that variation in the signals of MPs in LPS(-) and LPS(+) groups was observed (Figs. 3–2 ~ 4). This may be due to several reasons. More active interaction of macrophages with

LPS could have caused wider dispersion of MPs in the LPS(+) and LPS(++) groups than in the LPS(-) group. Additionally, some FITC dye quenching may have occurred in acidic MPs and cell endosomes, but when dye was released into neutral pH tissue, the fluorescence increased [170]. It was observed that there was significantly larger and more rapid macrophage accumulation in the LPS(++) mice than in any of the other groups (Fig. 3–4). Additionally, there was a very large decrease in tissue microvessel HbSat in the LPS(++) mice that initiated in the vicinity of the MPs and spread out over time. Six hours after injection of macrophages, a significant amount of macrophages had accumulated in the window chamber, and there was extensive microvessel disruption and tissue necrosis. Tissue alterations leading to necrosis could be observed 1 h after injection of macrophages (arrows in Fig. 3-4).

Quantitative Analysis for Hemoglobin Saturation Map, Microparticles and Macrophages

The results of quantitative regional data analysis of Figs. 3-1~3-4 are shown in Figs. 3-5~3-7. At least 25 different locations on arterioles and venules near MP implantation sites for each mouse were chosen as ROIs to quantitatively analyze HbSat and macrophage signals. Note that macrophage fluorescence signals in the ROIs were due to total accumulated DiD-loaded macrophages in the ROIs, with no distinction between those in blood vessels and ones that extravasated. ROIs on arterioles and venules that encompassed the immediate vicinity of the microvessels for LPS(++) (25 ROIs), LPS(+) (26 ROIs per mouse), LPS(-) (28 ROIs per mouse) and saline control (30 ROIs per mouse) were analyzed for all of the imaging time points.

Numerical HbSat data and macrophage signals in the ROIs were plotted at various imaging time points as mean \pm standard deviation and are shown in Figs. 3-5 and 3-6,

respectively. The HbSat in arterioles and venules of the LPS(+) mice was relatively stable and lower than in the LPS(-) and control groups, whereas the macrophage signals were higher in the LPS(+) than in the LPS(-) and control groups. Statistical differences ($p < 0.05$) of HbSat data in LPS(+) from other groups were apparent between 24 and 12 h in Fig. 3-5. Similarly, the macrophage signals of the LPS(+) group at the same ROIs demonstrated statistical differences ($p < 0.05$) from 12 h (Fig. 3-6). In the LPS(++) mice an immediate and rapid decrease in vascular oxygenation and an increase in macrophage accumulation were observed. The fluorescence intensity representing the macrophage signal for the LPS(++) mice in Fig. 6 is the actual macrophage signal $\div 5.5$, so the signal could be superimposed for easy viewing with the other groups shown in the figure. Within each group there was no difference in the macrophage signal between ROIs on arterioles or venules.

Statistical Analysis for Accumulated Region of Interests Data

HbSat and macrophage signal measurements were averaged over all imaging time points, as shown in Fig. 3-7, and analysis of variance (ANOVA) followed by a Scheffe's post hoc test were used to assess the statistical significance of the differences between the groups. The HbSat and macrophage data from the LPS(+) and LPS(++) groups were found to be significantly different ($p < 0.05$) vs. the LPS(-) and control groups, and there was a significant difference between LPS(++) and LPS(+). No significant difference between control and LPS(-) was observed.

In summary, we tracked localization of a specific immune cell, systemically administered macrophages in our case, to inflammatory LPS-loaded biomaterial MPs as a model vaccine/adjuvant delivery system. Simultaneously we measured from endogenous signals of HbSat changes in the co-localized tissue microvessel

oxygenation due to the host innate immune response to the MPs. For our experimental groups we observed a general trend of greater and faster macrophage localization with stronger inflammatory stimuli in terms of the amount of LPS concentrated in an area. With increased macrophage localization to MPs, we observed a trend of decreased microvessel oxygenation. Microvessel disruption and tissue necrosis occurred in the extreme case.

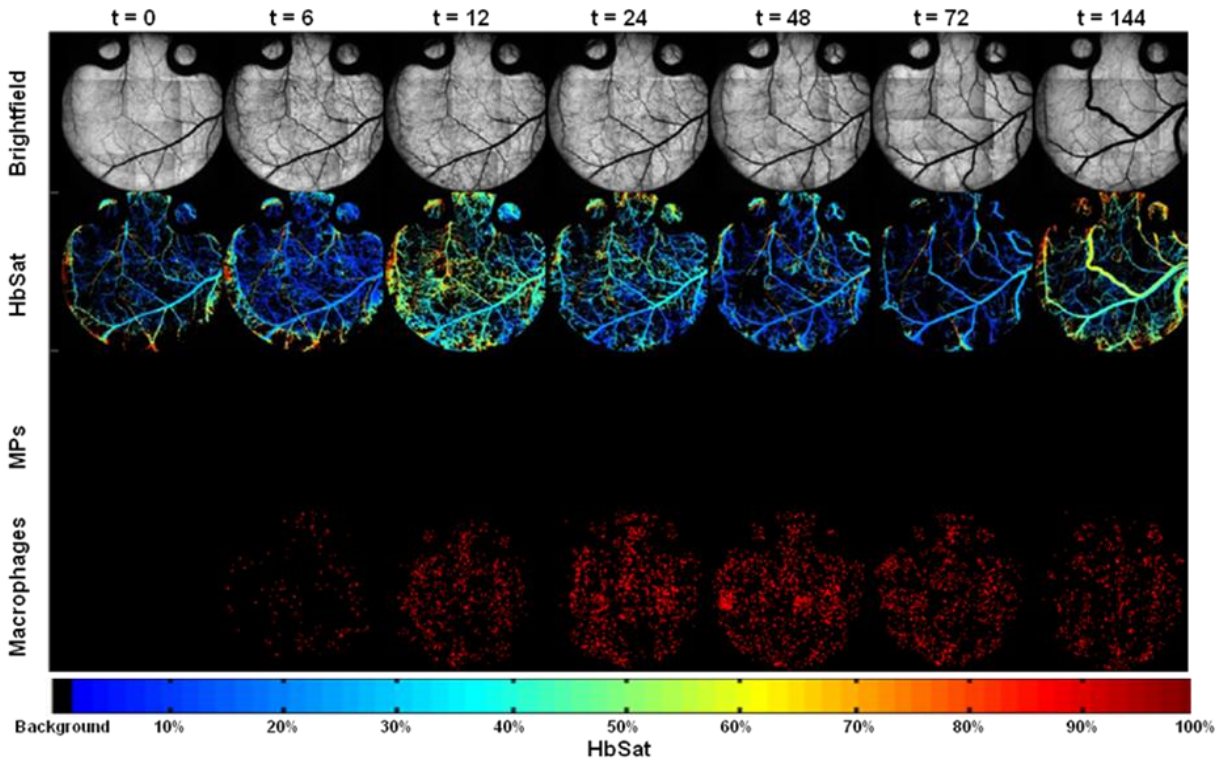


Figure 3-1. Hyperspectral and fluorescence Hb images for a control mouse with saline (carrier) injection without microparticles. Rows from top to bottom – Transmitted light (brightfield), microvessel HbSat (HbSat), microparticles (MP), and macrophage distributions (Macrophages) acquired at 0, 6, 12, 24, 48, 72, and 144 hours after the injection of labeled macrophages for a control mouse with saline (carrier) injection without microparticles. The window chamber area has a 12mm circular diameter. The color bar shown at bottom of the figure represents the oxygenation level in HbSat maps.

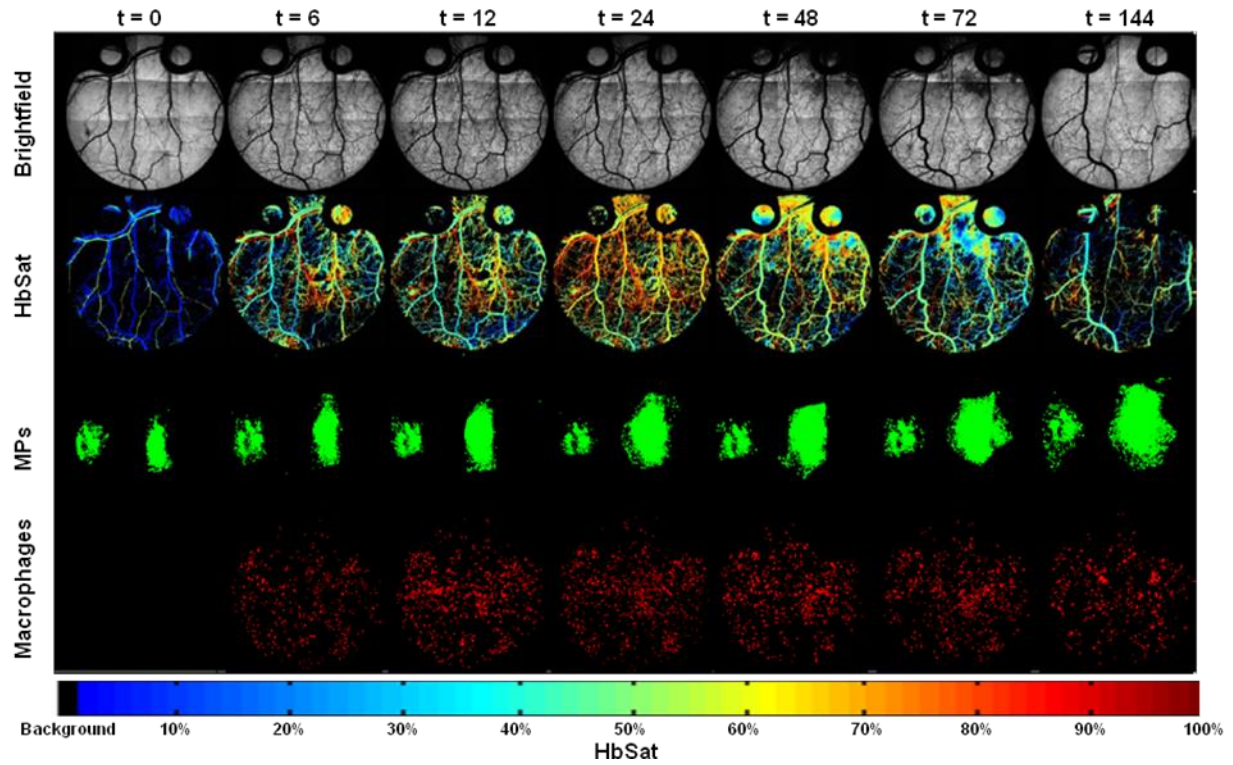


Figure 3-2. Hyperspectral and fluorescence images for a LPS(-) mouse with microparticles lacking LPS. Rows from top to bottom – Transmitted light (brightfield), microvessel HbSat (HbSat), microparticles (MP), and macrophage distributions (Macrophages) acquired at 0, 6, 12, 24, 48, 72, and 144 hours after the injection of labeled macrophages for a LPS(-) mouse with microparticles lacking LPS. The window chamber area has a 12mm circular diameter. The color bar shown at bottom of the figure represents the oxygenation level in HbSat maps.

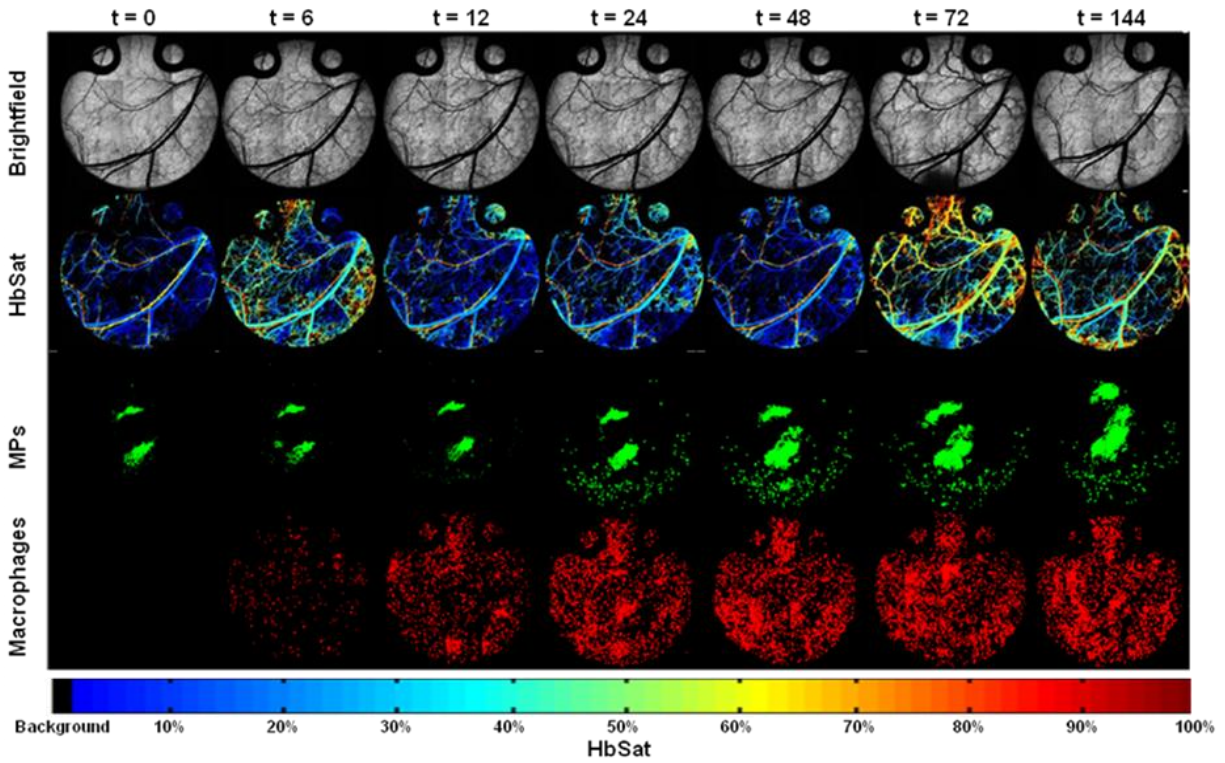


Figure 3-3. Hyperspectral and fluorescence images for a LPS(+) mouse with LPS encapsulated microparticles (400,000 in 20 μ L). Rows from top to bottom – Transmitted light (brightfield), microvessel HbSat (HbSat), microparticles (MP), and macrophage distributions (Macrophages) acquired at 0, 6, 12, 24, 48, 72, and 144 hours after the injection of labeled macrophages for a LPS(+) mouse with LPS encapsulated microparticles (400,000 in 20 μ L). The window chamber area has a 12mm circular diameter. The color bar shown at bottom of the figure represents the oxygenation level in HbSat maps.

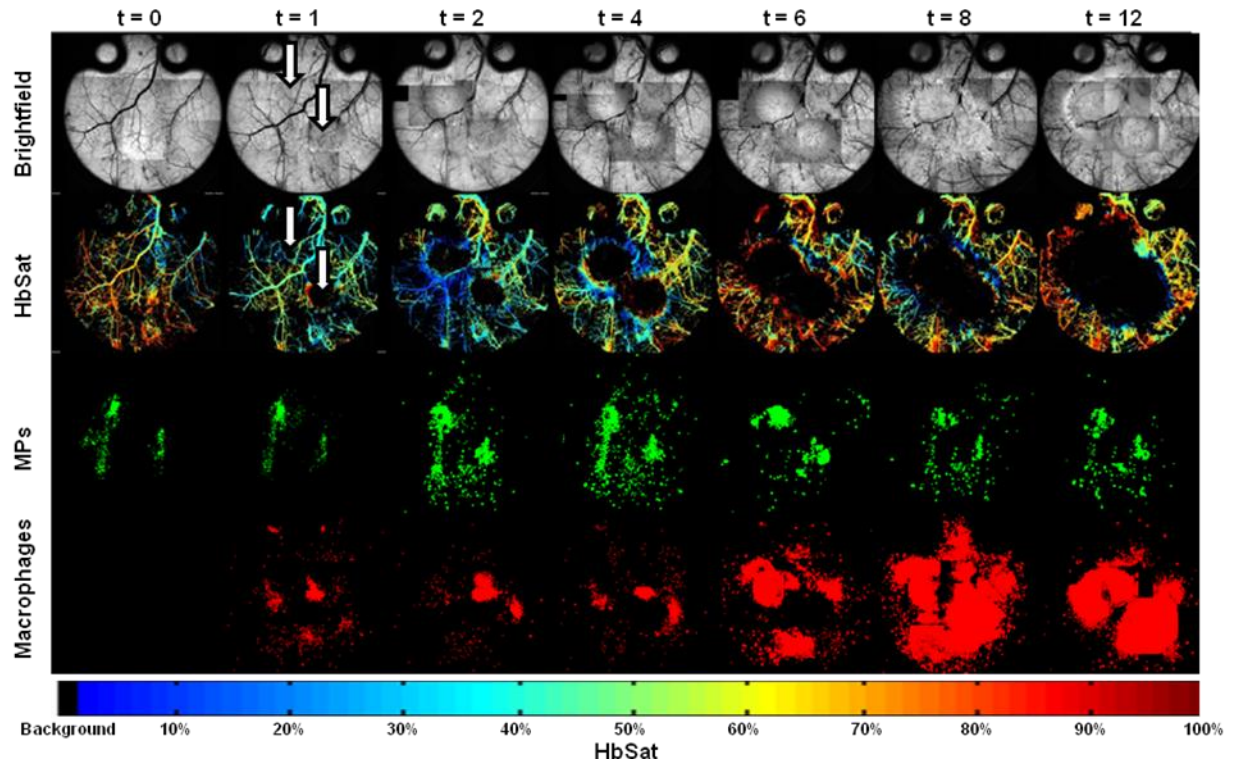


Figure 3-4. Hyperspectral and fluorescence images for LPS(++) mouse with LPS encapsulated microparticles (2,000,000 in 20 μ L). Rows from top to bottom – Transmitted light (brightfield), microvessel HbSat (HbSat), microparticles (MP), and macrophage distributions (Macrophages) acquired at 0, 6, 12, 24, 48, 72, and 144 hours after the injection of labeled macrophages for LPS(++) mouse with LPS encapsulated microparticles (2,000,000 in 20 μ L). The window chamber area has a 12mm circular diameter. The color bar shown at bottom of the figure represents the oxygenation level in HbSat maps. White arrowheads indicate the regions where tissue necrosis occurs.

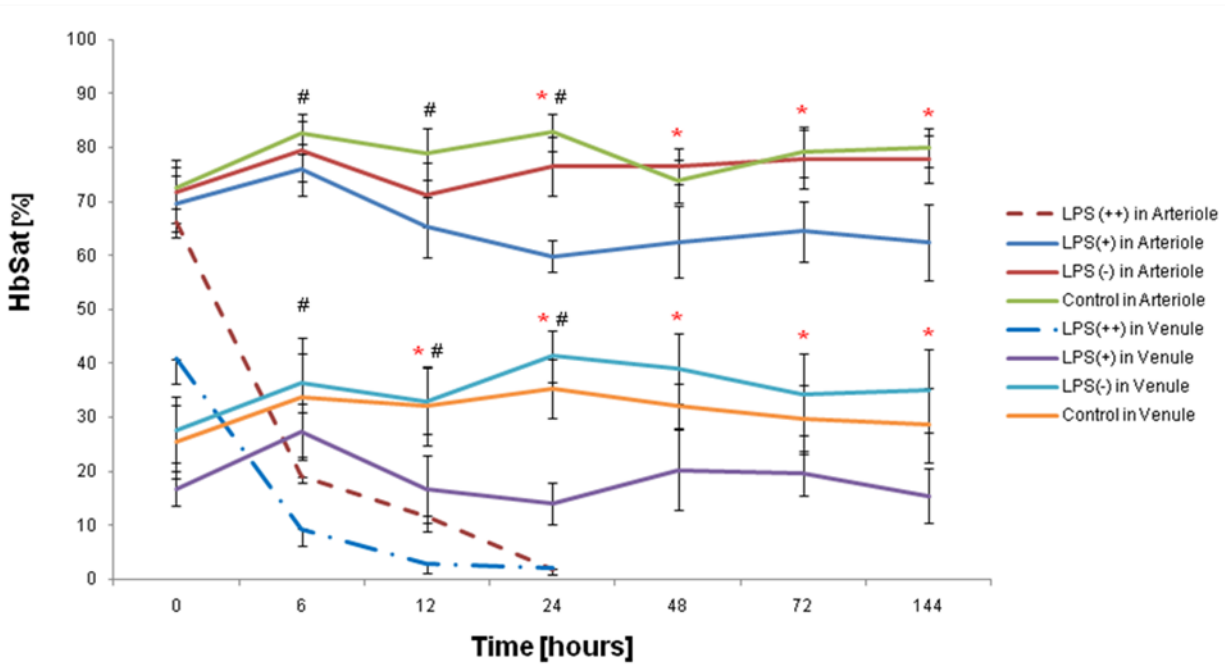


Figure 3-5. Numerical HbSat data for each group of ROIs at various time points. The ROIs are selected on arterioles and venules separately. Solid lines represent HbSat in arterioles and venules of control, LPS(-), and LPS(+) (mean \pm S.D.) while dotted lines represent HbSat in the arterioles and venules of LPS(++)(mean \pm S.D.). * = LPS(+) HbSat in the arterioles and venules are statistically different ($p < 0.05$) from control and LPS(-) after 24 and 12 hours post-injection of macrophages, respectively. # = LPS(++ HbSat from the arterioles and venules are statistically different ($p < 0.05$) from LPS(+) group after 6 hours post-injection of macrophages.

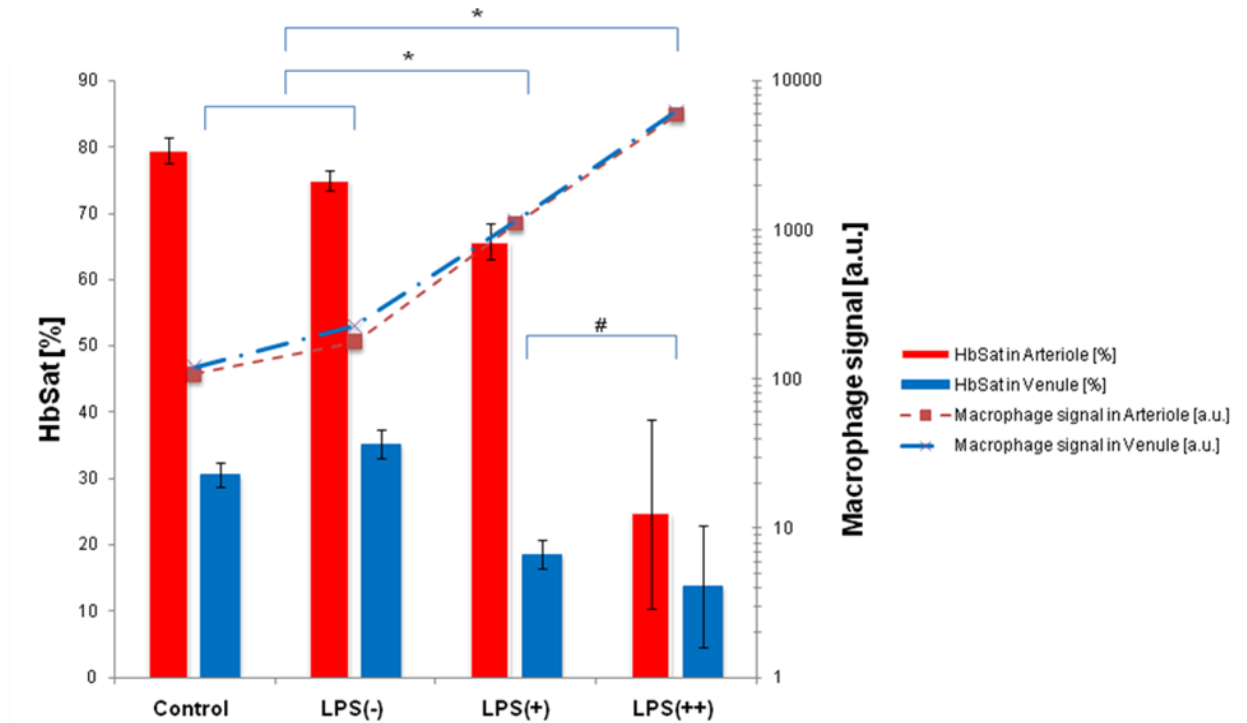


Figure 3-7. The accumulated ROI data overall time points are analyzed using ANOVA and Scheffe's post-hoc test. The bars represent HbSat in arterioles and venules of each group (mean \pm S.D.) while the dotted lines represent the macrophage fluorescence signals at the arteriole and venule ROIs of each group (mean). * = LPS(+) and LPS(++ groups data are significantly different from the control group ($p < 0.05$). # = LPS(++ group data are significantly different from LPS(+) ($p < 0.05$).

Discussion

Antigens and therapeutic drugs encapsulated in MP delivery systems have been investigated clinically [150]. Polymer-based antigen delivery systems for vaccines have the potential to release antigens in a continuous manner such that a single dose of a biodegradable polymer vaccine can be substituted for the repeated doses required in some conventional vaccinations [150, 153]. PLGA, a US Food and Drug Administration approved biomaterial, has been the most extensively investigated of the polymer-based materials for controlled delivery of antigens and drugs [150]. Numerous undesired effects, including impaired blood vessel function, tissue regeneration failure and organ failure, have occurred by incompatible tissue response to biomaterials alone [171, 172]. The combination of biomaterials, antigens and adjuvants in a biomaterial MP-based vaccine formulation represents a complex system that can result in complex responses from various immune cells with undesired tissue effects. The adjuvant formulation is particularly important in order to optimally shape the adaptive immune response without inducing excessive inflammation [173]. Therefore, the adequate evaluation of the biocompatibility and biodegradability of new biomaterial / drug combinations for MP-based vaccines requires in vivo experiments to fully appreciate the immune cell and tissue responses.

Typically, a series of inflammatory responses occur immediately after implantation of biomaterials [145, 159, 165]. It is desirable to tune the inflammatory response to MP-based vaccines in order to optimize the vaccination process. For example, macrophages actively react and respond to almost all the various biomaterials within minutes to hours after implantation because the inflammatory response is immediately initiated by injury to vascularized connective tissue in the implantation procedure [174].

Macrophages mediate several inflammatory responses in host tissues by infiltrating biomaterial-based implants, including those made of metal, ceramics, cements, polymers and protein constructs [167, 172]. Because of the long lifetime of macrophages (from days to months) [172] and the key role they play in innate and adaptive immune responses and chronic inflammation [175, 176], it is particularly critical to control the response of macrophages to MP-based vaccines. It would be desirable for MP-based vaccines to stimulate the antigen-presenting behavior of macrophages while inhibiting tissue-damaging functions.

In vivo imaging may be a useful tool to investigate the responses of various immune cells to MP-based vaccine formulations and the subsequent tissue effects. Intravital microscopy techniques have been utilized where continuous physiological monitoring and repetitive measurements on the same animal are needed [127, 163, 164]. Recently, dorsal skin window chambers have been used with mice to investigate host tissue response to implantable PLGA scaffolds over various imaging time points [156]. Neovascularization and inflammatory response to PLGA and the correlation between macrophage activities and blood vessel permeability was observed in these model systems [156]. In the present study, spectral and fluorescence intravital microscopy imaging was used with mouse dorsal skin window chambers to simultaneously measure localization of systemically administered macrophages and co-localized tissue microvessel oxygenation in response to implanted PLGA MPs with and without encapsulated LPS. We observed an increase in macrophage localization to LPS-loaded MPs compared to unloaded MPs and control saline injections, which is in agreement with other results from the literature [156, 167, 177, 178]. There was greater

and more rapid macrophage localization to a higher density of LPS-loaded MPs. Additionally we observed a concomitant decrease in local microvessel oxygenation in both arterioles and venules with increased numbers of macrophages. With a sufficiently large number of macrophages we observed an extreme decrease in microvessel oxygenation that was accompanied by tissue necrosis.

The decrease in microvascular oxygenation that occurred with increased amounts of accumulated macrophages was expected and was probably due to several different factors. For example, it is known that oxygen is consumed by activated inflammatory cells at a high rate [179] and phagocytosis of particulates by macrophages induces a burst of ROS production [162]. LPS greatly increases RAW 264.7 macrophage phagocytosis [177], and phagocytosis of PLGA MPs by these cells results in an oxidative burst [177]. Nitric oxide (NO) production in endothelial cells and macrophages stimulated by activated macrophages may also have decreased microvessel oxygenation. LPS activated macrophages produce NO with respect to microbicidal functions in a dosedependent manner [153, 177, 180-182]. NO can bind tightly to Hb such that the NO-bound Hb does not easily dissociate to carry and transport oxygen [153, 177]. Also, high concentrations of NO or its derivatives can interact with mitochondrial or other respiratory chain complexes, leading to tissue necrosis [183].

Rucker et al. [156] used mouse dorsal skin window chambers to observe macrophage response to PLGA scaffold constructs placed in the window chamber. The authors observed a moderate increase in numbers of rolling and accumulated leukocytes in response to PLGA scaffolds compared to controls without scaffolds. In our study, we saw no significant difference between saline control and empty PLGA MPs in

terms of localization of macrophages. This discrepancy may be due to several factors. Rucker et al. used BALB/c mice, while athymic nude mice were used in this study. Also, in Rucker et al. employed a comparatively large scaffold (3 mm×3 mm×1 mm), while in this study a relatively small amount of material was used. Finally, in Rucker et al. the PLGA scaffolds were placed on the tissue in the window chamber, while in our study the MPs and control saline doses were injected intradermally. The act of injecting the saline and empty control MPs may have induced similar mild inflammatory reactions in our study, unlike the control case in Rucker et al., in which no tissue damage occurred in the control case.

Spectral imaging intravital microscopy of microvessel Hb captured simultaneously with immune cell localization to biomaterial MPs may be useful in laboratory investigations of MP-based vaccine development. For example, Rucker et al. [156] used caspase-3 staining to search for evidence of apoptotic cells after implantation of biomaterial scaffolds in mouse window chambers, but these measurements required animal sacrifice for tissue histology sections. In our study, using serial observations in vivo, we found a decrease in HbSat around LPS(+) particles and an extreme decrease around LPS(++) MPs accompanied by apparent tissue necrosis. The drop in HbSat was measured prior to tissue changes indicative of necrosis that could be observed with the naked eye. Measurements of microvessel HbSat around an MP vaccine injection site may also be useful for clinical investigations as measurements of tissue HbSat may potentially serve as a biomarker for a harmful inflammatory reaction. For example, Stamatias and Kollias [184] used clinical spectral imaging of skin to measure bulk tissue response to inflammatory stimuli such as rhus dermatitis, which can occur in reaction to

poison ivy exposure. The authors found a moderate increase in deoxyHb around skin inflammation sites. Using spectroscopy of tissue Hb, Liu et al. [185] have shown that there is an increase in tissue blood supply in periodontal inflammation, though the increase is insufficient for the metabolic demand of the inflammation process and thus tissue oxygenation is lower than normal.

CHAPTER 4 PREFERENTIAL ACCUMULATION OF SICKLE RED BLOOD CELL IN TUMORIC ENVIRONMENT

The ideal drug carrier has to possess two important features to overcome systemic toxicity causing significant morbidity from conventional chemotherapy to treat distant metastases: tumor-selective accumulation and controlled release of drug contents from carriers. Many drug carriers including nanoparticles [6], polymer micelles [30], polymeric conjugate [31], lipid microemulsion [32], liposomes [33], and resealed erythrocytes [34] have been developed as drug carriers. Among those drug carriers, resealed RBCs loaded with therapeutic agents has been exploited extensively for both temporally and spatially controlled chemotherapeutic carriers. Ihler et al. first used the erythrocyte as the carrier to deliver enzyme in human body to heal certain diseases successfully [47] and then various drugs and other bioactive agents have been tried owing to their remarkable degree of biocompatibility, biodegradability, prolonged life-time in circulation and a series of other potential advantages as described in Chapter 1.

Interestingly, tumor-preferential accumulation by SSRBCs due to a combination of adhesion receptor over-expression and mechanical changes induced in the sickle cells under the deoxygenated tumor environment were shown previously by several case reports. Rapid tumor-specific accumulation of epinephrine induced SSRBC was demonstrated in a mouse model [86], intravenously administered SSRBCs from human SCD patients shown to preferentially accumulate in a rat brain tumor model [90], and extensive intravascular sickling of erythrocytes was observed in sickle trait patient with stage IIIB squamous cell carcinoma of the cervix by clinical case report [91]. Theoretically, tumor regions expressing hypoxic stress are suited to change morphological properties in SSRBCs. The environments of some tumor regions are

characterized in terms of low pH, low oxygen tension, relatively low blood flow due to disorganized vasculature and higher blood viscosity, permeability and interstitial pressure [186]. Therefore, HbS polymerization can be initiated by these unique characteristics under tumoric conditions and changes the flexibility of red blood cells. Other characteristics of tumor vasculature such as tortuous, chaotic vasculature or abnormal vessel lining also enhance sickling or promote SSRBC aggregation[90].

Moreover, matured SSRBCs express a number of adhesion receptors interacting to endothelial cells such as B-CAM/Lu, LW (ICAM-4), and CD47 [85]. Zennadi et al. and Kaul et al. showed that overexpressed LW on SSRBCs is a major receptor for endothelial $\alpha_v\beta_3$ integrins contributing to the adhesion in animal models [86-88], and $\alpha_v\beta_3$ integrin is one of the overexpressed counter-receptors in tumor microvascular endothelial cells[89]. Accordingly, SSRBCs may have a promising combination of molecularly and mechanically accumulated factors as a new tumor-targeting carrier with preferential accumulation in tumor sites.

Based on this evidence of SSRBCs' sickling causing vaso-occlusion under hypoxic condition described above, this study focused on the accumulation of several types of SSRBCs in tumors using intravital microscopy imaging and video recording of sickle cell accumulation to and obstruction of microvessels in tumors grown in dorsal skin-fold window chambers. This intravital microscopic imaging method was employed previously for the quantitative analysis of fluorescently labeled macrophage localization to immunogenic particles [187].

In this experiment, various blood samples were prepared to compare with each other and summarized in Table 4-1. Briefly, they were from human SSRBCs with /

without hydroxyurea treatment, wildtype mouse (C57BL/6), and two types of transgenic SCD mouse models such as Berkeley SCD mouse one of the most commonly used SCD mouse model [188, 189] and knock in SCD mouse (*Hba^{tm1Paz}Hbb^{tm1Tow} Tg(HBA-HBBs)41Paz/J*) recently developed and considered as the better SCD mouse model than Berkeley mouse [190, 191].

Fluorescently labeled blood cells were prepared for intravital microscopic observation and administered into 4T1 tumor bearing immunodeficient mouse models. Involved tissues from tumor, spleen and kidney were harvested to perform histological test to compare the entrapment rate of blood cells. Tissue specimens harvested for histology were snap frozen method to preserve the sickle cell fluorescence signal. In this Chapter, the tumor-selective accumulation of SSRBCs from human SCD patients and SCD murine models to the endothelium and vaso-occlusion in the tumoric environment were explored. Controlled release of substance from SSRBCs as the second required feature for drug carriers is examined in Chapter 5 [99-101, 192].

Table 4-1. Categorized groups for preferential accumulation of SSRBCs to tumoric microvasculature experiment.

Group	Species	Hydroxyurea treatment	n
C57	Wildtype mouse: C57BL/6	N	6
Hydroxyurea-on	Human SCD patient	Y	5
Hydroxyurea-off	Human SCD patient	N	3
Knock-in	Knock-in SCD mouse: <i>Hba^{tm1Paz}Hbb^{tm1Tow} Tg(HBA-HBBs)41Paz/J</i>	N	7
Berkeley	Berkeley SCD mouse:	N	7

Materials and Methods

Tumor Cells

4T1 mouse mammary adenocarcinoma cells were generously provided by Dr. Mark W. Dewhirst (Duke University Medical Center, Durham, NC). The cells were

cultured as a monolayer in DMEM (Cellgro, Inc., 1X, 4.5 g/l glucose, L-glutamine and sodium pyruvate) with 10% fetal bovine serum (Biowhittaker, Inc.), 1% L-glutamine (Clonogen, Inc.) and 1% penicillin streptomycin (Clonogen, Inc.). Single cell suspensions were prepared in DMEM without serum at room temperature and stored at 4°C until its subcutaneous injection in the window chamber on dorsal skin of mouse models.

Animal Model

All in-vivo experiments were carried out under a protocol approved by the University of Florida Institutional Animal Care and Use Committee (IACUC) and conformed to the NIH Guide for Care and Use of Laboratory Animals. Female athymic (nu/nu) nude and wild type (C-57) mice weighing between 20 and 26 g were obtained from Charles River Laboratories (Raleigh, NC) for this study.

A total of 28 4T1 tumor bearing mouse models with window chamber were placed in this experiment; Control group (n=6) administered with the labeled normal RBCs from C57 donor mice, Berkeley group (n=7) administered the labeled SSRBCs from Berkeley donor mice, Knock-in group (n=7) administered the labeled SSRBCs from Knock-in donor mice, Hydroxyurea-on group (n=5) administered the labeled SSRBCs from hydroxyurea medicated human SCD patients, Hydroxyurea-off group(n=3) administered the labeled SSRBCs from human SCD patients untreated with hydroxyurea.

Window Chamber Installation

Double sided titanium skinfold window chambers were surgically implanted into dorsal skin flap under anesthesia attained by intraperitoneal injection of ketamine (100mg/kg) and xylazine (10mg/kg). The epidermal and dermal layers of dorsal skin were carefully but completely removed in a circular area of about 12 mm diameter. A

single cell suspension of 10×10^3 tumor cells in 10ul was injected subcutaneously and a glass coverslip was placed on the window chamber to cover exposed tissue. After surgery, animals were housed in an environmental chamber maintained at 33 °C and 50% humidity with free access to food and water and standard 12 hrs light/dark cycles.

Preparation of Blood Cells

Fresh human SSRBCs from SCD patients were prepared by Dr. Richard Lottenberg (M.D. Professor, Department of Medicine, Division of Hematology/Oncology, University of Florida) and murine SSRBCs from the transgenic SCD mouse models were collected by Dr. Angela E. Rivers (M.D, Ph.D. Assistant Professor, Department of Pediatrics, Division of Hematology/Oncology, University of Florida). The Institutional Review Board (IRB) of University of Florida approved of obtaining patient blood sample for this study. Informed written consents were obtained from all patients in accordance with the Declaration of Helsinki.

Some of human SCD patients were medicated by hydroxyurea and all blood samples are categorized in Table 4-1. Murine SSRBCs were obtained from Knock-in and Berkeley SCD mouse models by retro-orbital bleeding using a heparinized glass pipette and normal RBCs were obtained by cardiac puncture from a donor C57BL/6 wildtype mouse. All donor mice were anesthetized by 1%-2% isoflurane in air and blood samples were collected about 1.5ml from each donor mouse. The prepared blood samples were stored in ethylenediaminetetraacetic acid (EDTA) tubes at 4°C until use.

Obtained cells from donor patients and mice were fluorescently labeled with a 1mM stock solution of Carbocyanine dye 1,1'-dioctadecyl-3,3,3',3'-tetramethylindodicarbocyanine, 4-chlorobenzenesulfonate salt (DiD solid, Invitrogen, D-7757) in ethanol using a modified procedure by Unthank et al [193]. Briefly, the RBCs

were washed via centrifugation at 4°C and resuspend in Dulbecco's Phosphate Buffered Saline (DPBS with 1mM of Ca²⁺ and 0.5mM of Mg²⁺ without phenol red, SH30264.01, HyClone) until its supernatant is clear. Isolated 200ul of cells were incubated with 200ul of DiD stock solution in 10ml of sterile DPBS at room temperature for 30min. To protect the sample from ambient light, the all tubes were covered by aluminum foil during all procedures. Unbound DiD dye was carefully removed by repeated washing steps.

DiD labeled murine RBCs in 200 µl of DPBS (hematocrit [Hct] 0.5 [50%]) were administered in mouse anesthetized by 1%-2% isoflurane in air by tail vein when the tumors reached about 6mm in a diameter. In the present study, the quantity of human and murine RBCs did not exceed 12% of the total circulating RBCs assuming that the mouse blood volume is 1.7ml, thereby minimizing any possible rheologic effects attributable to increased Hct [194]. Fluorescently labeled RBCs (100 µl) were saved at 4°C to evaluate for the efficiency of the labeling method by flow cytometry test.

Intravital Spectral and Fluorescence Imaging

Mice anesthetized by 1%-2% isoflurane in air were placed on the stage of an Axio microscope (Carl Zeiss, Inc., Thornwood, NY) and body temperature was maintained at 37°C by a heating pad. The spectral imaging system, image acquisition, and image processing techniques to create Hb saturation map and intravital fluorescence images for localized RBCs in microvasculature, normal and tumor tissues were explained in Chapter 2 and in previous studies [145, 187].

Briefly, microscopy was employed as a basic platform for the imaging system. A 100W tungsten halogen lamp and 100W mercury lamp was used for transillumination and epi-illumination of the window chamber, respectively. Spectral image datasets were

acquired with a monochrome scientific grade CCD camera thermoelectrically cooled to -20°C using 2.5× Fluars objective for up to 7 days prior to treated RBCs injection. Fluorescence imaging and video recording for quantitative analysis of blood cell accumulation were acquired with an Andor iXon EMCCD camera thermoelectrically cooled to -50°C using 5× Fluars and a 20× LD-Plan-NeoFluar objectives, respectively. Customized LabView software was used to automatically acquire spectral images. Spectral image data were collected using a LCTF with a 400–720 nm pass band and 10 nm nominal bandwidth. Band-limited images were acquired from 500 to 575 nm at 5 nm intervals to create Hb saturation pseudocolor maps from pure oxy- and deoxy-Hb reference spectra as described previously [145]. DiD (excitation: 644nm, emission: 665nm) marked blood cells were depicted and recorded using the EMCCD camera with a Cy5 filter set (Chroma Technology Corp., Rockingham, Vermont, excitation 640nm with 20nm bandwidth, emission 680nm with 30nm bandwidth) in line with the illumination source of a Zeiss FluoArc mercury lamp.

For fluorescence imaging with 5× Fluars objective, at least 6 regions of interest (ROIs) on postcapillary venules with up to 25µm diameter per mouse model were chosen where large number of immobile RBCs were observed in good focus and analyzed quantitatively. Since fast-moving RBCs in blood stream were appeared as gray lines with increased exposure time (up to 150ms), motionless blood cells were easily observed due to their brighter fluorescence signal. They were considered as accumulated cells to vessel wall and quantified by the image processing techniques using Matlab software (The Mathworks, Incorporated, Natick, Massachusetts) as done previously [187].

Additionally, fluorescently labeled blood cells were recorded via streaming video analysis using 20x LD-PlanNeoFluar objective (Carl Zeiss, Inc., Thornwood, NY) for 5min of streaming video with 1500 frames (exposure time of 200ms) were saved at 0, 30, 60, 90, 180, 360 and 720min after administration of labeled blood cells. All data were acquired in kinetic mode with 2x2 binning with a shift speed of 0.564 μ s. Labeled SSRBCs that appeared to be immobile over 1 min in streaming video were considered as accumulated cells to vessel wall and counted manually. The number of immobile RBCs was divided by vascular area for numerical analysis.

Statistical analysis was performed SPSS software (SPSS for Windows; SPSS Inc., Chicago, Illinois, USA) and analysis of variance (ANOVA) followed by a Bonferroni's post hoc test were used to assess the statistical significance of the differences between the groups.

Histology

Particular organs such as liver, spleen and tumor tissue from mice were harvested immediately after the last imaging acquisition at 12 hrs after RBCs injection under dissecting scope. These specimens were selected for examination regarding phagocytosis or accumulation rate of SSRBC by reticuloendothelial system (RES) macrophages in the spleen and liver. In addition, the microvascular occlusions observed in human SCD consistently affected the lungs, liver, kidneys, bone marrow, and spleen of the transgenic SCD mice [195].

The harvested tissues were fixed with 10% formalin, dehydrated with 15%~30% sucrose solution, embedded in optimal cutting temperature (OCT) solution (Tissue-Tec OCT, Fisher Scientific, Pittsburgh, PA) in plastic cryomolds and snap-frozen above pre-cooled methylbutane with dry ice at about -55°C. Specimens were sectioned by

microtome (Microm, HM550 microtome / cryostat, Microm International, Walldorf, Germany) at 20 μ m from standardized locations in each tissue at -18°C and each section was placed on Superfrost[®] Plus slide (Fisher Scientific, Pittsburgh, PA). The slides were merely air dried at room temperature overnight, then one slide was examined under fluorescence microscopy and consecutive slide was stained with hematoxylin and eosin (H&E). Five random, but same fields for two consecutive slides, were selected each tissue sample, then fluorescence and H&E stained images were acquired at a 20 \times magnification. Fluorescence intensities from labeled RBCs were quantified to compare accumulation ratio using Matlab software.

Results

Monitoring Hb Saturation Map

Bright field and HbSat maps were periodically observed after initiation of single cell suspension of 4T1 in dorsal window chamber to monitor the enhanced vascular development to deliver the excessive oxygen to growing tumor mass. Tumor size, microvascular structure and HbSat changes were monitored on 1st, 3rd, 5th and 7th day after 4T1 cell initiation (Fig.4-1) then labeled RBCs were administered when tumor size reached about 6 mm in a diameter with supplying vascular networks.

In-vivo Numerical Analysis of Accumulated Sickle Red Blood Cells using a Single Fluorescent Microscopic Image

After administration of fluorescently labeled RBCs and SSRBCs, at least 6 locations including enough number of venules within 25 μ m in diameter near tumor and normal sites in window chamber for each mouse were chosen as ROIs to quantitatively analyze fluorescence signals from preferentially accumulated SSRBCs to endothelium. Fluorescence and bright field Images were acquired after 0min, 30min, 60min, 90min,

3hrs, 6hrs, and 12hrs post-injection of labeled cells and compared with each group. For example, accumulated SSRBCs from Knock-in group in fluorescence images were segmented and overlaid to the bright field images of normal and tumor sites (Fig. 4-2). Greater number of the accumulated SSRBCs to microvasculature in tumor sites were determined as compared with in the normal sites. An accumulation of SSRBCs in hypoxic tumor sites was anticipated showing the enhanced accumulation to endothelial cells due to its polymerization of HbS in SSRBCs under deoxygenated environment and overexpressed adhesion receptors interacting with endothelial cells more than normal tissue sites. These results were consistent with research by others [90, 196].

The numerical analysis for all groups at all of the imaging time points were shown in Fig. 4-3. As shown in Figure 4-3 (A and B), Hydroxyurea-off group showed more dynamic and active accumulation at both tumor and normal sites than all the other groups. On the other hand, Hydroxyurea-on group demonstrated relatively stable accumulated rates as compared with the Hydroxyurea-off group and it showed much less accumulation in tumor sites as compared with murine models. In addition, its accumulation to blood vessels was similar both of normal and tumor sites. This was consistent with current clinical evidence that the efficacy of hydroxyurea, the only approved treatment of SCD, contributes to increased fetal Hb, decreased sludging and vaso-occlusion, decreased ischemia and necrosis, and decreased membrane damage [197]. There was a relatively higher accumulation rate in the Hydroxyurea-on group than murine blood groups in normal sites and this could possibly be explained by the larger volume of human's erythrocyte as compared with normal mouse[198].

Among murine blood sample groups, SSRBC signals of Knock-in and Berkeley groups in normal sites showed slightly lower intensity than the control group, whereas much higher SSRBC signal of Knock-in and Berkeley groups were seen in tumor site ROIs compared to the control group. Relative fluorescence intensities were calculated as shown in Fig. 4-3 (C). Averaged values of fluorescence signal on ROIs in tumor sites divided by ones in normal sites after 12 hrs post-administration of SSRBCs / RBCs was calculated and considered as relative fluorescence intensity. Statistical significance of the differences between the groups were calculated using ANOVA followed by a Bonferroni post hoc test and a p value below 0.05 was considered significantly different. Relative fluorescence intensity of Knock-in group and Berkeley group were significantly different not only from murine control group but also from human sample groups ($p < 0.05$). The highest relative fluorescence intensity from Knock-in group indicates that it had more enhanced accumulation rates to endothelium in tumor sites while much less in normal sites. In addition, Knock-in SCD mouse model has been considered as better SCD mouse model due to the therapeutic gene replacement upon homologous recombination regarding SCD research [191].

In-vivo Numerical Analysis of Accumulated Sickle Red Blood Cells using Fluorescence Video Recording

Fig. 4-4 shows supplementary microscopic observation of SSRBCs flux and accumulation by video recording for 5mins using 20x LD-Plan-NeoFluar objectives. It was conducted and analyzed at all of the same imaging time points, but human sample groups including Hydroxyurea-on and off were not included in this analysis due to its limited supply. Fig. 4-4 (A) show the bright field images of the interested microvasculature using 20x magnified objective and a single fluorescence image from

video recordings of localized SSRBCs in the same area at 12 hrs after post cells injection. Scale bar represents 50 μ m. Bar graph in Fig. 4-4 (B) shows relative fluorescence intensity for murine groups at all of the imaging time points and delivered similar results as in Fig. 4-3. The immobile SSRBCs over 1 min in streaming video were considered as accumulated cells to vessel wall and counted manually. It was divided by the number counted same way in normal sites to calculate the relative fluorescence intensities. Final relative fluorescence intensities were compared by both imaging methods with different magnification in Fig. 4-4 (C) and two different evaluation method showed similar patterns. Knock-in group had the most enhanced accumulation rate compared with the other murine models and it was significantly different from C57 and Berkeley groups.

Histological Analysis of Accumulated Sickle Red Blood Cells in Liver, Spleen and Tumor Tissues

The pathophysiologies in human SCD cause avascular necrosis, abnormal blood cell-endothelium interactions, inflammation, infarction and end organ failures [78-81]. Specifically, the microvascular occlusions observed in human SCD consistently affected the lung and liver disorders, kidney failure, bone marrow, and splenic infarction of the transgenic SCD mice [195]. In this experiment, typically damaged organs in human SCD patients such as liver and spleen were selected. In addition, tumor tissues were prepared by same way. They were stained by H&E method and a population of SSRBCs was monitored in each specimen using fluorescence imaging. Segmented fluorescence signals in green from RBCs and SSRBCs were superimposed the H&E stained images (Fig. 4-5 (A)). Numerically analysis of the cell population was performed and displayed in the bar graphs in Fig. 4-5 (B). To calculate the relative fluorescence

signals, the number of SSRBCs observed in a specific site was divided by the number of RBCs observed in the same area because the C57 group was considered as a reference group. Interestingly, the relative higher fluorescence intensity was detected in Knock-in group compared with Berkeley group and they were significantly different from each other ($p < 0.05$).

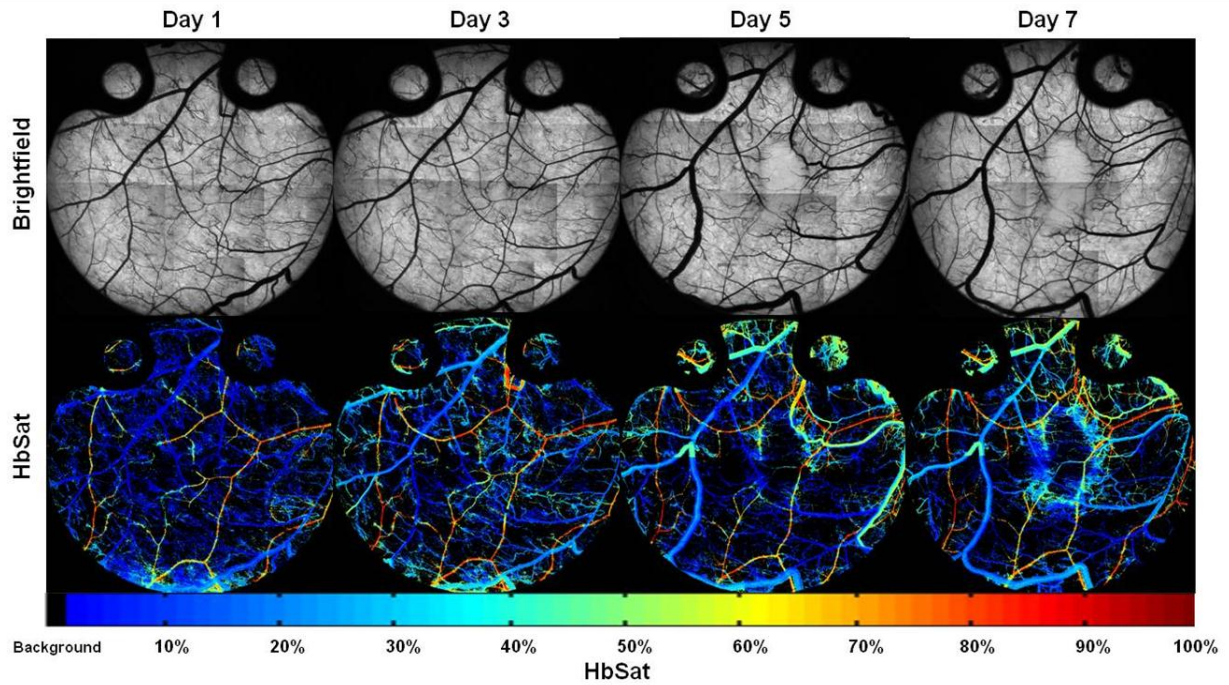


Figure 4-1. Hyperspectral images of dorsal skinfold window chamber. Transmitted light (brightfield) and Hb saturation (HbSat) images of dorsal skin fold window chamber were acquired on 1, 3, 5, and 7 days after initiation of 4T1 cells. The circular window chamber area has a 12mm diameter. The color bar shown at the bottom of the figure represents the oxygenation level in the HbSat maps.

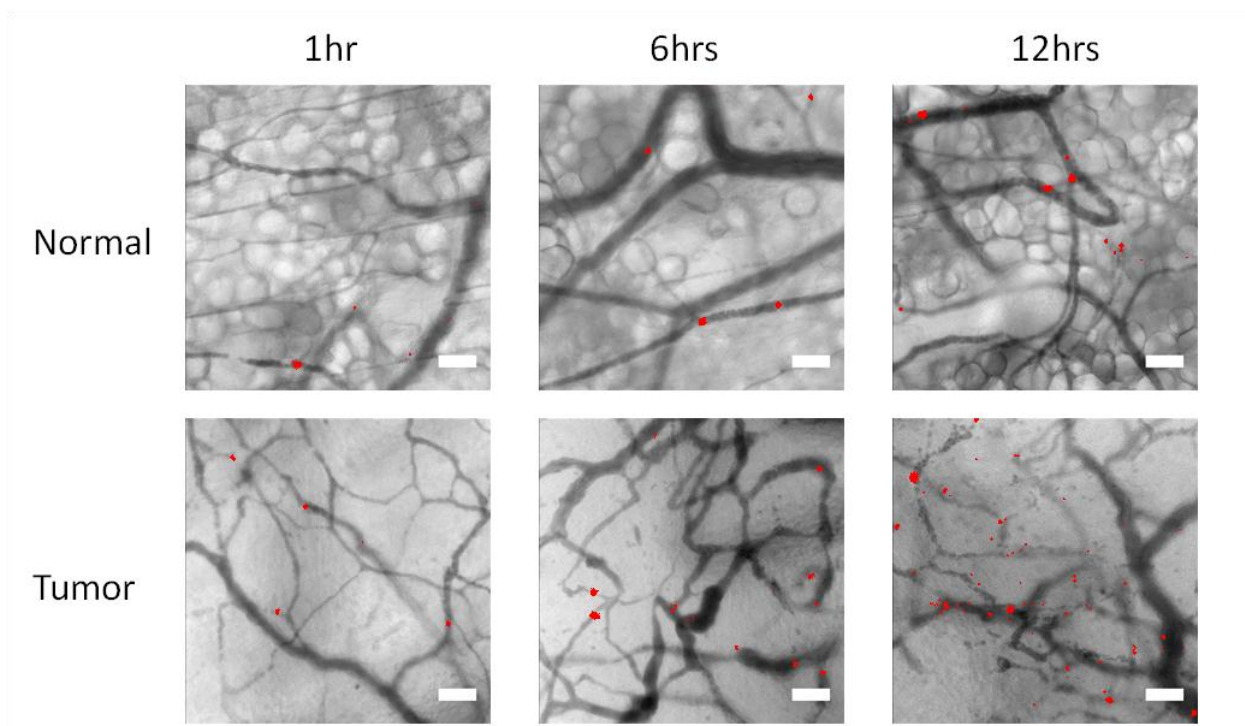


Figure 4-2. Microscopic images of postcapillary venules with transmitted light and fluorescence images were acquired. For example, accumulated Knock-in SSRBCs in capillary bed with red dot were overlaid on vascular images using 5X magnified objective. Top row: normal tissue, bottom row: tumor tissue; 1st column: after 1hr, 2nd column: after 6hrs, 3rd column: after 12 hrs post-injection of labeled SSRBC via tail vein. Scale bar represents 50 μ m.

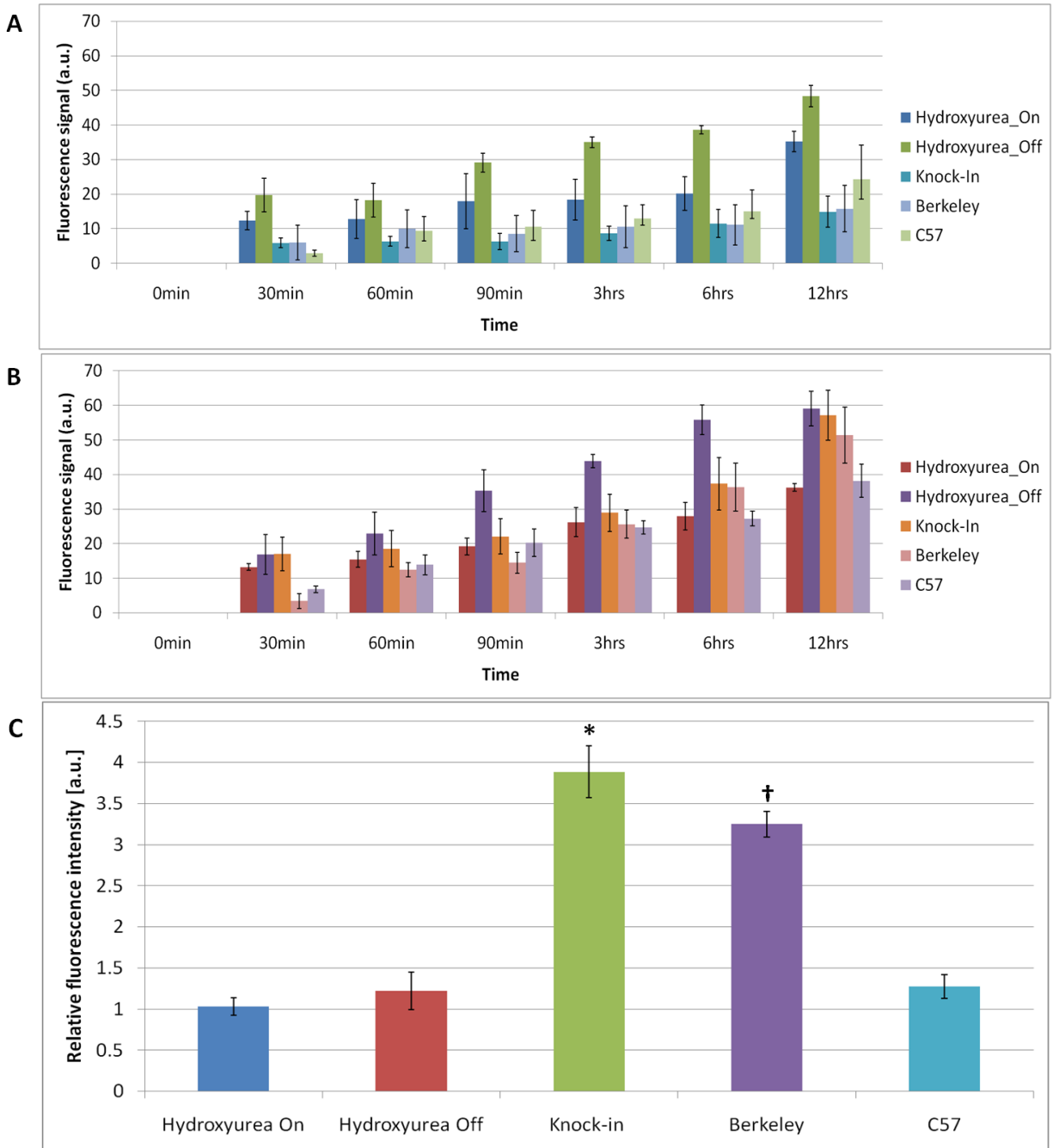


Figure 4-3. Bar graphs show numerical fluorescence intensities on selected ROIs in each group (mean±SD). (A) Fluorescence intensity on ROIs in normal sites after 0min, 30min, 60min, 90min, 3hrs, 6hrs, and 12hrs post-administration of SSRBCs,(B) Fluorescence intensities on ROIs in tumor sites at the same imaging time points,(C) Relative fluorescence intensity (signal from tumor sites ÷ signal from normal sites) were compared from accumulated RBCs on ROIs for each group after 12 hrs post-injection of RBCs and SSRBCs. * $p < 0.05$ compared with the other groups, † $p < 0.05$ compared with the other groups.

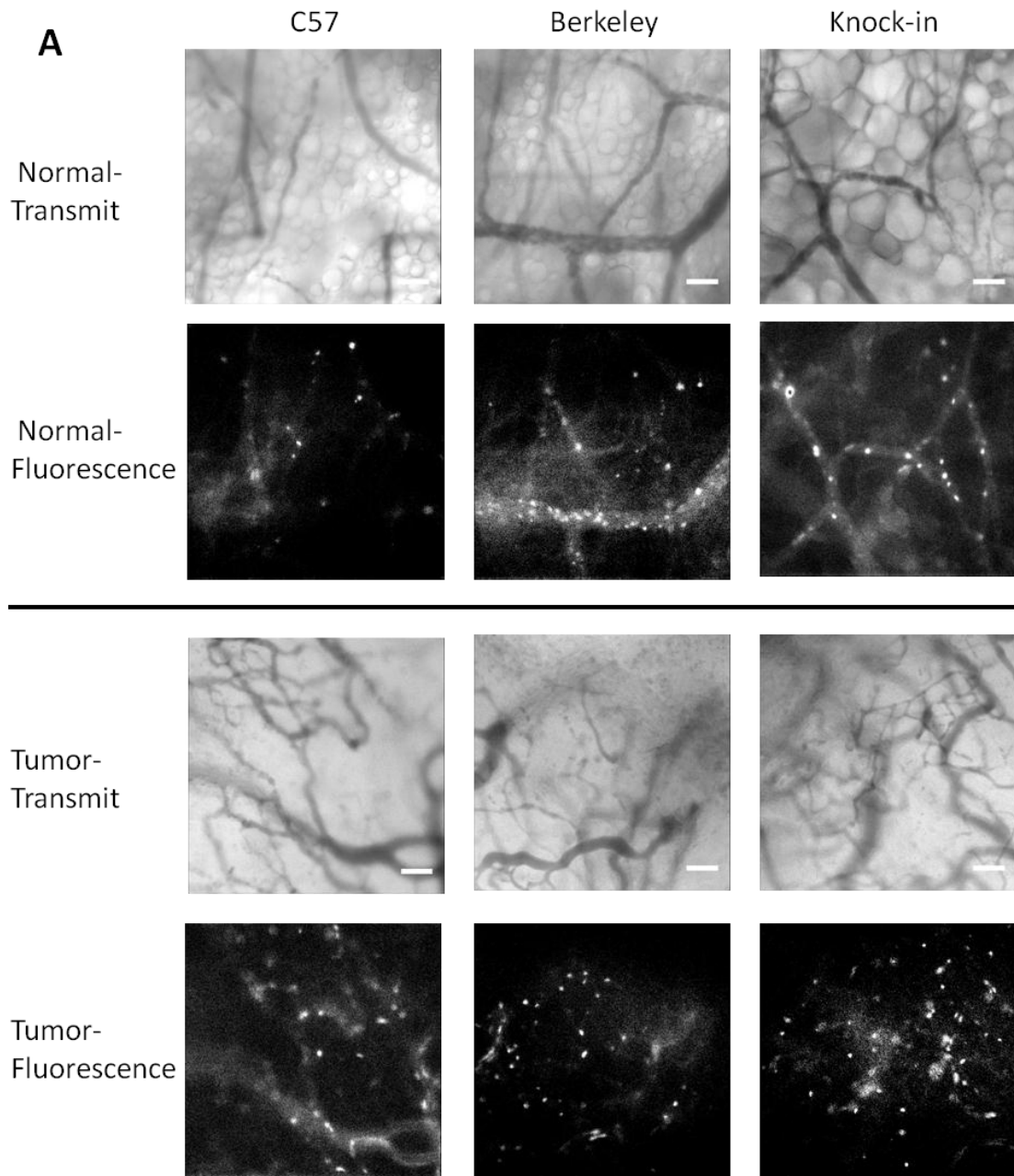
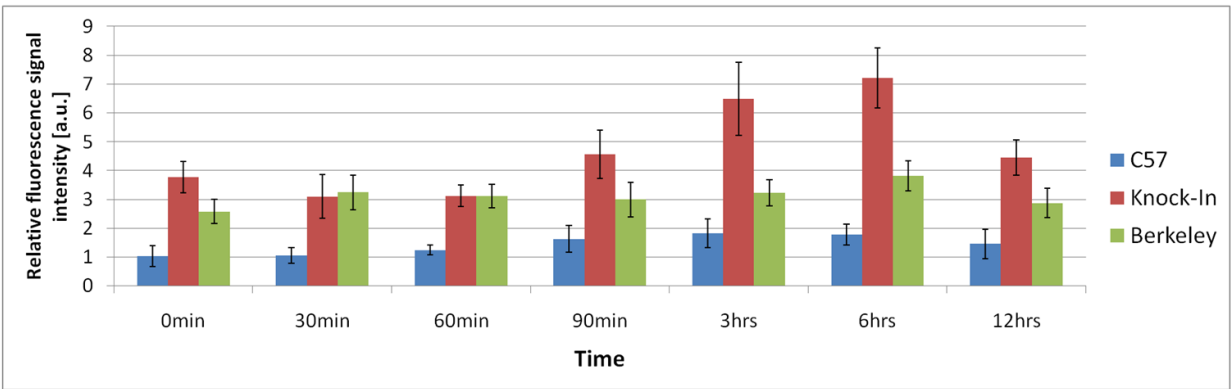


Figure 4-4. In-vivo numerical analysis of accumulated RBCs and SSRBCs using video recording with 20x objective. (A) Microscopic images of postcapillary venules with transmitted light and fluorescence images were acquired. 1st row: transmitted images for normal tissues, 2nd row: fluorescence images for normal tissues, 3rd row: transmitted light images for tumor tissues, 4th row: fluorescence images for tumor tissues; 1st column: C57 group, 2nd column: Berkeley group, 3rd column: Knock-in group. Scale bar represents 50 μ m. (B) Relative fluorescence intensity on ROIs after 0min, 30min, 60min, 90min, 3hrs, 6hrs, and 12hrs post-administration of SSRBCs and RBCs. (C) Comparison of relative fluorescence intensity from two different imaging techniques after 12 hrs post-administration of blood cells. * $p < 0.05$ compared with the other groups, † $p < 0.05$ compared with the other groups.

B



C

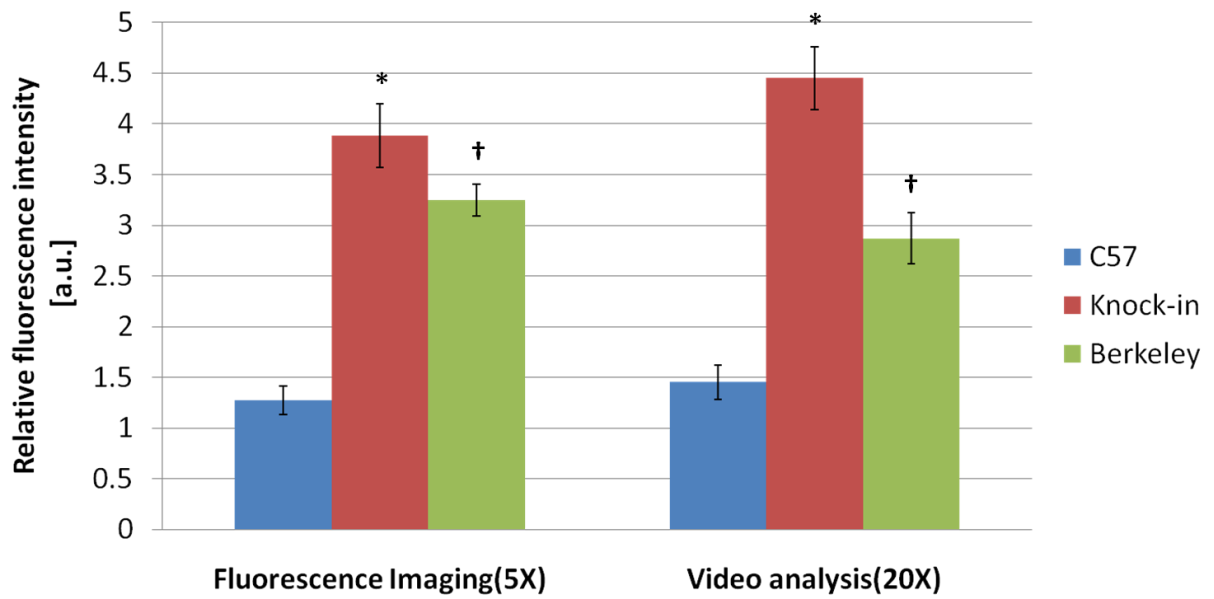


Figure 4-4. continued

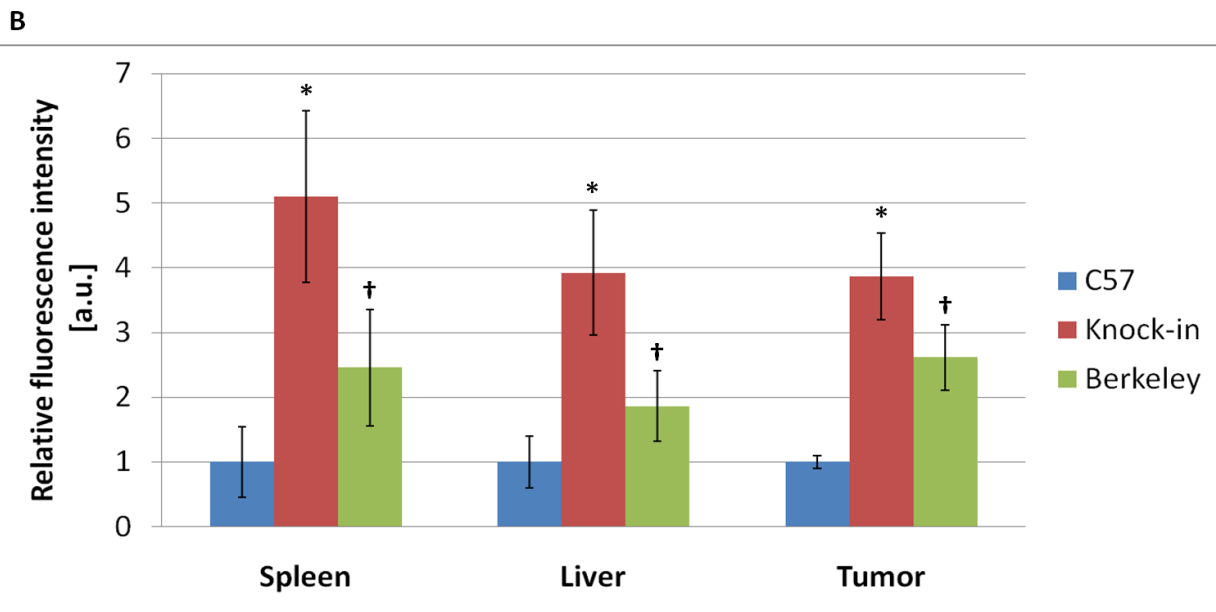
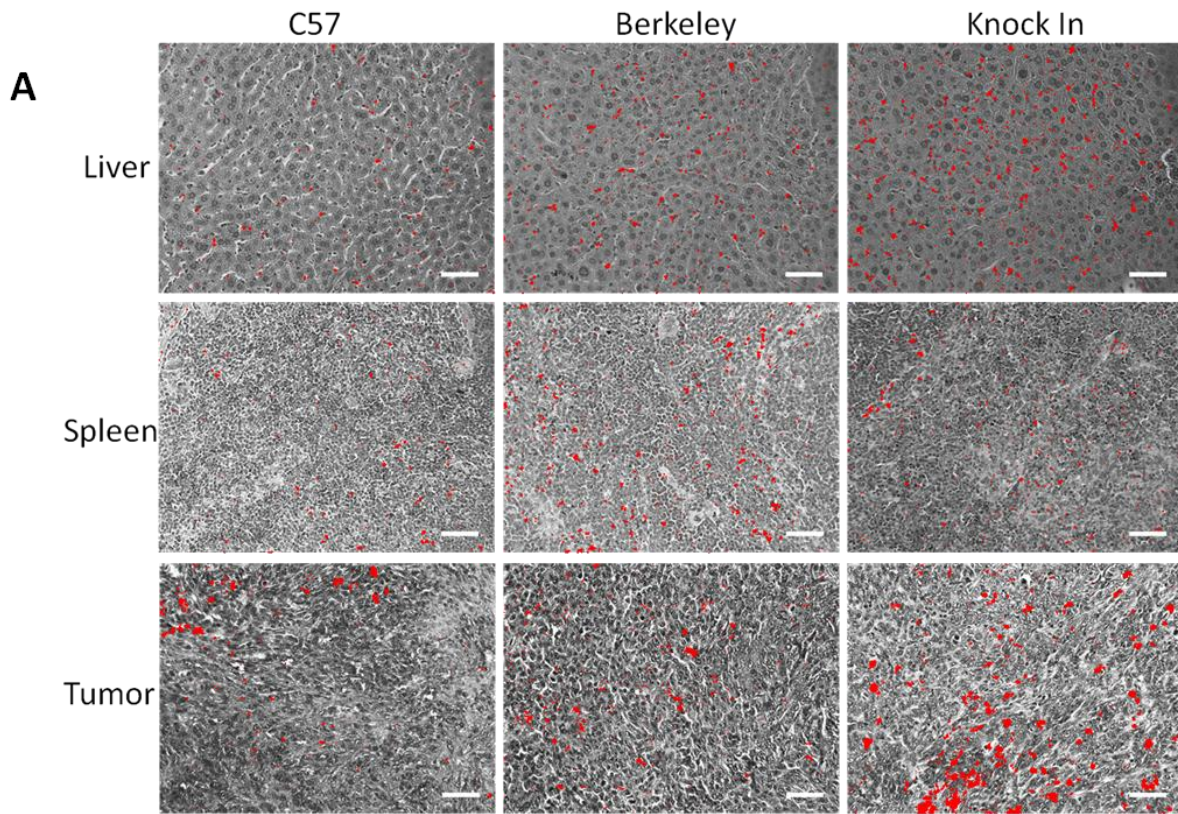


Figure 4-5. Fluorescently labeled cells in tissue specimens including liver, spleen and tumor were compared. Each specimen was stained by H&E method and segmented blood cells in red were superimposed to stained image. (A) Rows from top to bottom: liver, spleen, and tumor tissue; 1st column: C57 group, 2nd column: Berkeley group, 3rd column: Knock-in group. Scale bar represents 50 μ m. (B) Fluorescence signal from each organ infused by SSRBCs was divided by ones infused by RBCs. * $p < 0.05$ compared with the other groups, † $p < 0.05$ compared with the other groups. Scale bar is 50 μ m.

Discussion

Sickle cell disease is the most common inherited hematologic disease in the United States and it causes substantial morbidity and mortality. Hypoxia induced polymerization of HbS deforms the RBCs and causes massive cation loss as well as increased expression of adhesion receptors. The major pathologic processes involved in SCD are vaso occlusion, inflammation, procoagulant processes, hemolysis and altered vascular reactivity. However, a natural SCD animal model was not existing so that transgenic mouse models of SCD have been generated to investigate the complex pathophysiology and to evaluate potential therapies in-vivo and preclinical studies such as anti-sickling gene therapy.

In our experiment, two types of SCD mouse models (Berkeley and Knock-in mouse) were employed according to following reasons. Berkeley (Knock-out) mouse is one of the most commonly utilized SCD mouse model developed at Lawrence Berkeley National Laboratory in 1997 [188] . It expressed a very severe sickling with very low Hb concentration level (5 g/dL). Additionally, it survived for a mean of 14 months so that this relatively short life span was unfeasible to be employed for new therapies. However, it has demonstrated hematologic as well as histopathologic similarities and differences compared with human SCD patients. The similarities include sickling, hemolysis, reticulocytosis, severe anemia (hematocrit, 10~30%), leukocytosis, elevations of inflammatory cytokines, defects in urine concentrating ability, organ infarcts, glomerulosclerosis, and pulmonary congestion [199]. The differences include lower Hb concentration, thalassemic phenotype, smaller volume of SSRBCs and splenomegaly [188]. Another donor mouse was Knock-in SCD model. In this recently developed mouse model, the mouse globin genes was replaced by the γ gene of fetal hemoglobin

(HbF) and the human homologous genes. As a result, a high HbS expression in the fetus lacking HbF was decreased to avoid the fetal death between 3 and 6 months of age and increase a mean survival up to 18 months with slightly higher Hb concentration (8.9 g/dL) [190]. Therefore, Knock-in mouse model has been known as a better SCD mouse model for the therapeutic gene replacement than Berkeley mouse model [191].

The goal of this experiment was to find appropriate SCD mouse model presenting us more accumulation to endothelial cell due to overexpressed adhesion receptors and enhanced polymerization under tumoric environments characterized in terms of low pH, low oxygen tension, relatively low blood flow due to disorganized vasculature and higher blood viscosity, permeability and interstitial pressure [186]. Quantitatively analyzed results in Fig. 4-3 (C) demonstrated that relative fluorescence intensities for SSRBCs from murine SCD models had superior accumulative events to vessel walls as compared with human SSRBCs and C57 groups. Although absolute fluorescence signals of accumulated SSRBCs from Hydroxyurea-off group in tumor sites were higher than any other groups, relative fluorescence signal was decreased by elevated level of localized cells in normal sites. However, these results from current experiment were consistent with previous studies about tumor-preferential accumulations by SSRBCs under the hypoxic tumor environment [90, 91]. SSRBCs from Knock-in mouse model showed higher accumulation rates compared with Berkeley mouse model. Since the Berkeley mouse model had a more fragile membrane causing hemolysis, anemia and shorter lifespan in response to lack of human HbF than Knock-in mouse, relatively fewer accumulated SSRBCs from Berkeley were detected on endothelial cells [81, 200, 201]. In fact, Knock-in mouse model was recently developed by Wu et al. in 2006 [190] so

that preceding in-vitro studies may be recommendable to have better understanding on the subject of measurement of hematocrit, hemolysis rate, the percentage of sickled cells or rheologic characterization in blood stream under similar condition as tumor sites between two groups. The experiments in this chapter demonstrate that blood from the mouse models of SCD can effectively replicate the tumor accumulation of human SSRBCs that was previously reported in animal models and in clinical cases.

CHAPTER 5 IN-VIVO DELAYED PHOTOHEMOLYSIS MEASUREMENT FROM PHOTOSENSITIZED SSRBCS LOADED WITH CALCEIN IN 4T1 TUMOR BEARING MOUSE MODEL

In the previous chapter, the tumor-selective accumulation of SSRBCs by SCD human patients and mouse models was effectively demonstrated. Our intravital microscopic imaging system was employed to monitor the alteration of tumor microvasculature and functional changes of HbSat. Fluorescence images acquired from our imaging system were applied for quantitative analysis of the accumulated SSRBCs in the blood vessels. As we assumed, SSRBCs from SCD patients and animal models expressed the natural tumor preferential accumulation and it partially verified the potential of SSRBCs as a novel drug carrier. Among the SSRBCs groups, the Knock-in mouse model demonstrated the highest relative fluorescence intensities in selected ROIs in tumor and normal sites. Based on this result, Knock-in SCD mouse blood was used with in-vitro DPH measurement in a controlled manner, and in-vivo experiments using immunodeficient mice.

In previously published experiments with drug loaded normal RBCs, several osmosis-based techniques including hypotonic hemolysis, hypotonic dilution, hypotonic dialysis, hypotonic preswelling, and osmotic pulse have been developed for drug loading and were possibly applicable to SSRBCs [41, 59-61]. There are several advantages of the hypertonic preswelling method. This method employs simpler and faster procedures than the dialysis method so that it causes minimal destruction of the cell membrane with relatively high entrapment efficiency [42, 62]. As a result of moderate loading condition, the resulting resealed RBCs in systemic circulation has comparable lifespan to that of the normal RBCs [42]. Hence, hypotonic preswelling

method was selected and modified for SSRBCs based on previously reported methods for normal RBCs [202].

Characterization of In-vitro DPH experiment for normal RBCs was performed to examine the photohemolysis reactions in relation to various photosensitizer concentrations, incubation temperatures, irradiation temperatures, irradiation power and irradiation time similar to Al-Akhras and Grossweiner et al. [99-101]. However, careful manipulation was required to handle the sensitive carriers for temporally controllable dye release method from photosensitized SSRBCs with the photosensitizer protoporphyrin IX (PpIX). Since lots of SSRBCs accumulation was observed around 12 hrs after administration of the cells via tail vein injection in the previous chapter, various parameters were modified and optimized for t50 at this time in this experiment. The fractional hemolysis was determined from the amount of Hb released into the solution normalized to an equivalent solution of fully lysed red blood cells. The results from in-vitro DPH experiment were analyzed and the theoretical time required for t50 was calculated by Gompertz function [101].

Microdialysis methodology has been a powerful sampling technique capable of continuous monitoring the concentration of unbound drugs both for in-vitro and in-vivo investigation of both endogenous and exogenous substances [103, 104]. It has been applied and broadened for various pharmaceutical studies including the transdermal delivery of drugs [106], tissue pharmacokinetics [107], and tissue pharmacodynamics [108, 109]. Additionally, this monitoring technique has been employed in various tissue and organs of human or murine models such as liver [110], heart [111], skin [109], blood vessels [112], placenta [113], stomach [114], ear [115], and tumor tissue [116-118]. The

microdialysis methodology was employed for in-vivo DPH measurement, and fluorescence intensities of the collected dialysates from tumors were compared to healthy muscle tissues by microplate reader at 12 hrs and 24 hrs post injection.

In this experiment, we mainly focused on the controlled dye release from resealed SSRBCs group. Four different groups including free calcein, calcein loaded SSRBCs (from Knock-in mouse) with or without photoactivation, and calcein loaded normal RBCs (from wildtype mouse) with photoactivation by 1min irradiation were performed and compared with each group.

Materials and Methods

Materials

Dulbecco's Phosphate Buffered Saline (DPBS with 1mM of Ca^{2+} and 0.5mM of Mg^{2+} without phenol red, SH30264.01, HyClone), Phosphate Buffered Saline (PBS, HyClone), 10X Phosphate Buffered Saline (10X PBS, HyClone) and Ringers's solution (for mammals, S77939, Fisher Scientifics) were obtained from Fisher Scientifics (Pittsburg, PA). Calcein (623Da, ex: 495nm and em: 520nm, 019K1223, Sigma) and Protoporphyrin IX (PpIX, 1127K1570, Sigma) were obtained by Sigma-Aldrich (St. Louis, MO). Microdialysis probes (CMA 20 Elite Microdialysis probes, 10mm of membrane length, 20 kDa of cut-off, 8010436, CMA Microdialysis) were commercially available from CMA Microdialysis (Solna, Sweden).

Preparation of Blood Cells

All in-vivo experiments were carried out under a protocol approved by the University of Florida Institutional Animal Care and Use Committee (IACUC). SSRBCs from Knock-in mouse were prepared by Dr. Angela E. Rivers (M.D, Ph.D. Assistant Professor, Department of Pediatrics, Division of Hematology/Oncology, University of

Florida). Donor mice were anesthetized by 1%~2% isoflurane in air and blood samples were obtained by retro-orbital bleeding using a heparinized glass pipette. Normal RBCs from a donor C57BL/6 wildtype mouse were prepared by the author. Donor mice were anesthetized by intraperitoneal injection of ketamine (100mg/kg) and xylazine (10mg/kg) and normal RBCs were obtained by cardiac puncture. Obtained blood samples were stored in ethylenediaminetetraacetic acid (EDTA) tubes at 4°C until use.

Preparation of Loaded Blood Cells with Calcein

To load fluorescent dye into SSRBCs, the hypotonic preswelling method, one of the osmosis-based loading methods into normal RBCs, was selected and modified [202]. It was derived from the fact that exposing RBCs in a hypotonic solution leads to an enhanced permeability of the membrane and enlargement of pores with diameters of 200 to 500Å (20~50 nm) in the membrane when it reaches hemolysis [66].

The SSRBCs in about 1ml of DPBS solution were washed via temperature controllable centrifugation at 1600 rpm at 4°C for 7min and resuspend in DPBS. The supernatant was discarded and this step was repeated until its supernatant was clear. Packed SSRBCs were split by 200µl into several polypropylene tubes and 1.2ml of hypotonic DPBS solution with osmolarity of 0.67 was added into each tube. The cell suspension was gently mixed for 5 min and centrifugated at 1600 rpm at 4°C for 7 min to separate swollen cells. The supernatant was discarded and a 40µl of aliquot of a hemolysate (SSRBCs:DIH₂O = 1:1 (v:v)) was added gently above the swollen SSRBCs to compensate loss of Hb and intracellular components during this loading procedure. In addition, it led the decrement of the osmolarity shock between the swollen cells and aqueous dye solution. Then 250µl of aqueous hypotonic solution of calcein (77.8 µg ml⁻¹) was gently added in each tube and mixed for 5 min. When the transparency of

supernatant was suddenly increased and white ghost cells were observed between supernatant and packed cells, hemolysis point of the SSRBCs was achieved. At this point, 100µl of hypertonic solution (10X PBS) was added rapidly in each tube to reseal the pores created during cell swelling and lysis procedures by hypotonic environment. Cell suspensions were mixed by gentle swirling for 5 min and incubated at 37°C for 30min to reanneal the resealed cells. The SSRBCs were washed twice in DPBS to remove unloaded calcein and resuspended to give an expected SSRBCs concentration (8×10^8 cells ml^{-1}) for further procedures. That concentration was acquired by repeated absorbance measurement of lysed Hb from intact to completely lysed SSRBCs using spectrophotometer (NanoDrop™ 1000, Nanodrop, Wilmington, DE) until maximum lysis had occurred.

Preparation of Photosensitized Blood Cells by PpIX

The 1ml of SSRBCs in the tube was centrifuged at 1600 rpm at 4°C for 7 min and the supernatant was discarded. Concentrated SSRBCs were incubated with 6ml of PpIX dissolved in DPBS solution (20µM) at 37°C for 30min and it was swirled every 15min during the incubating period. The SSRBCs were washed twice in DPBS to remove unbound photosensitizer and resuspended in 3ml DPBS solution. Treated SSRBCs were stored at 4°C until it use. To protect the sample from ambient light, the all tubes were covered by aluminum foil during all procedures.

In-Vitro Delayed Photohemolysis Measurement

In vitro DPH measurement was previously described in Chapter 2. Briefly, calcein loaded and photosensitized 8×10^8 cells of normal RBCs from C57 wildtype mouse by 50 µM of PpIX and SSRBCs from Knock-in mouse by 25 µM of PpIX in 3ml were prepared. Two different types of blood sample were prepared according to its own purpose and

limited number of Knock-in mice. Normal RBCs were expected to present various t_{50} depending on the irradiation time ($t_{irr} = 0, 9, 11, 13, 15, 17$ and 19 min). Therefore, it could provide baseline data regarding characteristics of DPH for SSRBCs.

Each sample was transferred to a glass cuvette and was positioned in temperature controlled cuvette holder. Normal RBCs and SSRBCs suspensions were irradiated by 0.33W and 0.08W halogen lamp for various irradiation times ($t_{irr} = 0, 9, 11, 13, 15, 17$ and 19 min for normal RBCs and $t_{irr} = 1, 5, 10$ and 20 mins) to initiate photochemical reaction by PpIX at room temperature. Different light doses were achieved by varying the irradiation time for constant incident irradiance. After irradiation, the thermal reaction was initiated by increasing temperature of cuvette holder up to body temperature (37°C) in dark. In DPH method, photohemolysis rates were measured from the beginning of incubation in dark after irradiation period. When the temperature reached at 37°C , $30\mu\text{l}$ blood samples were collected periodically. The collected blood sample was split into packed SSRBCs and supernatant by immediate centrifugation and then $20\mu\text{l}$ of supernatant was stored in conical tubes to measure the absorbance for fractional photohemolysis using a spectrophotometer. The fractional hemolysis was determined from the amount of Hb released into the solution normalized to an equivalent solution of fully lysed red blood cells.

Gompertz Function

Empirical results were quantitatively analyzed by kinetics model to calculate the dependence of the irradiation time by the Gompertz function. The original Gompertz equation was described in equation (1). Gompertz function was employed to calculate the two parameters a and b regarding fractional photohemolysis by PpIX in equation (2) and estimate theoretical time required for 50% fractional photohemolysis (t_{50}) in

equation (3). This function parameters a , b , and t_{50} were important predict of the average DPH rate and this model has been assessed to investigate the hemolysis rate of photosensitized RBC by PpIX [101]. The empirical t_{50} was measured and compared with the theoretical t_{50} determined by equation (3) described in Chapter 1. R^2 values were computed for the fit of the empirical t_{50} to the theoretical values of t_{50} by the Gompertz function.

Tumor Cells

4T1 mouse mammary adenocarcinoma cells were generously provided by Dr. Mark W. Dewhirst (Duke University Medical Center, Durham, NC). The cells were cultured as a monolayer in DMEM (Cellgro, Inc., 1X, 4.5 g/l glucose, L-glutamine and sodium pyruvate) with 10% fetal bovine serum (Biowhittaker, Inc.), 1% L-glutamine (Clonogen, Inc.) and 1% penicillin streptomycin (Clonogen, Inc.). Single cell suspensions were prepared in DMEM without serum at room temperature and stored at 4°C until its injection into mouse models.

Animal Models

All in-vivo experiments were carried out under a protocol approved by the University of Florida Institutional Animal Care and Use Committee and conformed to the NIH Guide for Care and Use of Laboratory Animals. Female athymic (nu/nu) nude and wild type (C-57) mice between 20 and 26 g were obtained from Harlan Laboratories for this study.

Single cell suspensions of 1×10^5 4T1 cells in 100 μ l were prepared in DMEM without serum at room temperature and injected subcutaneously over the left quadriceps muscle of athymic nude mouse under anesthesia by 1~2% isofluorane in air. After the tumor cell injection, all mice were housed in an environmental chamber

maintained at 33°C and 50% humidity with free access to food and water and standard 12hrs light/dark cycles. When the tumor size reached to 10 mm in diameter, a 200µl bolus of treated RBCs in DPBS solution (Hct: 50% V/V) or calculated concentration of free calcein (5µg ml⁻¹) equal to the amount loaded into RBCs was administered via tail vein. Four different mouse groups were prepared and summarized in Table 5-1.

Table 5-1. Categorized groups for in-vivo DPH measurement of SSRBCs to tumoric microvasculature experiment.

Group	Blood type	Calcein	PpIX	t_{irr} [min]	N
RBC calcein PpIX 1min	Wildtype mouse (C57BL/6)	Y	Y	1	3
SSRBC calcein PpIX 1min	Knock-in SCD mouse	Y	Y	1	3
SSRBC calcein Free calcein	Knock-in SCD mouse N/A	Y Y	N N	0 0	3 3

Free calcein (Free calcein group), calcein loaded SSRBCs with (SSRBC calcein PpIX 1min group) and without (SSRBC calcein group) photoactivation, and calcein loaded normal RBCs with photoactivation (RBC calcein PpIX 1min group) by 1min irradiation were injected animal models when the injected tumor mass reached 10mm in a diameter.

In-vivo Delayed Photohemolysis using Microdialysis Tubing

When the tumor size at injected areas reached to about 10 mm in diameter, manipulated blood cells were systemically administered by tail vein. For in-vitro DPH measurement experiment, photosensitized blood cells were photoactivated by irradiation for 1 min ($t_{irr} = 1\text{min}$) prior to their administration. To investigate the controlled release rates of calcein from photoactivated SSRBCs in tissues, microdialysis probes were inserted at the sites for collection of dialysate. Microdialysis probes and tubing connectors were soaked in Ringers's solution and ethanol for 5min before use,

respectively. After that, the probes were perfused with Ringers's solution to purge air bubbles in tubing for 30min at a flow rate of $2 \mu\text{l min}^{-1}$ by syringe pump. The probes were then placed 5mm below the surface for tumor tissue through a plastic guide cannula. A probe was placed into the quadriceps muscle as a control site through a small incision made on the skin of implantation site with a small scalpel blade. The probe were inserted in a similar way in tumor tissue and sutured to skin. Dialysate samples were collected by perfusing with Ringers's solution at the rate of $1 \mu\text{l min}^{-1}$ during 4hrs intervals from the tumor tissue and the quadriceps muscle. Each sample was collected at a variety of time points after the photosensitized SSRBCs cells or free calcein injection via tail vein. Fluorescence signal of calcein in the dialysate could be analyzed using microplate reader and compared. Statistical analysis was performed using SPSS software (SPSS for Windows; SPSS Inc., Chicago, Illinois, USA) and analysis of variance (ANOVA) followed by a Bonferroni's post hoc test were used to assess the statistical significance of the differences between the groups.

Results

Efficacy of Calcein Loading Rate into Sickle Red Blood Cells

Hypotonic preswelling method for loading calcein into SSRBCs from Knock-in mouse was modified from the protocol for normal erythrocyte [202] and performed. Light microscope and fluorescence flow cytometry techniques were employed to analyze the fraction of SSRBCs loading calcein in Fig. 5-1. Untreated SSRBCs, treated SSRBCs without calcein and treated SSRBCs with calcein samples by modified hypotonic preswelling method were set up for fluorescence flow cytometry test. Example microscopic image of SSRBCs loading calcein is shown in Fig. 5-1(A) and distribution of fluorescence signals by flow cytometry is shown in Fig. 5-1(B). Modified hypotonic

preswelling showed 85.46% of entrapping efficacy of calcein into SSRBCs and this result was consistent with the fractional data of various hypo-osmotic lysis methods in Table 1-5.

In-vitro Delayed Photohemolysis Measurement of Photosensitized Sickle Red Blood Cells by PpIX

DPH measurement was performed using photosensitized normal RBCs from C57 wildtype mouse with PpIX first. Optical absorbance of the fractional hemolysis rates (0%, 20%, 40%, 60%, 80% and 100%) from the amount of Hb released into the solution was determined by spectrophotometer at 415nm (Fig. 5-2 (A)). The sample of various hemolysis rates was normalized and linearly fitted to an equivalent solution of fully lysed red blood cells (Fig. 5-2 (B)). Normal murine RBCs were photosensitized by 50 μ M of PpIX and photoactivated by 0.33W halogen lamp based on various irradiation time (t_{irr} = 0, 9, 11, 13, 15, 17 and 19 min) at 24°C. DPH measurement was created when the temperature of sample solution reached at 37°C in dark. Supernatant from the centrifugated sample in cuvette was collected every 5 min up to 105min and determined by spectrophotometer. Various sigmoidal curves depending on different irradiation time are presented in Fig. 5-2 (C). Each DPH curve showed a typical sigmoidal shape and fractional Hb release rate were possibly controlled by the various light energy dose according to the irradiation time. The released Hb concentration from photoactivated SSRBCs was accelerated by increased exposure time. Photohemolysis measurements from non-photoactivated RBCs were negligible (< 10%) at final measurement time point (105 mins) in dark (Fig. 5-2 (C)). It should be noted that thermal reaction by itself without photochemical activation couldn't cause significant photohemolysis. Combined two procedure such as photochemical and thermal reactions generated DPH.

Similar experiments were repeated for Knock-in SSRBCs and in-vitro DPH results are shown in Fig. 5-3. From the results in Chapter4, systemically administered SSRBCs could substantially accumulate in tumor sites about 12 hrs post-injection. Therefore, 50% fractional photohemolysis (t_{50}) rate in the range of about 12~24 hrs was desirable. All applicable parameters (i.e., light dose, irradiation time, and concentration of PpIX) from normal RBCs experiment were modified and optimized to produce significant photohemolysis at desired time point. For example, light dose (from 0.33 to 0.08W), irradiation time range (from 9~19min to 1-20min), and concentration of PpIX (50 μ M \rightarrow 25 μ M) were customized. DPH measurement of SSRBCs by various t_{irr} (1, 5, 10, and 20min) and the results from Gompertz analysis are demonstrated in Fig. 5-3 and average value of r^2 was over 0.99.

Analysis of in-vitro Delayed Photohemolysis Measurement by Gompertz Function

In this experiment, t_{50} could be adjusted by only one parameter (t_{irr}), whereas the other factors, such as concentration of PpIX, irradiation temperature, incubation temperature and light energy dose, were fixed. DPH measurements from Fig. 5-3 were analyzed by Gompertz function. The calculated parameters (a and b) accompanied with the best fit to empirical curves by equation (2) and empirical and theoretical time t_{50} by equation (3) are summarized in Table 5-2. The results are plotted in Fig. 5-4 and linear fitting model applied to each parameter (a , b and t_{50}) presented high r^2 values (>0.98). in addition, Gompertz function could effectively estimate theoretical t_{50} compared with empirical t_{50} ($r^2 = 0.9844$).

In-vivo Controlled Calcein Release Form Sickle Red Blood Cells

Dialysate samples were collected by perfusing with Ringers's solution at the rate of 1 μ l min^{-1} during 4hrs intervals from the tumor tissue and the quadriceps muscle. In-

vivo DPH measurements from dialysate samples collected at 12 hrs and 24 hrs post administration are shown in Fig. 5-5 (A).

The fluorescence signal of released calcein from photoactivated SSRBCs loaded with calcein group by 1min irradiation (SSRBC calcein PpIX 1min group) collected from both sites (tumor and normal sites) at 24hrs post injection demonstrated statistical difference ($p<0.05$) from the other groups. However, that of 12hrs measurements from same group but only in tumor sites was statistically different ($p<0.05$). That of the other groups including SSRBC calcein, RBC calcein PpIX 1min, and free calcein group had similar fluorescence intensity at 12 and 24 hrs post injection.

Relative fluorescence intensity measurements showed consistent results. To calculate relative fluorescence intensity, the fluorescence signals of released or existing calcein at tumor sites at 24hrs post injection was divided by that of normal sites. It is shown in Fig. 5-5 (B) and only SSRBC calcein PpIX 1min group was statistically different from the other groups ($p<0.05$)

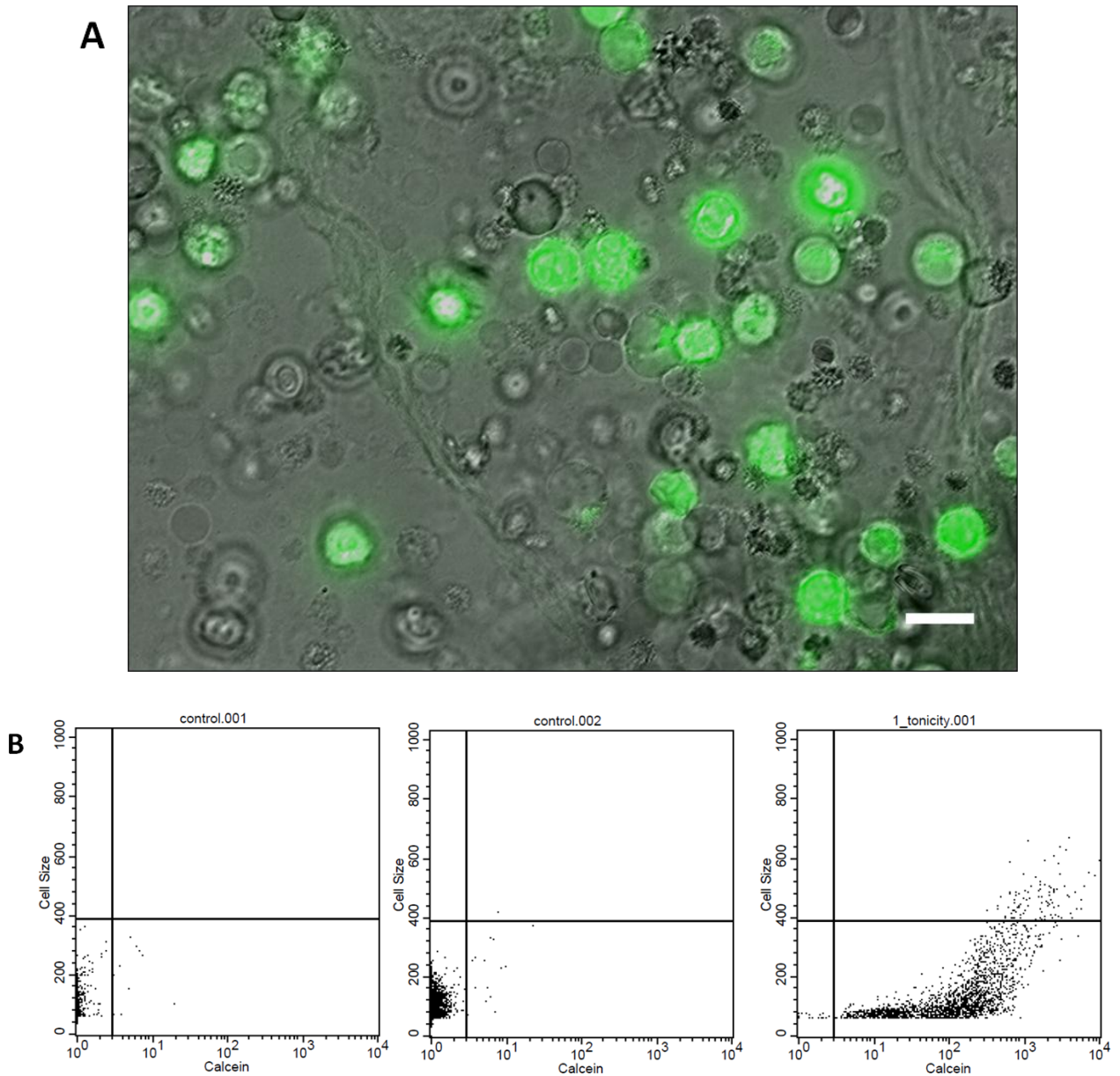


Figure 5-1. Light microscope and fluorescence flow cytometry techniques were employed to analyze the efficiency of hypotonic preswelling method to SSRBCs. A: Microscopic fluorescence image of calcein entrapped in SSRBCs was superimposed on the transmitted light image. Scale bar shows 15 μ m. B: Flow cytometric analysis of SSRBCs loading calcein. X axis represents the fluorescence intensity from entrapped calcein in the SSRBCs. Y axis represents size of cells. Left: normal SSRBCs, Middle: sham treated SSRBCs, Right: calcein loaded into SSRBCs.

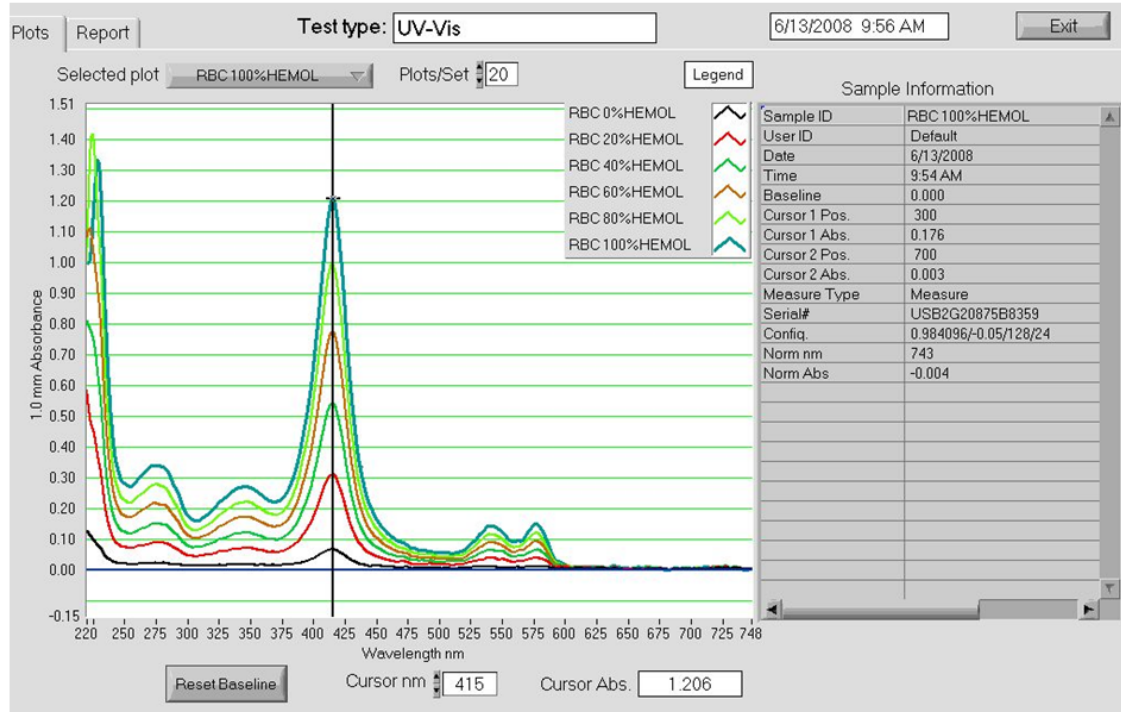
A

Figure 5-2. Delayed photohemolysis in normal canine RBCs photosensitized with PpIX were measured at 415nm. (A) Supernatant of collected photoactivated blood sample was measured at 415nm using spectrophotometer. (B) Linearly fitted model for optical density of various hemolysis (0%, 20%, 40%, 60%, 80% and 100%) fraction of normal canine RBCs at 415nm as reference group. (C) Photosensitized normal canine RBCs by 50 μM of PpIX were irradiated by 0.33W halogen lamp for various irradiation time ($t_{irr} = 0, 9, 11, 13, 15, 17$ and 19 min) and fraction of photohemolysis were acquired. Photoactivation by irradiation was performed at 24°C followed by incubation in dark at 37°C, respectively.

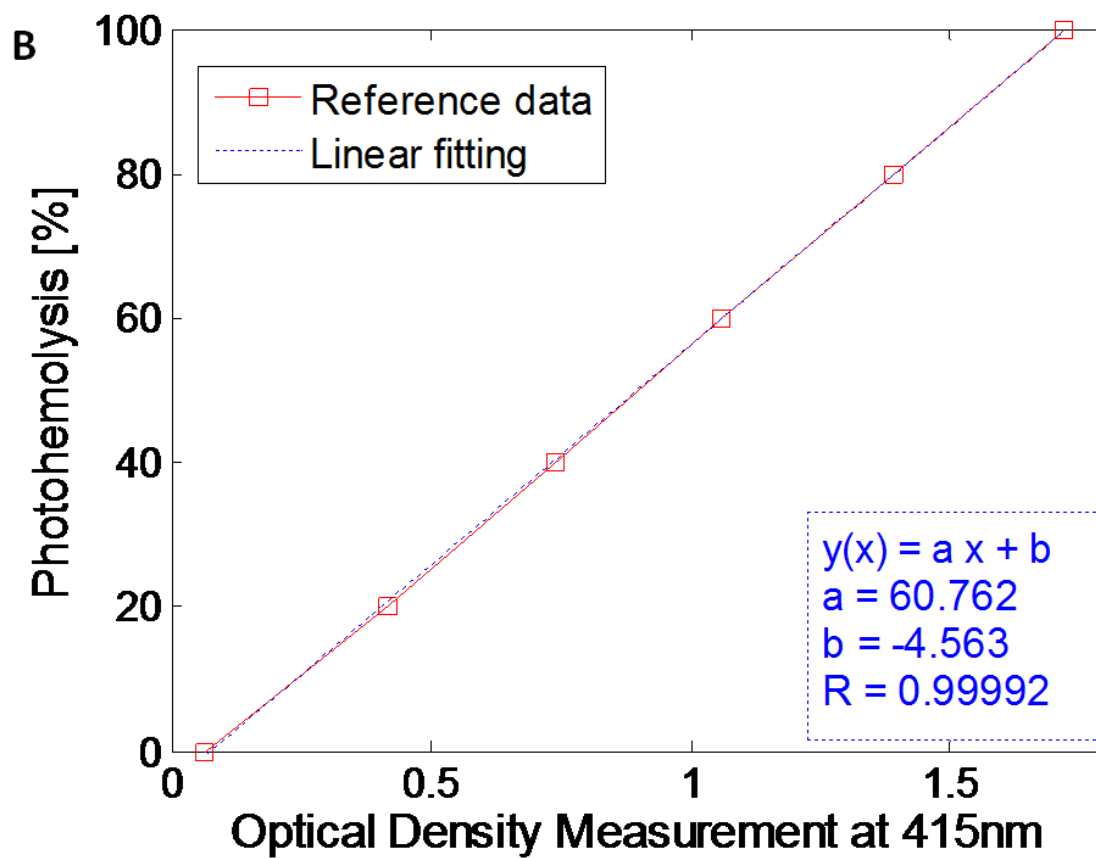


Figure 5-2. continued

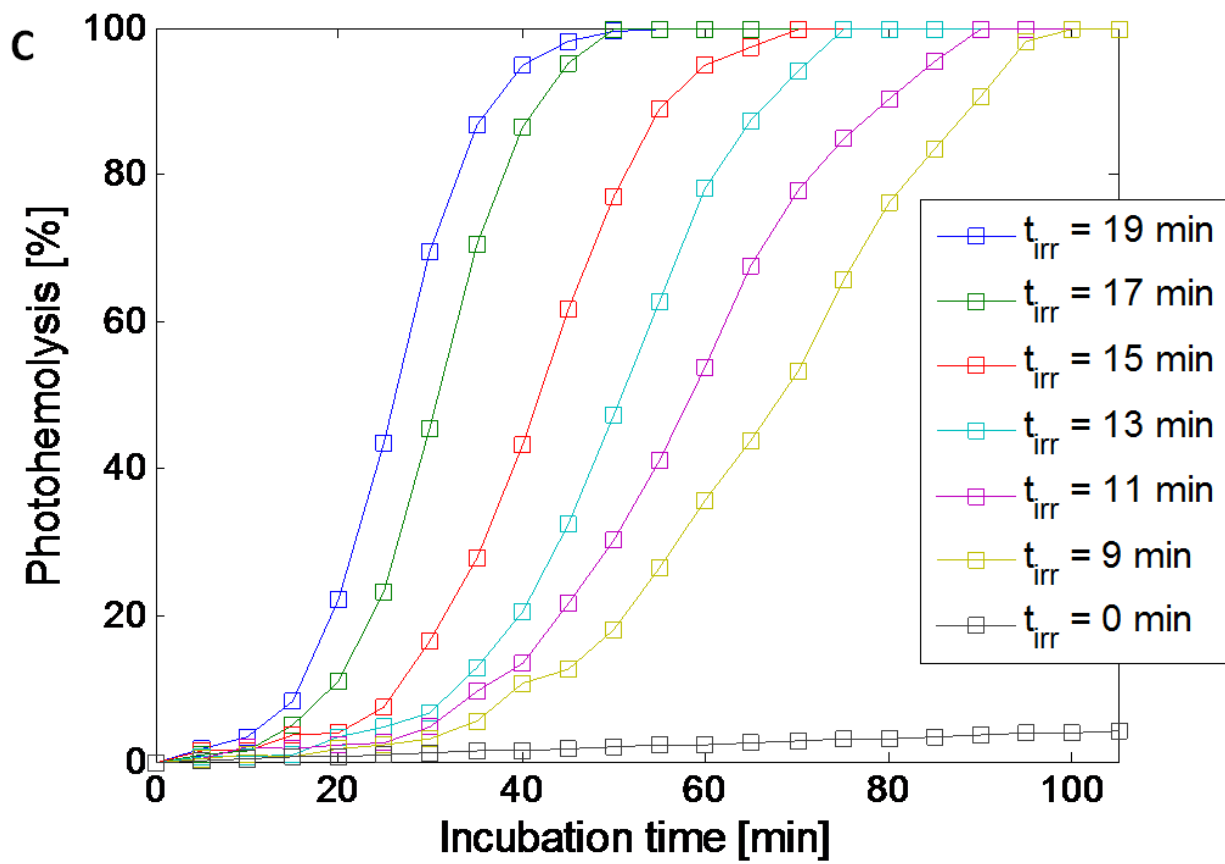


Figure 5-2. continued

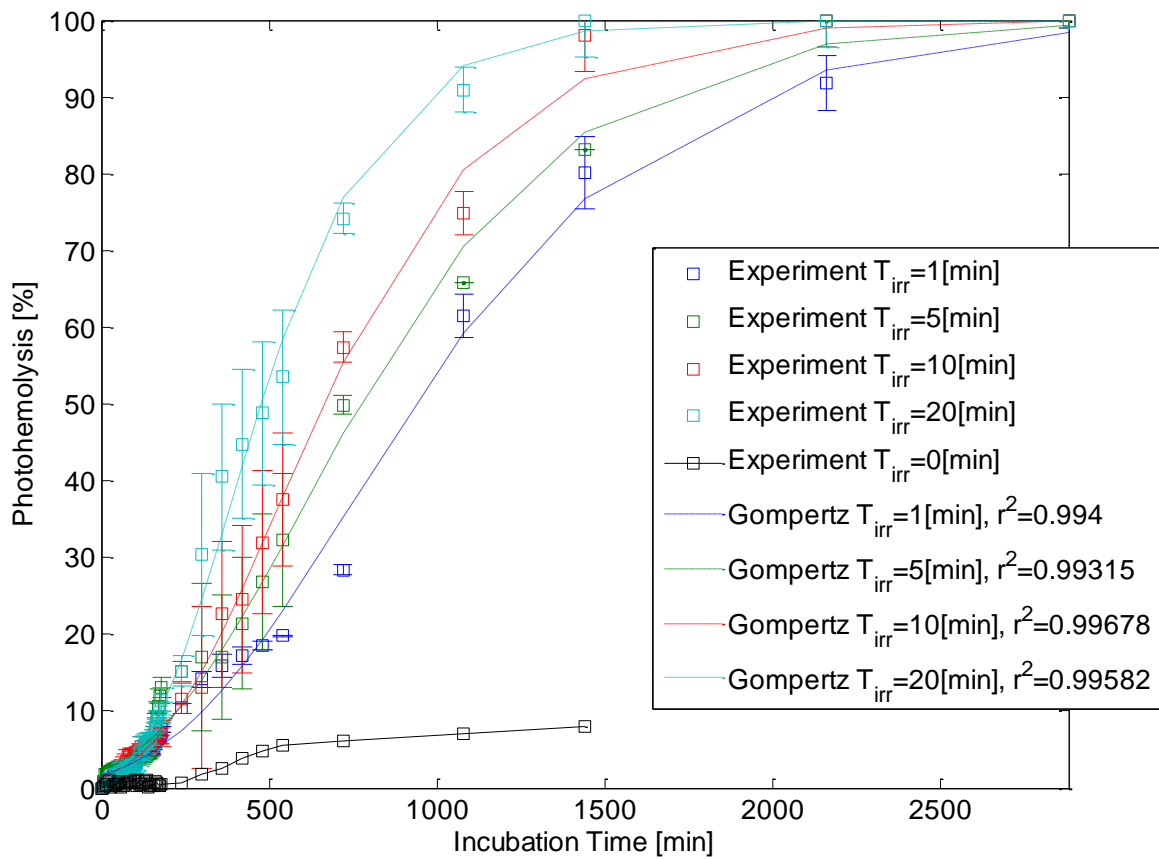


Figure 5-3. Fractional photohemolysis rates of photosensitized SSRBCs by 25 μM of PpIX were measured. The cells were irradiated by 0.08W halogen lamp at 24°C during various irradiation time (1, 5, 10, and 20min) and incubated in dark at body temperature (37°C). Open square with error bar represents experimental data by in-vitro optical density measurements and dotted line is fitting curves by Gompertz function. r^2 values were calculated.

Table 5-2. SSRBCs with 25 μ M PpIX irradiated with 0.08W halogen lamp at various irradiation times at fixed irradiation and incubation temperature

t_{irr} [min]	t_{50} [min] ^a	t_{50} [min] ^b	a	b [min ⁻¹]	T_{irr} [°C]	T_{inc} [°C]
1	940	934.4300	4.0906	0.0019	24	37
5	777	809.6226	4.1142	0.0022	24	37
10	664	653.4984	4.3192	0.0028	24	37
20	476	477.4097	4.6782	0.0040	24	37

^a Empirical results obtained from data curves.

^b Theoretical values calculated from Equation (3).

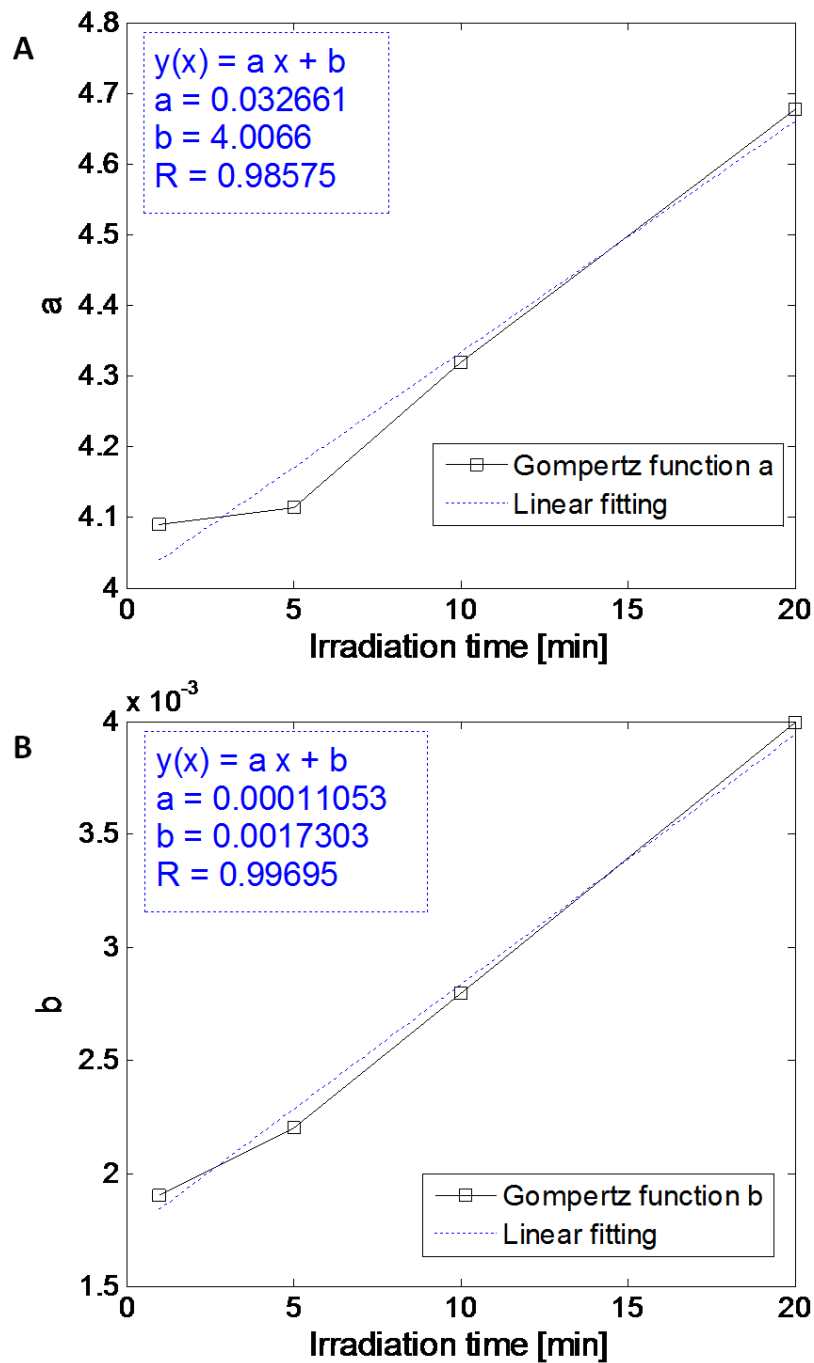


Figure 5-4. Parameters for Gompertz function were calculated based on fractional DPH measurement of SSRBCs carrying calcein with various irradiation time (t_{irr}). (A) x axis: irradiation time [min], y axis: parameter a in Gompertz function. $r^2 = 0.98575$. (B) x axis: irradiation time [min], y axis: parameter b in Gompertz function. $r^2 = 0.99695$. (C) x axis: irradiation time [min], y axis: t_{50} in experimental results with black solid line and estimated t_{50} values by Gompertz function. $r^2 = 0.98444$.

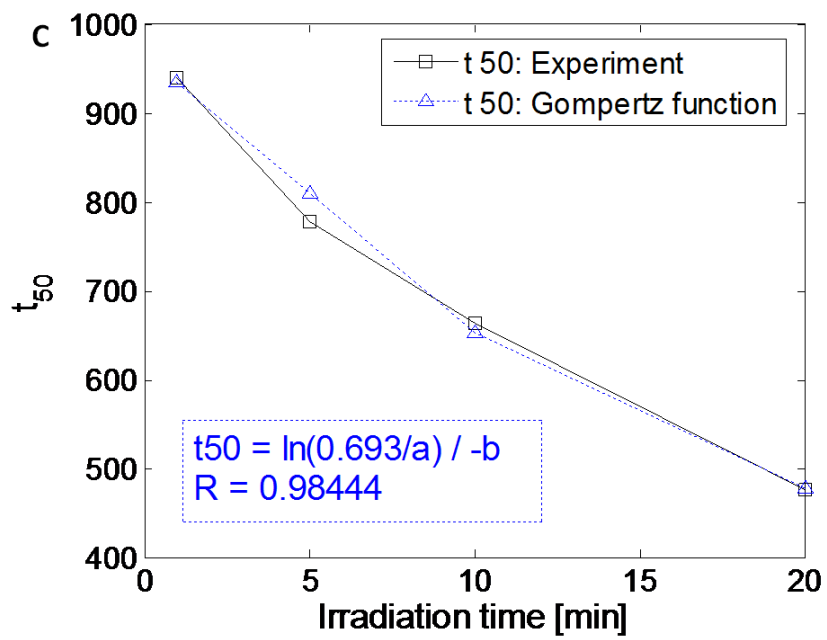


Figure 5-4. continued

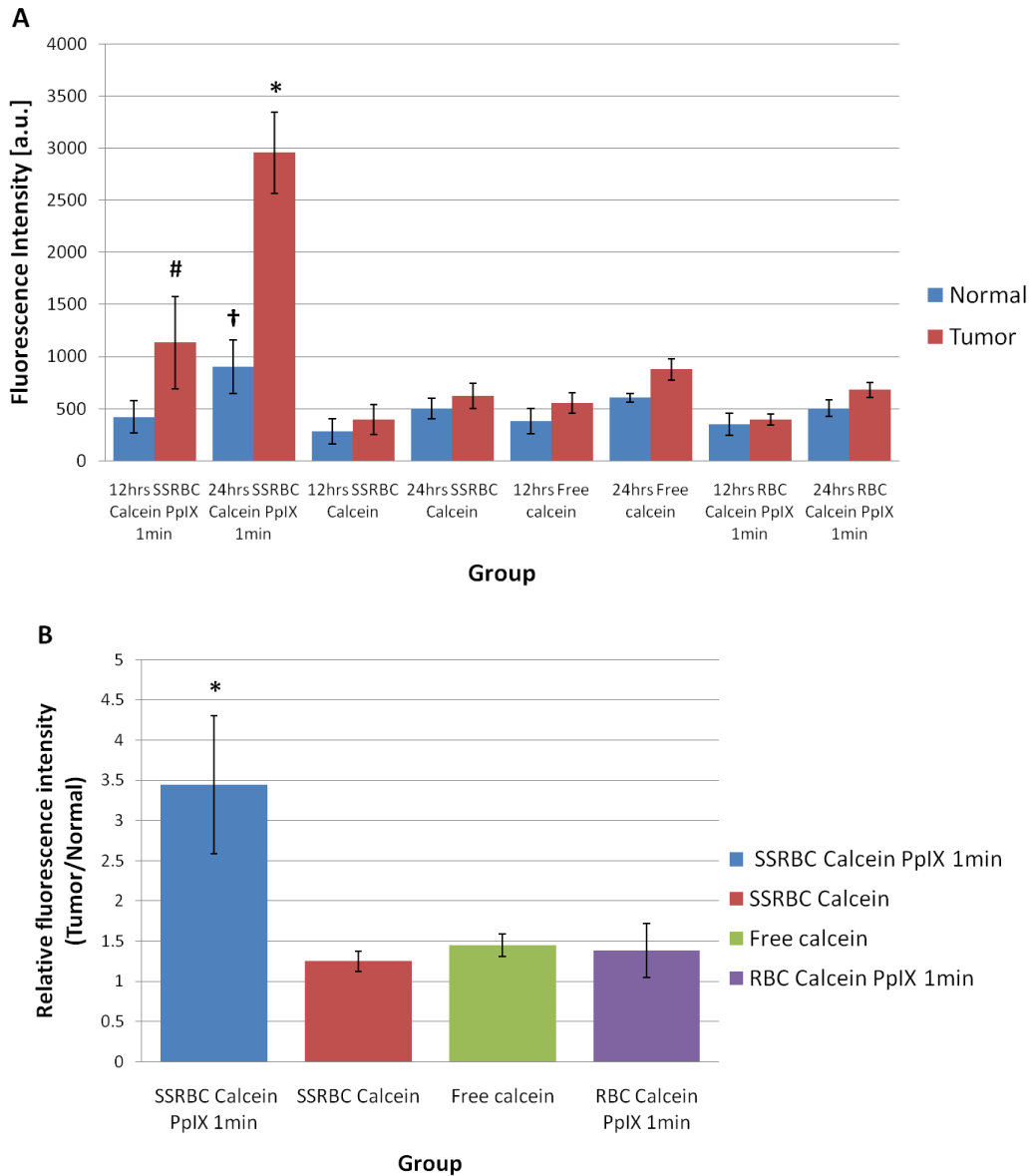


Figure 5-5. In-vivo fluorescence signal measurement through systemic administration of prepared blood sample groups, such as Free calcein, RBC calcein PpIX 1min, SSRBC calcein, and SSRBC calcein PpIX 1min to tumor bearing mouse model. (A) Fluorescence signal from the dialysate in each group were determined at 12 hrs and 24hrs post-administration. Fluorescence signal from SSRBC calcein PpIX 1min group 24hrs post-administration in tumor (*) and normal sites (†) is significantly different ($p < 0.05$) from the other groups collected at 24hrs post-administration. Fluorescence signal from SSRBC calcein PpIX 1min group 12hrs post-administration in tumor site (#) is significantly different ($p < 0.05$) from the other groups collected at 12hrs post-administration. (B) Relative fluorescence intensities were determined at 24hrs post-administration. * Relative fluorescence intensity from SSRBC calcein PpIX 1min group is significantly different from the other groups ($p < 0.05$).

Discussion

Cytotoxic chemotherapy is limited by systemic toxicity. The possible scenario to improve the therapeutic index is development of tumor specific targeting drug carriers and controlled release of drug from carriers. In the present work, SSRBCs from Knock-in SCD mouse model was employed as a new drug carriers and its natural tumor targeting under unique environment of tumor sites using mouse model was evaluated from previous experiment. According to the results, the minimum required time to observe the accumulation of SSRBCs in the tumor sites was empirically determined at about 12hrs ~24 hrs. Using this finding, temporally controlled release of the entrapped fluorescent dye (calcein) from resealed SSRBCs was attempted using the DPH technique.

Drug release by photodynamic activation using photosensitizer could provide rapid and predefined release. However, it is one of conventionally used techniques for topical photodynamic therapy for the treatment of skin cancer and it is only available for identified and accessible tumor sites, not for randomly distributed solid tumors due to difficulties identifying and irradiating multiple tumor sites in disseminated locations that may be inaccessible [8, 203]. Therefore, the possibility of ex vivo activation for in vivo drug release at disseminated tumors with tumor specific targeting maybe enabled with the technique in the project.

Flynn et al. demonstrated the directly photo-dependent release of entrapped thrombolytic agent brinase from photosensitized RBCs by exposure of radiation from a 10mW HeNe laser above the sample [97]. In addition, DPH of photoactivated RBCs was more precisely analyzed by Al-Akhras et al. [99]. Adapting techniques in the previously reported studies, in this project the combined techniques were used to manipulate

SSRBCs with in-vitro DPH experiments. Temporally controlled t_{50} was observed by combined effects such as photochemical and thermal reactions.

The efficiency of our SSRBCs drug carrier model was evaluated by in-vivo DPH experiment. As shown in data in Fig. 5-5, concentration of released calcein from photoactivated SSRBCs in tumor sites were significantly higher than other groups. In addition, the large difference of fluorescence signal from released calcein was observed between the measurements at 12 hrs and 24 hrs post-administration. These results pointed out two most important facts that SSRBCs from Knock-in mouse were preferentially accumulated in target tissues around desired time point and temporally controlled to release entrapped calcein from SSRBCs. Since photohemolysis was temporally programmed to disrupt SSRBCs, relatively higher fluorescence signal was observed in normal sites from photoactivated SSRBCs than the other groups at 12 hrs post-administration. Photochemically inactivated SSRBCs and activated RBCs carriers showed moderate release of calcein or even less than free calcein group at tumor and normal sites. Intact SSRBCs due to inactivated photohemolysis demonstrated less fluorescence signals than activated SSRBCs group. Photoactivated RBCs group demonstrated less signal intensity compared with that of SSRBCs because normal RBCs were not affected by tumor environment and therefore did not preferentially accumulate in the tumors. In addition, they were not significantly different from free calcein. Therefore, the highest relative fluorescence intensity was calculated in photoactivated SSRBCs group. The experiments in this chapter demonstrate that in-vitro DPH based drug release technique from photoactivated SSRBCs can be adapted to in-vivo mouse model and effectively shows the temporally controlled release of

entrapped calcein from SSRBCs in tumor locations. This results suggest that similar results may be obtained for chemotherapeutic agents.

CHAPTER 6 CONCLUSIONS AND FUTURE WORKS

Summary and Conclusion

Conventional cytotoxic chemotherapy for cancer treatment has limited therapeutic efficacy. Despite remarkable progress in development of chemotherapeutic agents and numerous drug delivery systems, major challenges such as inadequate concentration of therapeutic agents in tumor sites and systemic toxicity in healthy normal tissues remain. To overcome the limitations, advanced strategy for tumor targeting and controlled drug release method is necessary. In this dissertation, the potential of sickle red blood cells (SSRBCs) as a novel drug carrier with tumor targeting and temporally controlled drug release characteristics was investigated.

SSRBCs obtained from Knock-in sickle cell disease (SCD) mouse model had more enhanced accumulation to endothelial cells in tumor microvasculature than Berkeley mouse model, one of the most popularly used transgenic mouse model for SCD research, using our hyperspectral imaging system. This finding suggests an appropriate transgenic SCD mouse model with prolonged lifespan that enables researchers developing therapeutic agents for human patients with SCD and with advanced stage of solid tumors to investigate vaso-occlusive crisis and natural tumor targeting. However, the mechanisms responsible for more enhanced accumulation by Knock-in mouse than Berkeley mouse are not yet known and further investigation is necessary. The hyperspectral imaging system provides direct information regarding morphological changes of tumor microvasculature, functional alteration of hemoglobin saturation while tumor mass grows, and quantitative measurements for localized SSRBCs in tumor and normal sites.

Modified hypotonic swelling method was applied to load SSRBCs with calcein and resulted in high entrapping efficacy (85.46%). Temporally controlled release of calcein from resealed SSRBCs was achieved by Delayed photohemolysis (DPH) method. This technique has been employed throughout in-vitro and in-vivo experiments and demonstrates suitable calcein release in a controlled manner. Gompertz based fitting model was used for analysis of empirical and theoretical DPH trials. 4T1 tumor bearing mouse models were prepared to observe the calcein release rate from SSRBCs in tumor sites and significantly elevated fluorescence signals compared with similarly treated normal RBCs with photoactivation and SSRBCs without photoactivation were detected by microplate spectrophotometer.

Light activated SSRBCs has a potential to be used as a novel drug carrier with natural tumor targeting and temporally controlled release characteristics. It is not only an alternative drug delivery system by itself, but also it enables to develop new drug carriers using mechanobiological mimicry of SSRBCs to cure human patient with advanced stage of cancer.

Future Works

In this research, only the absorbance from the released Hb was determined through in-vitro DPH experiment. However, the released calcein volume based on DPH may or may not show similar pattern as Hb according to different molecular weight. The determination of released calcein concentration from the resealed SSRBCs needs to be characterized with that of Hb simultaneously through in vitro DPH.

Conventional chemotherapeutic agents (i.e. doxorubicin or equivalent therapeutic agents) could be employed to replicate the in-vivo experiment so that tumor size in terms of apparent tumor area can be monitored to evaluate its efficacy. Histological

analysis by specialists in tumors, normal tissues and organs typically damaged by SCD are required to evaluate its systemic toxicity.

Further investigation involving accurate concentration measurement using quantitative techniques like high performance liquid chromatography (HPLC) is necessary.

LIST OF REFERENCES

- [1] K. K. Jain, "Drug delivery systems - an overview," *Methods Mol Biol*, vol. 437, pp. 1-50, 2008.
- [2] L. H. Reddy, "Drug delivery to tumours: recent strategies," *J Pharm Pharmacol*, vol. 57, pp. 1231-42, Oct 2005.
- [3] V. P. Torchilin, "Passive and active drug targeting: drug delivery to tumors as an example," *Handb Exp Pharmacol*, pp. 3-53, 2010.
- [4] Y. H. Bae, "Drug targeting and tumor heterogeneity," *J Control Release*, vol. 133, pp. 2-3, Jan 5 2009.
- [5] T. Jones and N. Saba, "Nanotechnology and Drug Delivery: An Update in Oncology," *Pharmaceutics*, vol. 3, pp. 171-185, 2011.
- [6] B. Haley and E. Frenkel, "Nanoparticles for drug delivery in cancer treatment," *Urol Oncol*, vol. 26, pp. 57-64, Jan-Feb 2008.
- [7] A. Sharma and U. S. Sharma, "Liposomes in drug delivery: Progress and limitations," *International Journal of Pharmaceutics*, vol. 154, pp. 123-140, 1997.
- [8] T. L. Andresen, S. S. Jensen, and K. Jorgensen, "Advanced strategies in liposomal cancer therapy: problems and prospects of active and tumor specific drug release," *Prog Lipid Res*, vol. 44, pp. 68-97, Jan 2005.
- [9] G. Gregoriadis, "Engineering liposomes for drug delivery: progress and problems," *Trends Biotechnol*, vol. 13, pp. 527-37, Dec 1995.
- [10] Y. Matsumura and H. Maeda, "A new concept for macromolecular therapeutics in cancer chemotherapy: mechanism of tumoritropic accumulation of proteins and the antitumor agent smancs," *Cancer Res*, vol. 46, pp. 6387-92, Dec 1986.
- [11] S. H. Jang, M. G. Wientjes, D. Lu, and J. L. Au, "Drug delivery and transport to solid tumors," *Pharm Res*, vol. 20, pp. 1337-50, Sep 2003.
- [12] J. Folkman, "Angiogenesis in cancer, vascular, rheumatoid and other disease," *Nat Med*, vol. 1, pp. 27-31, Jan 1995.
- [13] S. A. Skinner, P. J. Tutton, and P. E. O'Brien, "Microvascular architecture of experimental colon tumors in the rat," *Cancer Res*, vol. 50, pp. 2411-7, Apr 15 1990.
- [14] E. Ruoslahti, "Specialization of tumour vasculature," *Nat Rev Cancer*, vol. 2, pp. 83-90, Feb 2002.

- [15] S. K. Hobbs, W. L. Monsky, F. Yuan, W. G. Roberts, L. Griffith, V. P. Torchilin, and R. K. Jain, "Regulation of transport pathways in tumor vessels: role of tumor type and microenvironment," *Proc Natl Acad Sci U S A*, vol. 95, pp. 4607-12, Apr 14 1998.
- [16] F. Yuan, H. A. Salehi, Y. Boucher, U. S. Vasthare, R. F. Tuma, and R. K. Jain, "Vascular permeability and microcirculation of gliomas and mammary carcinomas transplanted in rat and mouse cranial windows," *Cancer Res*, vol. 54, pp. 4564-8, Sep 1 1994.
- [17] F. Yuan, M. Leunig, S. K. Huang, D. A. Berk, D. Papahadjopoulos, and R. K. Jain, "Microvascular permeability and interstitial penetration of sterically stabilized (stealth) liposomes in a human tumor xenograft," *Cancer Res*, vol. 54, pp. 3352-6, Jul 1 1994.
- [18] M. Bundgaard, "Transport pathways in capillaries--in search of pores," *Annu Rev Physiol*, vol. 42, pp. 325-36, 1980.
- [19] N. Simionescu, M. Simionescu, and G. E. Palade, "Open junctions in the endothelium of the postcapillary venules of the diaphragm," *J Cell Biol*, vol. 79, pp. 27-44, Oct 1978.
- [20] L. W. Seymour, "Passive tumor targeting of soluble macromolecules and drug conjugates," *Crit Rev Ther Drug Carrier Syst*, vol. 9, pp. 135-87, 1992.
- [21] K. Iwai, H. Maeda, and T. Konno, "Use of oily contrast medium for selective drug targeting to tumor: enhanced therapeutic effect and X-ray image," *Cancer Res*, vol. 44, pp. 2115-21, May 1984.
- [22] M. Suzuki, K. Hori, I. Abe, S. Saito, and H. Sato, "A new approach to cancer chemotherapy: selective enhancement of tumor blood flow with angiotensin II," *J Natl Cancer Inst*, vol. 67, pp. 663-9, Sep 1981.
- [23] H. Maeda and Y. Matsumura, "Tumoritropic and lymphotropic principles of macromolecular drugs," *Crit Rev Ther Drug Carrier Syst*, vol. 6, pp. 193-210, 1989.
- [24] H. Maeda, G. Y. Bharate, and J. Daruwalla, "Polymeric drugs for efficient tumor-targeted drug delivery based on EPR-effect," *Eur J Pharm Biopharm*, vol. 71, pp. 409-19, Mar 2009.
- [25] W. G. Roberts and G. E. Palade, "Increased microvascular permeability and endothelial fenestration induced by vascular endothelial growth factor," *J Cell Sci*, vol. 108 (Pt 6), pp. 2369-79, Jun 1995.

- [26] D. R. Senger, L. Van de Water, L. F. Brown, J. A. Nagy, K. T. Yeo, T. K. Yeo, B. Berse, R. W. Jackman, A. M. Dvorak, and H. F. Dvorak, "Vascular permeability factor (VPF, VEGF) in tumor biology," *Cancer Metastasis Rev*, vol. 12, pp. 303-24, Sep 1993.
- [27] M. Dellian, B. P. Witwer, H. A. Salehi, F. Yuan, and R. K. Jain, "Quantitation and physiological characterization of angiogenic vessels in mice: effect of basic fibroblast growth factor, vascular endothelial growth factor/vascular permeability factor, and host microenvironment," *Am J Pathol*, vol. 149, pp. 59-71, Jul 1996.
- [28] H. Maeda, Y. Matsumura, and H. Kato, "Purification and identification of [hydroxypropyl³]bradykinin in ascitic fluid from a patient with gastric cancer," *J Biol Chem*, vol. 263, pp. 16051-4, Nov 5 1988.
- [29] A. K. Iyer, G. Khaled, J. Fang, and H. Maeda, "Exploiting the enhanced permeability and retention effect for tumor targeting," *Drug Discov Today*, vol. 11, pp. 812-8, Sep 2006.
- [30] A. K. Iyer, K. Greish, T. Seki, S. Okazaki, J. Fang, K. Takeshita, and H. Maeda, "Polymeric micelles of zinc protoporphyrin for tumor targeted delivery based on EPR effect and singlet oxygen generation," *J Drug Target*, vol. 15, pp. 496-506, Aug-Sep 2007.
- [31] T. Nakanishi, S. Fukushima, K. Okamoto, M. Suzuki, Y. Matsumura, M. Yokoyama, T. Okano, Y. Sakurai, and K. Kataoka, "Development of the polymer micelle carrier system for doxorubicin," *J Control Release*, vol. 74, pp. 295-302, Jul 6 2001.
- [32] W. Junping, K. Takayama, T. Nagai, and Y. Maitani, "Pharmacokinetics and antitumor effects of vincristine carried by microemulsions composed of PEG-lipid, oleic acid, vitamin E and cholesterol," *Int J Pharm*, vol. 251, pp. 13-21, Jan 30 2003.
- [33] V. P. Torchilin, "Recent advances with liposomes as pharmaceutical carriers," *Nat Rev Drug Discov*, vol. 4, pp. 145-60, Feb 2005.
- [34] M. Hamidi, A. Zarrin, M. Foroozesh, and S. Mohammadi-Samani, "Applications of carrier erythrocytes in delivery of biopharmaceuticals," *J Control Release*, vol. 118, pp. 145-60, Apr 2 2007.
- [35] V. R. Muzykantov, "Drug delivery by red blood cells: vascular carriers designed by mother nature," *Expert Opin Drug Deliv*, vol. 7, pp. 403-27, Apr 2010.
- [36] M. Tattersall and S. Clarke, "Developments in drug delivery: implications for cancer care," *Curr Opin Oncol*, vol. 15, pp. 293-9, Jul 2003.

- [37] Q. Chen, S. Tong, M. W. Dewhurst, and F. Yuan, "Targeting tumor microvessels using doxorubicin encapsulated in a novel thermosensitive liposome," *Mol Cancer Ther*, vol. 3, pp. 1311-7, Oct 2004.
- [38] R. I. Pakunlu, Y. Wang, M. Saad, J. J. Khandare, V. Starovoytov, and T. Minko, "In vitro and in vivo intracellular liposomal delivery of antisense oligonucleotides and anticancer drug," *J Control Release*, vol. 114, pp. 153-62, Aug 28 2006.
- [39] B. S. Coller, K. T. Springer, J. H. Beer, N. Mohandas, L. E. Scudder, K. J. Norton, and S. M. West, "Thromboerythrocytes. In vitro studies of a potential autologous, semi-artificial alternative to platelet transfusions," *J Clin Invest*, vol. 89, pp. 546-55, Feb 1992.
- [40] V. R. Muzykantov, D. V. Sakharov, M. D. Smirnov, G. P. Samokhin, and V. N. Smirnov, "Immunotargeting of erythrocyte-bound streptokinase provides local lysis of a fibrin clot," *Biochim Biophys Acta*, vol. 884, pp. 355-62, Nov 19 1986.
- [41] C. G. Millán, M. L. Marinero, A. Z. Castañeda, and J. M. Lanao, "Drug, enzyme and peptide delivery using erythrocytes as carriers," *J Control Release*, vol. 95, pp. 27-49, Feb 20 2004.
- [42] A. V. Gothoskar, "Resealed Erythrocytes: A Review," *Pharmaceutical Technology*, vol. 28, pp. 140-154, 2004.
- [43] R. Ktavtsoff, I. Desbois, C. Doinel, P. Colombat, J. P. Lamagnere, M. Chassaigne, and C. Ropars, "Immunological response to L-asparaginase loaded into red blood cells," *Adv Exp Med Biol*, vol. 326, pp. 175-82, 1992.
- [44] M. Tonetti, B. Astroff, W. Satterfield, A. De Flora, U. Benatti, and J. R. DeLoach, "Construction and characterization of adriamycin-loaded canine red blood cells as a potential slow delivery system," *Biotechnol Appl Biochem*, vol. 12, pp. 621-9, Dec 1990.
- [45] L. Rossi, S. Serafini, L. Cenerini, F. Picardi, L. Bigi, I. Panzani, and M. Magnani, "Erythrocyte-mediated delivery of dexamethasone in patients with chronic obstructive pulmonary disease," *Biotechnol Appl Biochem*, vol. 33, pp. 85-9, Apr 2001.
- [46] G. Gardos, "[Accumulation of potassium ions by human blood corpuscles]," *Acta Physiol Hung*, vol. 6, pp. 191-9, 1954.
- [47] G. M. Ihler, R. H. Glew, and F. W. Schnure, "Enzyme loading of erythrocytes," *Proc Natl Acad Sci U S A*, vol. 70, pp. 2663-6, Sep 1973.
- [48] M. Magnani, L. Rossi, M. D'Ascenzo, I. Panzani, L. Bigi, and A. Zanella, "Erythrocyte engineering for drug delivery and targeting," *Biotechnol Appl Biochem*, vol. 28 (Pt 1), pp. 1-6, Aug 1998.

- [49] P. R. Mishra and N. K. Jain, "Biotinylated methotrexate loaded erythrocytes for enhanced liver uptake. 'A study on the rat'," *Int J Pharm*, vol. 231, pp. 145-53, Jan 14 2002.
- [50] R. Kravtsoff, C. Ropars, M. Laguerre, J. P. Muh, and M. Chassaingne, "Erythrocytes as carriers for L-asparaginase. Methodological and mouse in-vivo studies," *J Pharm Pharmacol*, vol. 42, pp. 473-6, Jul 1990.
- [51] M. Hamidi, H. Tajerzadeh, A. R. Dehpour, and S. Ejtemaee-Mehr, "Inhibition of serum angiotensin-converting enzyme in rabbits after intravenous administration of enalaprilat-loaded intact erythrocytes," *J Pharm Pharmacol*, vol. 53, pp. 1281-6, Sep 2001.
- [52] M. Tonetti, A. B. Astroff, W. Satterfield, A. De Flora, U. Benatti, and J. R. DeLoach, "Pharmacokinetic properties of doxorubicin encapsulated in glutaraldehyde-treated canine erythrocytes," *Am J Vet Res*, vol. 52, pp. 1630-5, Oct 1991.
- [53] L. A. Lotero, G. Olmos, and J. C. Diez, "Delivery to macrophages and toxic action of etoposide carried in mouse red blood cells," *Biochimica et Biophysica Acta (BBA) - General Subjects*, vol. 1620, pp. 160-166, 2003.
- [54] N. Talwar and N. K. Jain, "Erythrocytes as carriers of primaquine-preparation: characterization and evaluation," *Journal of Controlled Release*, vol. 20, pp. 133-141, 1992.
- [55] H. G. Eichler, W. Rafflesberg, S. Gasic, A. Korn, and K. Bauer, "Release of vitamin B12 from carrier erythrocytes in vitro," *Res Exp Med (Berl)*, vol. 185, pp. 341-4, 1985.
- [56] V. Annese, A. Latiano, L. Rossi, G. Lombardi, B. Dallapiccola, S. Serafini, G. Damonte, A. Andriulli, and M. Magnani, "Erythrocytes-mediated delivery of dexamethasone in steroid-dependent IBD patients-a pilot uncontrolled study," *Am J Gastroenterol*, vol. 100, pp. 1370-5, Jun 2005.
- [57] B. Deuticke, M. Kim, and C. Zöllner, "The influence of amphotericin B on the permeability of mammalian erythrocytes to nonelectrolytes, anions and cations," *Biochimica et Biophysica Acta (BBA) - Biomembranes*, vol. 318, pp. 345-359, 1973.
- [58] M. Hamidi, H. Tajerzadeh, A. R. Dehpour, M. R. Rouini, and S. Ejtemaee-Mehr, "In vitro characterization of human intact erythrocytes loaded by enalaprilat," *Drug Deliv*, vol. 8, pp. 223-30, Oct-Dec 2001.
- [59] R. Green, J. Miller, and W. Crosby, "Enhancement of iron chelation by desferrioxamine entrapped in red blood cell ghosts," *Blood*, vol. 57, pp. 866-72, May 1981.

- [60] N. Talwar and N. K. Jain, "Erythrocyte based delivery system of primaquine: in vitro characterization," *J Microencapsul*, vol. 9, pp. 357-64, Jul-Sep 1992.
- [61] J. Deloach and G. Ihler, "A dialysis procedure for loading erythrocytes with enzymes and lipids," *Biochim Biophys Acta*, vol. 496, pp. 136-45, Jan 24 1977.
- [62] P. D. Patel, N. Dand, R. S. Hirlekar, and V. J. Kadam, "Drug loaded erythrocytes: as novel drug delivery system," *Curr Pharm Des*, vol. 14, pp. 63-70, 2008.
- [63] V. S. Gopal, A. Ranjith Kumar, A. N. Usha, A. Karthik, and N. Udupa, "Effective drug targeting by Erythrocytes as Carrier Systems," *Current Trends in Biotechnology and Pharmacy*, vol. 1, pp. 18-33, 2007.
- [64] G. M. Ihler and H. C. Tsang, "Hypotonic hemolysis methods for entrapment of agents in resealed erythrocytes," *Methods Enzymol*, vol. 149, pp. 221-9, 1987.
- [65] E. Pitt, C. M. Johnson, D. A. Lewis, D. A. Jenner, and R. E. Offord, "Encapsulation of drugs in intact erythrocytes: an intravenous delivery system," *Biochem Pharmacol*, vol. 32, pp. 3359-68, Nov 15 1983.
- [66] M. Hamidi and H. Tajerzadeh, "Carrier erythrocytes: an overview," *Drug Deliv*, vol. 10, pp. 9-20, Jan-Mar 2003.
- [67] J. Xiao and J. Liu, "Thermo-fluidic devices and materials inspired from mass and energy transport phenomena in biological system," *Frontiers of Energy and Power Engineering in China*, vol. 3, pp. 47-59, 2009.
- [68] S. Jain, "Engineered erythrocytes as a drug delivery system," *Indian journal of pharmaceutical sciences*, vol. 59, p. 275, 1997.
- [69] W. N. Field, M. D. Gamble, and D. A. Lewis, "A comparison of the treatment of thyroidectomized rats with free thyroxine and thyroxine encapsulated in erythrocytes," *International Journal of Pharmaceutics*, vol. 51, pp. 175-178, 1989.
- [70] M. M. Heeney and R. E. Ware, "Hydroxyurea for children with sickle cell disease," *Hematol Oncol Clin North Am*, vol. 24, pp. 199-214, Feb 2010.
- [71] M. Elagouz, S. Jyothi, B. Gupta, and S. Sivaprasad, "Sickle cell disease and the eye: old and new concepts," *Surv Ophthalmol*, vol. 55, pp. 359-77, Jul 8 2010.
- [72] R. M. Bookchin and V. L. Lew, "Pathophysiology of sickle cell anemia," *Hematol Oncol Clin North Am*, vol. 10, pp. 1241-53, Dec 1996.
- [73] W. N. Poillon, B. C. Kim, and O. Castro, "Intracellular hemoglobin S polymerization and the clinical severity of sickle cell anemia," *Blood*, vol. 91, pp. 1777-83, Mar 1 1998.

- [74] J. Chang, P. A. Shi, E. Y. Chiang, and P. S. Frenette, "Intravenous immunoglobulins reverse acute vaso-occlusive crises in sickle cell mice through rapid inhibition of neutrophil adhesion," *Blood*, vol. 111, pp. 915-23, Jan 15 2008.
- [75] L. A. Verduzco and D. G. Nathan, "Sickle cell disease and stroke," *Blood*, vol. 114, pp. 5117-25, Dec 10 2009.
- [76] H. Hiruma, C. T. Noguchi, N. Uyesaka, S. Hasegawa, E. J. Blanchetmackie, A. N. Schechter, and G. P. Rodgers, "Sickle-Cell Rheology Is Determined by Polymer Fraction - Not Cell Morphology," *American Journal of Hematology*, vol. 48, pp. 19-28, Jan 1995.
- [77] D. K. Kaul, E. Finnegan, and G. A. Barabino, "Sickle red cell-endothelium interactions," *Microcirculation*, vol. 16, pp. 97-111, Jan 2009.
- [78] N. Conran and F. F. Costa, "Hemoglobin disorders and endothelial cell interactions," *Clin Biochem*, vol. 42, pp. 1824-38, Dec 2009.
- [79] S. K. Ballas and N. Mohandas, "Sickle red cell microrheology and sickle blood rheology," *Microcirculation*, vol. 11, pp. 209-25, Mar 2004.
- [80] S. K. Bains, R. Foresti, J. Howard, S. Atwal, C. J. Green, and R. Moteerlini, "Human sickle cell blood modulates endothelial heme oxygenase activity," *Arteriosclerosis, Thrombosis, and Vascular Biology*, vol. 30, pp. 305-312, 2010.
- [81] G. A. Barabino, M. O. Platt, and D. K. Kaul, "Sickle cell biomechanics," *Annu Rev Biomed Eng*, vol. 12, pp. 345-67, Aug 15 2010.
- [82] M. W. Dewhirst, "Concepts of oxygen transport at the microcirculatory level," *Semin Radiat Oncol*, vol. 8, pp. 143-50, Jul 1998.
- [83] C. J. Gullledge and M. W. Dewhirst, "Tumor oxygenation: a matter of supply and demand," *Anticancer Res*, vol. 16, pp. 741-9, Mar-Apr 1996.
- [84] I. F. Tannock and D. Rotin, "Acid pH in tumors and its potential for therapeutic exploitation," *Cancer Res*, vol. 49, pp. 4373-84, Aug 15 1989.
- [85] M. J. Telen, "Role of adhesion molecules and vascular endothelium in the pathogenesis of sickle cell disease," *Hematology Am Soc Hematol Educ Program*, pp. 84-90, 2007.
- [86] R. Zennadi, B. J. Moeller, E. J. Whalen, M. Batchvarova, K. Xu, S. Shan, M. Delahunty, M. W. Dewhirst, and M. J. Telen, "Epinephrine-induced activation of LW-mediated sickle cell adhesion and vaso-occlusion in vivo," *Blood*, vol. 110, pp. 2708-17, Oct 1 2007.

- [87] R. Zennadi, P. C. Hines, L. M. De Castro, J. P. Cartron, L. V. Parise, and M. J. Telen, "Epinephrine acts through erythroid signaling pathways to activate sickle cell adhesion to endothelium via LW-alphaVbeta3 interactions," *Blood*, vol. 104, pp. 3774-81, Dec 1 2004.
- [88] D. K. Kaul, X. D. Liu, X. Zhang, T. Mankelow, S. Parsons, F. Spring, X. An, N. Mohandas, D. Anstee, and J. A. Chasis, "Peptides based on alphaV-binding domains of erythrocyte ICAM-4 inhibit sickle red cell-endothelial interactions and vaso-occlusion in the microcirculation," *Am J Physiol Cell Physiol*, vol. 291, pp. C922-30, Nov 2006.
- [89] W. Arap, R. Pasqualini, and E. Ruoslahti, "Cancer treatment by targeted drug delivery to tumor vasculature in a mouse model," *Science*, vol. 279, pp. 377-80, Jan 16 1998.
- [90] S. L. Brown, J. R. Ewing, T. N. Nagaraja, P. S. Swerdlow, Y. Cao, J. D. Fenstermacher, and J. H. Kim, "Sickle red blood cells accumulate in tumor," *Magn Reson Med*, vol. 50, pp. 1209-14, Dec 2003.
- [91] M. Milosevic, I. Quirt, W. Levin, A. Fyles, L. Manchul, and W. Chapman, "Intratumoral sickling in a patient with cervix cancer and sickle trait: effect on blood flow and oxygenation," *Gynecol Oncol*, vol. 83, pp. 428-31, Nov 2001.
- [92] M. H. Steinberg, "Management of sickle cell disease," *N Engl J Med*, vol. 340, pp. 1021-30, Apr 1 1999.
- [93] J. Cui, C. Li, W. Guo, Y. Li, C. Wang, L. Zhang, Y. Hao, and Y. Wang, "Direct comparison of two pegylated liposomal doxorubicin formulations: is AUC predictive for toxicity and efficacy?," *J Control Release*, vol. 118, pp. 204-15, Apr 2 2007.
- [94] R. J. Price, D. M. Skyba, S. Kaul, and T. C. Skalak, "Delivery of colloidal particles and red blood cells to tissue through microvessel ruptures created by targeted microbubble destruction with ultrasound," *Circulation*, vol. 98, pp. 1264-7, Sep 29 1998.
- [95] G. Flynn, L. McHale, and A. P. McHale, "Methotrexate-loaded, photosensitized erythrocytes: a photo-activatable carrier/delivery system for use in cancer therapy," *Cancer Lett*, vol. 82, pp. 225-9, Jul 29 1994.
- [96] A. Rollan and A. P. McHale, "Differential response of photosensitized young and old human erythrocytes to photodynamic activation," *Cancer Lett*, vol. 111, pp. 207-13, Jan 1 1997.
- [97] G. Flynn, T. J. Hackett, L. McHale, and A. P. McHale, "Encapsulation of the thrombolytic enzyme, brinase, in photosensitized erythrocytes: a novel thrombolytic system based on photodynamic activation," *J Photochem Photobiol B*, vol. 26, pp. 193-6, Nov 1994.

- [98] U. Zimmerman, "Cellular drug-carrier systems and their possible targeting," in *Targeted Drugs*, E. P. Goldberg, Ed., ed New York: Wiley, 1983, pp. 153-200.
- [99] M. A. al-Akhras and L. I. Grossweiner, "Sensitization of photohemolysis by hypericin and Photofrin," *J Photochem Photobiol B*, vol. 34, pp. 169-75, Jul 1996.
- [100] L. I. Grossweiner, J. M. Fernandez, and M. D. Bilgin, "Photosensitisation of red blood cell haemolysis by photodynamic agents," *Lasers in Medical Science*, vol. 13, pp. 42-54, 1998.
- [101] M. Al-Akhras, "A new application of Gompertz function in photohemolysis: the effect of temperature on red blood cell hemolysis photosensitized by protoporphyrin IX," *Med Biol Eng Comput*, vol. 44, pp. 703-10, Aug 2006.
- [102] B. Gompertz, "On the Nature of the Function Expressive of the Law of Human Mortality, and on a New Mode of Determining the Value of Life Contingencies," *Philosophical Transactions of the Royal Society of London*, vol. 115, pp. 513-583, 1825.
- [103] P. Nandi and S. M. Lunte, "Recent trends in microdialysis sampling integrated with conventional and microanalytical systems for monitoring biological events: a review," *Anal Chim Acta*, vol. 651, pp. 1-14, Sep 28 2009.
- [104] N. Plock and C. Kloft, "Microdialysis--theoretical background and recent implementation in applied life-sciences," *Eur J Pharm Sci*, vol. 25, pp. 1-24, May 2005.
- [105] J. M. Delgado, F. V. DeFeudis, R. H. Roth, D. K. Ryugo, and B. M. Mitruka, "Dialytrode for long term intracerebral perfusion in awake monkeys," *Arch Int Pharmacodyn Ther*, vol. 198, pp. 9-21, 1972.
- [106] H. J. Holovics, C. R. Anderson, B. S. Levine, H. W. Hui, and C. E. Lunte, "Investigation of drug delivery by iontophoresis in a surgical wound utilizing microdialysis," *Pharm Res*, vol. 25, pp. 1762-70, Aug 2008.
- [107] A. Kim, L. A. Suecof, C. A. Sutherland, L. Gao, J. L. Kuti, and D. P. Nicolau, "In vivo microdialysis study of the penetration of daptomycin into soft tissues in diabetic versus healthy volunteers," *Antimicrob Agents Chemother*, vol. 52, pp. 3941-6, Nov 2008.
- [108] K. Lanckmans, R. Clinckers, A. Van Eeckhaut, S. Sarre, I. Smolders, and Y. Michotte, "Use of microbore LC-MS/MS for the quantification of oxcarbazepine and its active metabolite in rat brain microdialysis samples," *J Chromatogr B Analyt Technol Biomed Life Sci*, vol. 831, pp. 205-12, Feb 2 2006.
- [109] S. Bielecka-Grzela and A. Klimowicz, "Application of cutaneous microdialysis to evaluate metronidazole and its main metabolite concentrations in the skin after a single oral dose," *J Clin Pharm Ther*, vol. 28, pp. 465-9, Dec 2003.

- [110] D. A. Richards, M. A. Silva, N. Murphy, S. J. Wigmore, and D. F. Mirza, "Extracellular amino acid levels in the human liver during transplantation: a microdialysis study from donor to recipient," *Amino Acids*, vol. 33, pp. 429-37, Sep 2007.
- [111] K. E. Price, S. S. Vandaveer, C. E. Lunte, and C. K. Larive, "Tissue targeted metabolomics: metabolic profiling by microdialysis sampling and microcoil NMR," *J Pharm Biomed Anal*, vol. 38, pp. 904-9, Aug 10 2005.
- [112] H. Huang, Y. Zhang, R. Yang, and X. Tang, "Determination of baicalin in rat cerebrospinal fluid and blood using microdialysis coupled with ultra-performance liquid chromatography-tandem mass spectrometry," *J Chromatogr B Analyt Technol Biomed Life Sci*, vol. 874, pp. 77-83, Oct 15 2008.
- [113] K. W. Ward and G. M. Pollack, "Use of intrauterine microdialysis to investigate methanol-induced alterations in uteroplacental blood flow," *Toxicol Appl Pharmacol*, vol. 140, pp. 203-10, Oct 1996.
- [114] K. L. Woo and C. E. Lunte, "The direct comparison of health and ulcerated stomach tissue: a multiple probe microdialysis sampling approach," *J Pharm Biomed Anal*, vol. 48, pp. 85-91, Sep 10 2008.
- [115] T. Zhu, B. W. Cheung, L. L. Cartier, G. S. Giebink, and R. J. Sawchuk, "Simultaneous intravenous and intramiddle-ear dosing to determine cefditoren influx and efflux clearances in middle ear fluid in freely moving chinchillas," *J Pharm Sci*, vol. 92, pp. 1947-56, Oct 2003.
- [116] C. S. Parkins, M. R. Stratford, M. F. Dennis, M. Stubbs, and D. J. Chaplin, "The relationship between extracellular lactate and tumour pH in a murine tumour model of ischaemia-reperfusion," *Br J Cancer*, vol. 75, pp. 319-23, 1997.
- [117] W. C. Zamboni, P. J. Houghton, J. L. Hulstein, M. Kirstein, J. Walsh, P. J. Cheshire, S. K. Hanna, M. K. Danks, and C. F. Stewart, "Relationship between tumor extracellular fluid exposure to topotecan and tumor response in human neuroblastoma xenograft and cell lines," *Cancer Chemother Pharmacol*, vol. 43, pp. 269-76, 1999.
- [118] R. K. Palsmeier and C. E. Lunte, "Microdialysis sampling in tumor and muscle: study of the disposition of 3-amino-1,2,4-benzotriazine-1,4-di-N-oxide (SR 4233)," *Life Sci*, vol. 55, pp. 815-25, 1994.
- [119] S. N. Sani, K. Henry, M. Bohlke, J. Kim, A. Stricker-Krongrad, and T. J. Maher, "The effects of drug transporter inhibitors on the pharmacokinetics and tissue distribution of methotrexate in normal and tumor-bearing mice: a microdialysis study," *Cancer Chemother Pharmacol*, vol. 66, pp. 159-69, May 2010.
- [120] C. Höcht, J. A. Opezco, and C. A. Taira, "Microdialysis in drug discovery," *Curr Drug Discov Technol*, vol. 1, pp. 269-85, Dec 2004.

- [121] M. J. Stuart and R. L. Nagel, "Sickle-cell disease," *Lancet*, vol. 364, pp. 1343-60, Oct 9-15 2004.
- [122] S. Hak, N. K. Reitan, O. Haraldseth, and C. de Lange Davies, "Intravital microscopy in window chambers: a unique tool to study tumor angiogenesis and delivery of nanoparticles," *Angiogenesis*, vol. 13, pp. 113-30, Jun 2010.
- [123] J. C. Sandison, "A new method for the microscopic study of living growing tissues by the introduction of a transparent chamber in the rabbit's ear," *The Anatomical Record*, vol. 28, pp. 281-287, 1924.
- [124] C. M. Goodall, A. G. Sanders, and P. Shubik, "Studies of vascular patterns in living tumors with a transparent chamber inserted in hamster cheek pouch," *J Natl Cancer Inst*, vol. 35, pp. 497-521, Sep 1965.
- [125] D. Kedrin, B. Gligorijevic, J. Wyckoff, V. V. Verkhusha, J. Condeelis, J. E. Segall, and J. van Rheenen, "Intravital imaging of metastatic behavior through a mammary imaging window," *Nature Methods*, vol. 5, pp. 1019-1021, Dec 2008.
- [126] J. C. Nims and J. W. Irwin, "Chamber techniques to study the microvasculature," *Microvasc Res*, vol. 5, pp. 105-18, Jan 1973.
- [127] R. K. Jain, L. L. Munn, and D. Fukumura, "Dissecting tumour pathophysiology using intravital microscopy," *Nat Rev Cancer*, vol. 2, pp. 266-76, Apr 2002.
- [128] K. E. Arfors, J. A. Jonsson, and F. N. McKenzie, "A titanium rabbit ear chamber: assembly, insertion and results," *Microvasc Res*, vol. 2, pp. 516-8, Oct 1970.
- [129] J. V. Gaustad, K. G. Brurberg, T. G. Simonsen, C. S. Mollatt, and E. K. Rofstad, "Tumor vascularity assessed by magnetic resonance imaging and intravital microscopy imaging," *Neoplasia*, vol. 10, pp. 354-62, Apr 2008.
- [130] F. G. Arthur, L. Yuxiang, and S. Mir Farrokh, "A System for Multi-Modality Optical and MR Imaging of Implanted Window Chambers," 2009, p. NWD4.
- [131] H. D. Papenfuss, J. F. Gross, M. Intaglietta, and F. A. Treese, "A transparent access chamber for the rat dorsal skin fold," *Microvasc Res*, vol. 18, pp. 311-8, Nov 1979.
- [132] C. Dedeugd, M. Wankhede, and B. S. Sorg, "Multimodal optical imaging of microvessel network convective oxygen transport dynamics," *Appl Opt*, vol. 48, pp. D187-97, Apr 1 2009.
- [133] Y. Gazit, D. A. Berk, M. Leunig, L. T. Baxter, and R. K. Jain, "Scale-invariant behavior and vascular network formation in normal and tumor tissue," *Phys Rev Lett*, vol. 75, pp. 2428-2431, Sep 18 1995.

- [134] Y. Izumi, L. Xu, E. di Tomaso, D. Fukumura, and R. K. Jain, "Tumour biology: herceptin acts as an anti-angiogenic cocktail," *Nature*, vol. 416, pp. 279-80, Mar 21 2002.
- [135] R. T. Tong, Y. Boucher, S. V. Kozin, F. Winkler, D. J. Hicklin, and R. K. Jain, "Vascular normalization by vascular endothelial growth factor receptor 2 blockade induces a pressure gradient across the vasculature and improves drug penetration in tumors," *Cancer Res*, vol. 64, pp. 3731-6, Jun 1 2004.
- [136] A. Erikson, I. Tufto, A. B. Bjønnum, O. S. Bruland, and L. Davies Cde, "The impact of enzymatic degradation on the uptake of differently sized therapeutic molecules," *Anticancer Res*, vol. 28, pp. 3557-66, Nov-Dec 2008.
- [137] I. Tufto, R. Hansen, D. Byberg, K. H. Nygaard, J. Tufto, and L. Davies Cde, "The effect of collagenase and hyaluronidase on transient perfusion in human osteosarcoma xenografts grown orthotopically and in dorsal skinfold chambers," *Anticancer Res*, vol. 27, pp. 1475-81, May-Jun 2007.
- [138] G. Helmlinger, F. Yuan, M. Dellian, and R. K. Jain, "Interstitial pH and pO₂ gradients in solid tumors in vivo: high-resolution measurements reveal a lack of correlation," *Nat Med*, vol. 3, pp. 177-82, Feb 1997.
- [139] C. Y. Li, S. Shan, Q. Huang, R. D. Braun, J. Lanzen, K. Hu, P. Lin, and M. W. Dewhirst, "Initial stages of tumor cell-induced angiogenesis: evaluation via skin window chambers in rodent models," *J Natl Cancer Inst*, vol. 92, pp. 143-7, Jan 19 2000.
- [140] D. Fukumura, L. Xu, Y. Chen, T. Gohongi, B. Seed, and R. K. Jain, "Hypoxia and acidosis independently up-regulate vascular endothelial growth factor transcription in brain tumors in vivo," *Cancer Res*, vol. 61, pp. 6020-4, Aug 15 2001.
- [141] G. Alexandrakis, E. B. Brown, R. T. Tong, T. D. McKee, R. B. Campbell, Y. Boucher, and R. K. Jain, "Two-photon fluorescence correlation microscopy reveals the two-phase nature of transport in tumors," *Nat Med*, vol. 10, pp. 203-7, Feb 2004.
- [142] A. L. Seynhaeve, S. Hoving, D. Schipper, C. E. Vermeulen, G. de Wiel-Ambagtsheer, S. T. van Tiel, A. M. Eggermont, and T. L. Ten Hagen, "Tumor necrosis factor alpha mediates homogeneous distribution of liposomes in murine melanoma that contributes to a better tumor response," *Cancer Res*, vol. 67, pp. 9455-62, Oct 1 2007.
- [143] D. M. Brizel, G. S. Sibley, L. R. Prosnitz, R. L. Scher, and M. W. Dewhirst, "Tumor hypoxia adversely affects the prognosis of carcinoma of the head and neck," *Int J Radiat Oncol Biol Phys*, vol. 38, pp. 285-9, May 1 1997.

- [144] M. Nordmark and J. Overgaard, "A confirmatory prognostic study on oxygenation status and loco-regional control in advanced head and neck squamous cell carcinoma treated by radiation therapy," *Radiother Oncol*, vol. 57, pp. 39-43, Oct 2000.
- [145] B. S. Sorg, B. J. Moeller, O. Donovan, Y. Cao, and M. W. Dewhirst, "Hyperspectral imaging of hemoglobin saturation in tumor microvasculature and tumor hypoxia development," *J Biomed Opt*, vol. 10, p. 44004, Jul-Aug 2005.
- [146] R. D. Shonat, E. S. Wachman, W. Niu, A. P. Koretsky, and D. L. Farkas, "Near-simultaneous hemoglobin saturation and oxygen tension maps in mouse brain using an AOTF microscope," *Biophys J*, vol. 73, pp. 1223-31, Sep 1997.
- [147] Y. Garini, I. T. Young, and G. McNamara, "Spectral imaging: principles and applications," *Cytometry A*, vol. 69, pp. 735-47, Aug 1 2006.
- [148] M. L. Hans and A. M. Lowman, "Biodegradable nanoparticles for drug delivery and targeting," *Current Opinion in Solid State and Materials Science*, vol. 6, pp. 319-327, 2002.
- [149] M. Igartua, R. M. Hernandez, A. Esquisabel, A. R. Gascon, M. B. Calvo, and J. L. Pedraz, "Enhanced immune response after subcutaneous and oral immunization with biodegradable PLGA microspheres," *J Control Release*, vol. 56, pp. 63-73, Dec 4 1998.
- [150] W. Jiang, R. K. Gupta, M. C. Deshpande, and S. P. Schwendeman, "Biodegradable poly(lactic-co-glycolic acid) microparticles for injectable delivery of vaccine antigens," *Adv Drug Deliv Rev*, vol. 57, pp. 391-410, Jan 10 2005.
- [151] P. Johansen, Y. Men, H. P. Merkle, and B. Gander, "Revisiting PLA/PLGA microspheres: an analysis of their potential in parenteral vaccination," *Eur J Pharm Biopharm*, vol. 50, pp. 129-46, Jul 2000.
- [152] K. S. Jones, "Effects of biomaterial-induced inflammation on fibrosis and rejection," *Semin Immunol*, vol. 20, pp. 130-6, Apr 2008.
- [153] S. Mochida, T. Matsura, A. Yamashita, S. Horie, S. Ohata, C. Kusumoto, T. Nishida, Y. Minami, Y. Inagaki, Y. Ishibe, J. Nakada, Y. Ohta, and K. Yamada, "Geranylgeranylacetone ameliorates inflammatory response to lipopolysaccharide (LPS) in murine macrophages: inhibition of LPS binding to the cell surface," *J Clin Biochem Nutr*, vol. 41, pp. 115-23, Sep 2007.
- [154] J. Panyam and V. Labhasetwar, "Biodegradable nanoparticles for drug and gene delivery to cells and tissue," *Adv Drug Deliv Rev*, vol. 55, pp. 329-47, Feb 24 2003.

- [155] J. E. Rosas, R. M. Hernandez, A. R. Gascon, M. Igartua, F. Guzman, M. E. Patarroyo, and J. L. Pedraz, "Biodegradable PLGA microspheres as a delivery system for malaria synthetic peptide SPf66," *Vaccine*, vol. 19, pp. 4445-51, Aug 14 2001.
- [156] M. Rucker, M. W. Laschke, D. Junker, C. Carvalho, A. Schramm, R. Mulhaupt, N. C. Gellrich, and M. D. Menger, "Angiogenic and inflammatory response to biodegradable scaffolds in dorsal skinfold chambers of mice," *Biomaterials*, vol. 27, pp. 5027-38, Oct 2006.
- [157] A. P. Acharya, M. J. Clare-Salzler, and B. G. Keselowsky, "A high-throughput microparticle microarray platform for dendritic cell-targeting vaccines," *Biomaterials*, vol. 30, pp. 4168-77, Sep 2009.
- [158] A. P. Acharya, N. V. Dolgova, M. J. Clare-Salzler, and B. G. Keselowsky, "Adhesive substrate-modulation of adaptive immune responses," *Biomaterials*, vol. 29, pp. 4736-50, Dec 2008.
- [159] B. G. Keselowsky, A. W. Bridges, K. L. Burns, C. C. Tate, J. E. Babensee, M. C. LaPlaca, and A. J. Garcia, "Role of plasma fibronectin in the foreign body response to biomaterials," *Biomaterials*, vol. 28, pp. 3626-31, Sep 2007.
- [160] S. P. Shankar, Chen, II, B. G. Keselowsky, A. J. Garcia, and J. E. Babensee, "Profiles of carbohydrate ligands associated with adsorbed proteins on self-assembled monolayers of defined chemistries," *J Biomed Mater Res A*, vol. 92, pp. 1329-42, Mar 15 2010.
- [161] E. Ingham and J. Fisher, "The role of macrophages in osteolysis of total joint replacement," *Biomaterials*, vol. 26, pp. 1271-86, Apr 2005.
- [162] J. B. Park, "Phagocytosis induces superoxide formation and apoptosis in macrophages," *Exp Mol Med*, vol. 35, pp. 325-35, Oct 31 2003.
- [163] C. Sumen, T. R. Mempel, I. B. Mazo, and U. H. von Andrian, "Intravital microscopy: visualizing immunity in context," *Immunity*, vol. 21, pp. 315-29, Sep 2004.
- [164] Y. Tang, P. Borgstrom, J. Maynard, J. Koziol, Z. Hu, A. Garen, and A. Deisseroth, "Mapping of angiogenic markers for targeting of vectors to tumor vascular endothelial cells," *Cancer Gene Ther*, vol. 14, pp. 346-53, Apr 2007.
- [165] B. S. Sorg, M. E. Hardee, N. Agarwal, B. J. Moeller, and M. W. Dewhirst, "Spectral imaging facilitates visualization and measurements of unstable and abnormal microvascular oxygen transport in tumors," *J Biomed Opt*, vol. 13, p. 014026, Jan-Feb 2008.

- [166] M. E. Hardee, M. W. Dewhirst, N. Agarwal, and B. S. Sorg, "Novel imaging provides new insights into mechanisms of oxygen transport in tumors," *Curr Mol Med*, vol. 9, pp. 435-41, May 2009.
- [167] S. Copeland, H. S. Warren, S. F. Lowry, S. E. Calvano, and D. Remick, "Acute inflammatory response to endotoxin in mice and humans," *Clin Diagn Lab Immunol*, vol. 12, pp. 60-7, Jan 2005.
- [168] C. N. Kraft, M. Hansis, S. Arens, M. D. Menger, and B. Vollmar, "Striated muscle microvascular response to silver implants: A comparative in vivo study with titanium and stainless steel," *J Biomed Mater Res*, vol. 49, pp. 192-9, Feb 2000.
- [169] M. J. Burne, F. Daniels, A. El Ghandour, S. Mauiyyedi, R. B. Colvin, M. P. O'Donnell, and H. Rabb, "Identification of the CD4(+) T cell as a major pathogenic factor in ischemic acute renal failure," *J Clin Invest*, vol. 108, pp. 1283-90, Nov 2001.
- [170] E. Lanz, M. Gregor, J. Slavík, and A. Kotyk, "Use of FITC as a Fluorescent Probe for Intracellular pH Measurement," *Journal of Fluorescence*, vol. 7, pp. 317-319, 1997.
- [171] M. S. Kim, H. H. Ahn, Y. N. Shin, M. H. Cho, G. Khang, and H. B. Lee, "An in vivo study of the host tissue response to subcutaneous implantation of PLGA- and/or porcine small intestinal submucosa-based scaffolds," *Biomaterials*, vol. 28, pp. 5137-43, Dec 2007.
- [172] Z. Xia and J. T. Triffitt, "A review on macrophage responses to biomaterials," *Biomed Mater*, vol. 1, pp. R1-9, Mar 2006.
- [173] S. G. Reed, S. Bertholet, R. N. Coler, and M. Friede, "New horizons in adjuvants for vaccine development," *Trends Immunol*, vol. 30, pp. 23-32, Jan 2009.
- [174] J. M. Anderson, A. Rodriguez, and D. T. Chang, "Foreign body reaction to biomaterials," *Semin Immunol*, vol. 20, pp. 86-100, Apr 2008.
- [175] B. D. Ratner, *Biomaterials Science. An introduction to materials in medicine*: San Diego, CA; Academic Press, 1997.
- [176] J. M. Anderson and M. S. Shive, "Biodegradation and biocompatibility of PLA and PLGA microspheres," *Advanced Drug Delivery Reviews*, vol. 28, pp. 5-24, 1997.
- [177] A. Luzardo-Alvarez, N. Blarer, K. Peter, J. F. Romero, C. Reymond, G. Corradin, and B. Gander, "Biodegradable microspheres alone do not stimulate murine macrophages in vitro, but prolong antigen presentation by macrophages in vitro and stimulate a solid immune response in mice," *J Control Release*, vol. 109, pp. 62-76, Dec 5 2005.

- [178] M. Triantafilou and K. Triantafilou, "The dynamics of LPS recognition: complex orchestration of multiple receptors," *J Endotoxin Res*, vol. 11, pp. 5-11, 2005.
- [179] H. W. Hopf and M. D. Rollins, "Wounds: an overview of the role of oxygen," *Antioxid Redox Signal*, vol. 9, pp. 1183-92, Aug 2007.
- [180] L. Bosca, M. Zeini, P. G. Traves, and S. Hortelano, "Nitric oxide and cell viability in inflammatory cells: a role for NO in macrophage function and fate," *Toxicology*, vol. 208, pp. 249-58, Mar 15 2005.
- [181] K. T. Huang, L. Kuo, and J. C. Liao, "Lipopolysaccharide activates endothelial nitric oxide synthase through protein tyrosine kinase," *Biochem Biophys Res Commun*, vol. 245, pp. 33-7, Apr 7 1998.
- [182] J. MacMicking, Q. W. Xie, and C. Nathan, "Nitric oxide and macrophage function," *Annu Rev Immunol*, vol. 15, pp. 323-50, 1997.
- [183] G. C. Brown, "Nitric oxide and mitochondrial respiration," *Biochim Biophys Acta*, vol. 1411, pp. 351-69, May 5 1999.
- [184] G. N. Stamatas and N. Kollias, "In vivo documentation of cutaneous inflammation using spectral imaging," *J Biomed Opt*, vol. 12, p. 051603, Sep-Oct 2007.
- [185] K. Z. Liu, X. M. Xiang, A. Man, M. G. Sowa, A. Cholakis, E. Ghiabi, D. L. Singer, and D. A. Scott, "In vivo determination of multiple indices of periodontal inflammation by optical spectroscopy," *J Periodontal Res*, vol. 44, pp. 117-24, Feb 2009.
- [186] P. Shubik, "Vascularization of tumors: a review," *J Cancer Res Clin Oncol*, vol. 103, pp. 211-26, 1982.
- [187] S. W. Choe, A. P. Acharya, B. G. Keselowsky, and B. S. Sorg, "Intravital microscopy imaging of macrophage localization to immunogenic particles and co-localized tissue oxygen saturation," *Acta Biomater*, vol. 6, pp. 3491-8, Sep 2010.
- [188] C. Paszty, C. M. Brion, E. Mancini, H. E. Witkowska, M. E. Stevens, N. Mohandas, and E. M. Rubin, "Transgenic knockout mice with exclusively human sickle hemoglobin and sickle cell disease," *Science*, vol. 278, pp. 876-8, Oct 31 1997.
- [189] J. Ieremia and C. A. Blau, "Limitations of a mouse model of sickle cell anemia," *Blood Cells Mol Dis*, vol. 28, pp. 146-51, Mar-Apr 2002.
- [190] L. C. Wu, C. W. Sun, T. M. Ryan, K. M. Pawlik, J. Ren, and T. M. Townes, "Correction of sickle cell disease by homologous recombination in embryonic stem cells," *Blood*, vol. 108, pp. 1183-8, Aug 15 2006.

- [191] J. Hanna, M. Wernig, S. Markoulaki, C. W. Sun, A. Meissner, J. P. Cassady, C. Beard, T. Brambrink, L. C. Wu, T. M. Townes, and R. Jaenisch, "Treatment of sickle cell anemia mouse model with iPS cells generated from autologous skin," *Science*, vol. 318, pp. 1920-3, Dec 21 2007.
- [192] M. D. Bilgin, M. A. al Akhras, M. Khalili, H. Hemmati, and L. I. Grossweiner, "Photosensitization of red blood cell hemolysis by lutetium texaphyrin," *Photochem Photobiol*, vol. 72, pp. 121-7, Jul 2000.
- [193] J. L. Unthank, J. M. Lash, J. C. Nixon, R. A. Sidner, and H. G. Bohlen, "Evaluation of carbocyanine-labeled erythrocytes for microvascular measurements," *Microvasc Res*, vol. 45, pp. 193-210, Mar 1993.
- [194] M. R. King, D. Bansal, M. B. Kim, and I. H. Sarelius, "The effect of hematocrit and leukocyte adherence on flow direction in the microcirculation," *Ann Biomed Eng*, vol. 32, pp. 803-14, Jun 2004.
- [195] M. Trudel, M. E. De Paepe, N. Chretien, N. Saadane, J. Jacmain, M. Sorette, T. Hoang, and Y. Beuzard, "Sickle cell disease of transgenic SAD mice," *Blood*, vol. 84, pp. 3189-97, Nov 1 1994.
- [196] P. Bonnin, N. Sabaa, M. Flamant, H. Debbabi, and P. L. Tharaux, "Ultrasound imaging of renal vaso-occlusive events in transgenic sickle mice exposed to hypoxic stress," *Ultrasound Med Biol*, vol. 34, pp. 1076-84, Jul 2008.
- [197] O. S. Platt, "Hydroxyurea for the treatment of sickle cell anemia," *N Engl J Med*, vol. 358, pp. 1362-9, Mar 27 2008.
- [198] T. R. Gregory, "Nucleotypic effects without nuclei: genome size and erythrocyte size in mammals," *Genome*, vol. 43, pp. 895-901, Oct 2000.
- [199] E. A. Mancini, C. A. Hillery, C. A. Bodian, Z. G. Zhang, G. A. Luty, and B. S. Coller, "Pathology of Berkeley sickle cell mice: similarities and differences with human sickle cell disease," *Blood*, vol. 107, pp. 1651-8, Feb 15 2006.
- [200] Y. Beuzard, "Mouse models of sickle cell disease," *Transfus Clin Biol*, vol. 15, pp. 7-11, Feb-Mar 2008.
- [201] N. Patel, N. Sundaram, M. Yang, C. Madigan, V. K. Kalra, and P. Malik, "Placenta growth factor (PlGF), a novel inducer of plasminogen activator inhibitor-1 (PAI-1) in sickle cell disease (SCD)," *J Biol Chem*, vol. 285, pp. 16713-22, May 28 2010.
- [202] M. Hamidi, N. Zarei, A. Zarrin, and S. Mohammadi-Samani, "Preparation and validation of carrier human erythrocytes loaded by bovine serum albumin as a model antigen/protein," *Drug Deliv*, vol. 14, pp. 295-300, Jul 2007.

- [203] J. S. Tyrrell, C. Morton, S. M. Campbell, and A. Curnow, "Comparison of protoporphyrin IX accumulation and destruction during methylaminolevulinate photodynamic therapy of skin tumours located at acral and nonacral sites," *Br J Dermatol*, vol. 164, pp. 1362-8, Jun 2011.
- [204] J. S. Goldberg, "Transfusion of sickle cells may be a therapeutic option for patients suffering metastatic disease," *Med Hypotheses*, vol. 74, pp. 629-30, Apr 2010.
- [205] S. K. Ballas, "New era dawns on sickle cell pain," *Blood*, vol. 116, pp. 311-2, Jul 22 2010.
- [206] S. H. Orkin and D. R. Higgs, "Sickle Cell Disease at 100 Years," *Science*, vol. 329, pp. 291-292, July 16, 2010 2010.
- [207] C. Booth, B. Inusa, and S. K. Obaro, "Infection in sickle cell disease: a review," *Int J Infect Dis*, vol. 14, pp. e2-e12, Jan 2010.
- [208] M. Kurata, M. Suzuki, and N. S. Agar, "Antioxidant systems and erythrocyte lifespan in mammals," *Comp Biochem Physiol B*, vol. 106, pp. 477-87, Nov 1993.
- [209] B. Mintz, K. Anthony, and S. Litwin, "Monoclonal derivation of mouse myeloid and lymphoid lineages from totipotent hematopoietic stem cells experimentally engrafted in fetal hosts," *Proc Natl Acad Sci U S A*, vol. 81, pp. 7835-9, Dec 1984.
- [210] B. Endrich, H. S. Reinhold, J. F. Gross, and M. Intaglietta, "Tissue perfusion inhomogeneity during early tumor growth in rats," *J Natl Cancer Inst*, vol. 62, pp. 387-95, Feb 1979.
- [211] P. Rubin and G. Casarett, "Microcirculation of tumors. I. Anatomy, function, and necrosis," *Clin Radiol*, vol. 17, pp. 220-9, Jul 1966.
- [212] H. Dumez, W. H. Reinhart, G. Guetens, and E. A. de Bruijn, "Human red blood cells: rheological aspects, uptake, and release of cytotoxic drugs," *Crit Rev Clin Lab Sci*, vol. 41, pp. 159-88, 2004.
- [213] O. Skorokhod, E. V. Kulikova, N. M. Galkina, P. V. Medvedev, E. E. Zybunova, V. M. Vitvitsky, A. V. Pivnik, and F. I. Ataulakhanov, "Doxorubicin pharmacokinetics in lymphoma patients treated with doxorubicin-loaded erythrocytes," *Haematologica*, vol. 92, pp. 570-1, Apr 2007.
- [214] E. Zocchi, M. Tonetti, C. Polvani, L. Guida, U. Benatti, and A. De Flora, "Encapsulation of doxorubicin in liver-targeted erythrocytes increases the therapeutic index of the drug in a murine metastatic model," *Proc Natl Acad Sci U S A*, vol. 86, pp. 2040-4, Mar 1989.

- [215] A. J. Chicco, D. S. Hydock, C. M. Schneider, and R. Hayward, "Low-intensity exercise training during doxorubicin treatment protects against cardiotoxicity," *J Appl Physiol*, vol. 100, pp. 519-27, Feb 2006.
- [216] T. A. Elbayoumi and V. P. Torchilin, "Enhanced cytotoxicity of monoclonal anticancer antibody 2C5-modified doxorubicin-loaded PEGylated liposomes against various tumor cell lines," *Eur J Pharm Sci*, vol. 32, pp. 159-68, Nov 2007.
- [217] K. M. Laginha, S. Verwoert, G. J. Charrois, and T. M. Allen, "Determination of doxorubicin levels in whole tumor and tumor nuclei in murine breast cancer tumors," *Clin Cancer Res*, vol. 11, pp. 6944-9, Oct 1 2005.
- [218] J. R. Mourant, T. M. Johnson, G. Los, and I. J. Bigio, "Non-invasive measurement of chemotherapy drug concentrations in tissue: preliminary demonstrations of in vivo measurements," *Phys Med Biol*, vol. 44, pp. 1397-417, May 1999.
- [219] N. Doshi, A. S. Zahr, S. Bhaskar, J. Lahann, and S. Mitragotri, "Red blood cell-mimicking synthetic biomaterial particles," *Proc Natl Acad Sci U S A*, vol. 106, pp. 21495-9, Dec 22 2009.

BIOGRAPHICAL SKETCH

Se-woon Choe was born in Gwangju, Republic of Korea. He received his Bachelor of Science degree in the Department of Electronic and Electrical engineering from the Hong-Ik University in Seoul, Korea in 2001. He began his graduate studies in the Department of Electrical and Computer Engineering at University of Florida from 2002 and earned Master of Science degree in 2004. In 2006, he made a decision to move into the field of biomedical engineering when he was a second-year doctoral student and he joined in the Biophotonics Imaging, Therapeutics, and Sensing Laboratory (BITS lab) in the J. Crayton Pruitt Family Department of Biomedical Engineering. He received Master of Science degree under the guidance of Dr. Brian S. Sorg in 2008 and continued to pursue his doctoral degree. In the BITS lab, he has investigated the potential of SSRBCs as a novel drug carrier with better tumor targeting and controlled release of entrapped substance. His research interests include biophotonics, biomedical optics, cancer diagnostics and therapy, intravital microscopy, microcirculation, and tumor angiogenesis.